Cryogenic Current Comparators for Precise Ion Beam Current Measurements

Dissertation

zur Erlangung des Doktorgrades

der Naturwissenschaften

vorgelegt beim Fachbereich Physik

der

Johann Wolfgang Goethe-Universität

in Frankfurt am Main

von

Febin Kurian

aus Iritty (Indien)

Frankfurt 2015

(D 30)

In collaboration with

GSI Helmholtzzentrum für Schwerionenforschung GmbH Darmstadt

vom Fachbereich Physik der
Johann Wolfgang Goethe-Universität als Dissertation angenommen.

Dekan : Prof. Dr. Rene Reifarth

Gutachter : Dr. Peter Hülsmann

: Prof. Dr. Oliver Kester

Datum der Disputation: 23.03.2016

"Everything is theoretically impossible, until it is done" - Robert. A. Heinlein

Erklärung zur Dissertation

Hiermit versichere ich, die vorliegende Dissertation ohne Hilfe Dritter nur mit den angegebenen Quellen und Hilfsmitteln angefertigt zu haben. Alle Stellen, die aus Quellen entnommen wurden, sind als solche kenntlich gemacht. Diese Arbeit hat in gleicher oder ähnlicher Form noch keiner Prüfungsbehörde vorgelegen.

Darmstadt, den November 25, 2015

_____

(Febin Kurian)

Abstract

The planned Facility for Antiproton and Ion Research (FAIR) at GSI has to cope with a wide range of beam intensities in its high-energy beam transport systems and in the storage rings. To meet the requirements of a non-intercepting intensity measurement down to nA range, it is planned to install a number of Cryogenic Current Comparator (CCC) units at different locations in the FAIR beamlines. In this work, the first CCC system for intensity measurement of heavy ion beams, which was developed at GSI, was re-commissioned and upgraded to be used as a 'GSI-CCC prototype' for extensive optimization and development of an improved CCC for FAIR. After installation of a new SQUID sensor and related electronics, as well as implementation of improved data acquisition components, successful beam current measurements were performed at a SIS18 extraction line. The measured intensity values were compared with those of a Secondary Electron Monitor (SEM). Furthermore, the spill-structure of a slowly extracted beam was measured and analyzed, investigating its improvement due to bunching during the slow-extraction process.

Due to the extreme sensitivity of the superconducting sensor, the determined intensity values as well as the adjustment of the system for optimal performance are strongly influenced by the numerous noise sources of the accelerators environment. For this reason, detailed studies of different effects caused by noise have been carried out, which are presented together with proposals to reduce them. Similarly, studies were performed to increase the dynamic range and overcome slew rate limitations, the results of which are illustrated and discussed as well.

By combining the various optimizations and characterizations of the GSI CCC prototype with the experiences made during beam operation, criteria for a more efficient CCC System could be worked out, which are presented in this work. The details of this new design are worked out with respect to the corresponding boundary conditions at FAIR. Larger beam tube diameters, higher radiation resistivity and UHV requirements are of particular importance for the cryostat. At the same time these parameters affect the CCC superconducting magnetic shielding, which again has significant influence on the current resolution of the system. In order to investigate the influence of the geometry of the superconducting magnetic shield on different magnetic field components and to optimize the attenuation, FEM simulations have been performed. Based on the results of these calculations, modifications of the shield geometry for optimum damping behavior are proposed and discussed in the thesis.

Kurzfassung

Die geplante FAIR Anlage (Facility for Antiproton ans Ion Research) bei GSI wird ein breites Spektrum an Strahlintensitäten in ihren Hochenergie Strahltransportsystemen und in den Speicherringen erzeugen. Um den Anforderungen einer Intensitätsmessung bis in den nA Bereich zu genügen, ist es geplant, mehrere Einheiten eines kryogenen Stromkomparators (Cryogenic Current Comparator, CCC) an unterschiedlichen Orten der Strahlführung einzubauen.

Im Rahmen der vorliegenden Arbeit wurde das erste, bei GSI entwickelte CCC System für die Intensitätsmessung bei Schwerionenstrahlen wieder in Betrieb genommen und zum ‚GSI-CCC Prototypen' ausgebaut, mit dem Ziel, daran umfangreiche Optimierungen und Tests zur Entwicklung einer verbesserten Form des CCC durchzuführen. Nach Einbau eines neuartigen SQUID Sensors und der dazugehörigen Elektronik, sowie der Implementierung von verbesserten Datenaufnahmekomponenten, konnten erfolgreiche Strahlmessungen an einer Extraktionslinie des SIS18 sowie zahlreiche Untersuchungen bzgl. der Einflüsse der Beschleunigerumgebung auf das CCC System durchgeführt werden. Die gemessenen Intensitätswerte wurden mit denen eines Sekundärelektronen-Monitors (SEM) verglichen. Weiterhin wurde die Spill-Struktur eines langsam extrahierten Strahls mit Hilfe der CCC Messungen analysiert und ihre Verbesserung durch Bunching des Strahls während der Extraktion beurteilt.

Aufgrund der extremen Empfindlichkeit des supraleitenden Sensors werden beim CCC die ermittelten Intensitätswerte ebenso wie die Einstellung des Systems für eine optimale Leistungsfähigkeit stark von den zahlreichen Rauschquellen der Beschleunigerumgebung beeinflusst. Aus diesem Grund wurden detaillierte Untersuchungen verschiedener durch Rauschen verursachter Effekte durchgeführt, die zusammen mit Vorschlägen zu ihrer Reduzierung präsentiert werden. Gleichermaßen wurden Untersuchungen durchgeführt um den Dynamikbereich und die Anstiegsgeschwindigkeit Begrenzungen des Systems zu optimieren, deren Ergebnisse ebenfalls vorgestellt und diskutiert werden.

Durch Kombination der verschiedenen Optimierungen und Charakterisierungen des GSI-CCC Prototypen mit den Erfahrungen, die beim Betrieb gemacht wurden, konnten Kriterien für ein leistungsfähigeres CCC System ermittelt werden, welche in dieser Arbeit präsentiert werden. Die Details dieses neuen Designs werden im Hinblick auf die Randbedingungen bei FAIR erläutert. Für den Kryostaten sind insbesondere größere Strahlrohrradien, höhere Strahlungsbeständigkeit sowie UHV-Tauglichkeit gefordert. Dies beeinflusst in gleichem Maße die supraleitende Abschirmung des CCC, von der wiederum die Stromauflösung der Apparatur maßgeblich abhängt. Um den Einfluss der Geometrie der SC Schirmung auf die Abschwächung verschiedener Magnetfeldkomponenten zu untersuchen und um diese zu optimieren, wurden FEM Simulationen durchgeführt. Basierend auf den Ergebnissen dieser Rechnungen, werden Modifikationen der Schildgeometrie für ein optimales Dämpfungsverhalten vorgeschlagen und diskutiert.

Contents

List of Figures

Chapter 1

Introduction

After several decades of investigation on the mysteries of fundamental forces and the ultimate structure of subatomic particles, the physics of particle accelerators has proven to be an indispensable part of fundamental physics research. Moreover, there are many applications of accelerators in health care and industry which started as by-products but became - although still sometimes unseen by the non-expert - more and more important in daily life.

Accelerator technology is constantly pushing its boundaries to answer the remaining fundamental questions such as the nature of dark matter and dark energy, matter-antimatter symmetry and the search for grand unification theory. As a part of one such effort, the GSI accelerator facility will be upgraded to Facility for Antiproton and Ion Research (FAIR). FAIR is planned to have a largely extended range of particle beam parameters, mainly concerning particle species, energies and particle intensities. To fulfill the requirements of this enormous variety of beams from diagnostics point of view, new or improved diagnostics instruments are necessary, in particular for intensity ranges which have not been covered so far. For this reason Cryogenic Current Comparators (CCC) devices are planned to be installed at a number of locations in FAIR.

This thesis work presents the development, commissioning and successful beam test of a GSI-CCC prototype and describes extensive studies of the system performance and the steps for its optimization. This first chapter gives an introduction to the region of interest and the role of the CCC for the intensity measurement in accelerator facilities. Main features of the GSI and FAIR facilities are presented and standard intensity measurement schemes and their dynamic ranges are discussed - showing in particular the motivation to include CCCs in the FAIR beam diagnostics system. Finally a short overview of the CCC development at GSI is presented.

1.1 GSI and FAIR Accelerator Facilities

The "GSI Helmholtzzentrum für Schwerionenforschung" (Helmholtz center for heavy ion research) is an accelerator facility located in Darmstadt, Germany, jointly funded by the Federal Republic of Germany and by the state of Hesse. Capable of accelerating ions from the lightest (protons) to the heaviest stable element on Earth (Uranium), GSI facility is known for the discovery of several new, super-heavy chemical elements (eg. [1, 2]) and tumor therapy with ion beams [3]. The main fields of research at GSI are mid-range nuclear physics with heavy ions, atomic physics of highly-

charged ions, biophysics and radioactive beams. The accelerators and experimental areas in the GSI facility are shown schematically in figure 1.1. Ion beams, produced from the ion sources are accelerated through the linear accelerator UNILAC (UNIversal LInear ACcelerator) up to an energy of 11.4 MeV/u. These ions are used for several experiments at the experimental hall-I or further injected into the heavy ion synchrotron SIS18. SIS18 is capable of accelerating all kinds of accelerated ions injected from UNILAC to an energy range with a peak value of 1 GeV/u (for U^{73+} ions) to 4.5 GeV/u (for protons), depending on the ion species. The accelerated ions are delivered either by fast extraction to the Experimental Storage Ring (ESR- which can also re-inject the beam into SIS18 for further acceleration) or by slow and fast extraction to a number of experimental sections. In ESR the accelerated beams are accumulated, cooled and stored for a large number of experiments [4].

To satisfy a broadened scope of high energy physics, the GSI facility is currently upgraded to FAIR. In the coming years, the FAIR facility will expand the scope of science by generating intense secondary beams of rare, short-lived nuclei and anti-protons. These secondary beams will be produced by nuclear reactions from intense beams of stable particles, which have two orders of magnitude higher intensity than what is currently used at GSI [5].

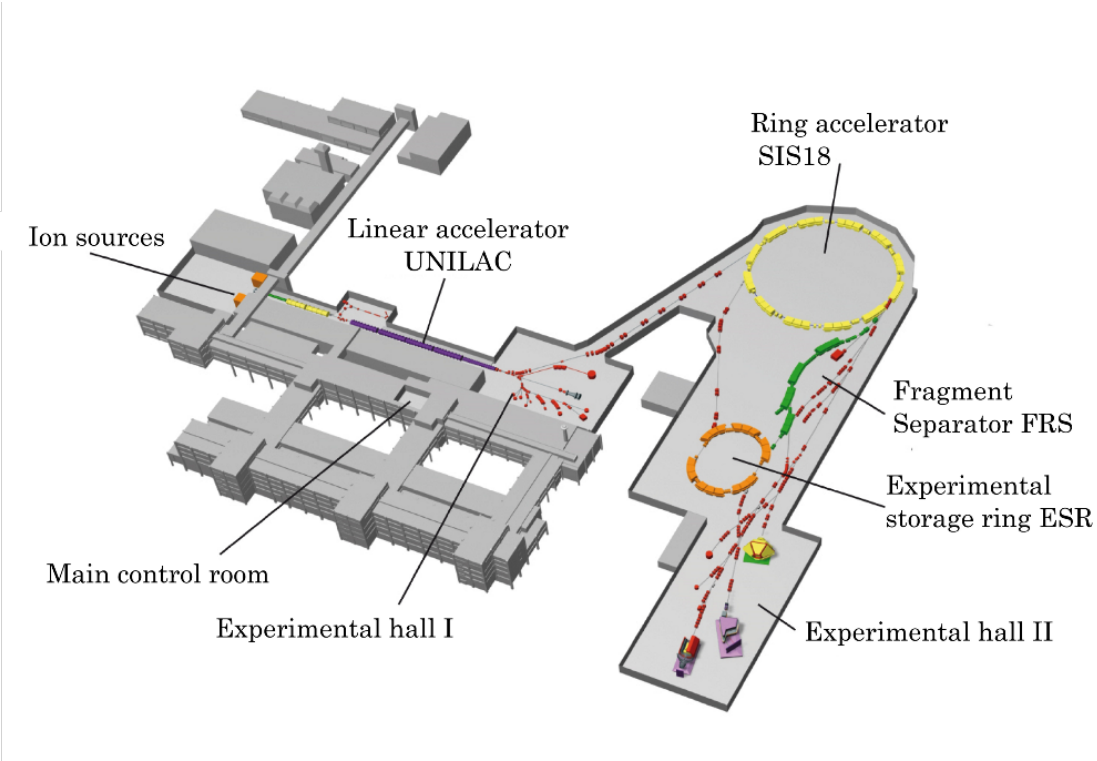

Figure 1.1: Schematic view of the accelerators and experimental areas at GSI.

The concept of FAIR is based on the scientific developments made over several years at GSI and other accelerator facilities worldwide in acceleration, storage and phase space cooling[1] of high energy protons and heavy-ion beams. The existing GSI facility, consisting of UNILAC, SIS18 and the storage ring ESR together with a new high current (up to 70 mA) proton *linac*,

[1] Dense beams with high energy resolution are produced by the phase space cooling [6]

will act as the injector chain for the FAIR facility. The central parts of the FAIR facility will be the two fast ramped synchrotrons SIS100 (with maximum magnetic rigidity, $\rho = 100\,T \cdot m$) and SIS300 (maximum $\rho = 300\,T \cdot m$) and four storage rings (named as HESR, RESR, NESR and CR) as shown in figure 1.2. The goal of SIS100 is to achieve intense pulsed beams from uranium of intensity 5×10^{11} ions per pulse (with an energy up to $1\,GeV/u$ and charge state $q = 28^{+}$) to proton (with an energy up to $29\,GeV/u$) of intensity 4×10^{13} ions per pulse [7]. With SIS300 foreseen to be installed in the second construction phase, the ultimate intensity of heavy ions are further increased (up to $45\,GeV/u$ for Ne^{10+} beams and up to $35\,GeV/u$ for U^{92+}), an energy and intensity regime in which nucleus-nucleus collision experiments become possible.

The synchrotrons SIS100 and SIS300 are connected to storage rings and other experimental sections through the High Energy Beam Transport (HEBT) sections. The storage rings are equipped with beam cooling facilities, internal targets and in-ring experiments. Together with the super-Fragment Separator (SFRS), where rare isotopes of all elements up to uranium can be produced and spatially separated within few hundred nanoseconds for studies on very short lived nuclei [8], unprecedented variety of particle beams will be available for studies at FAIR.

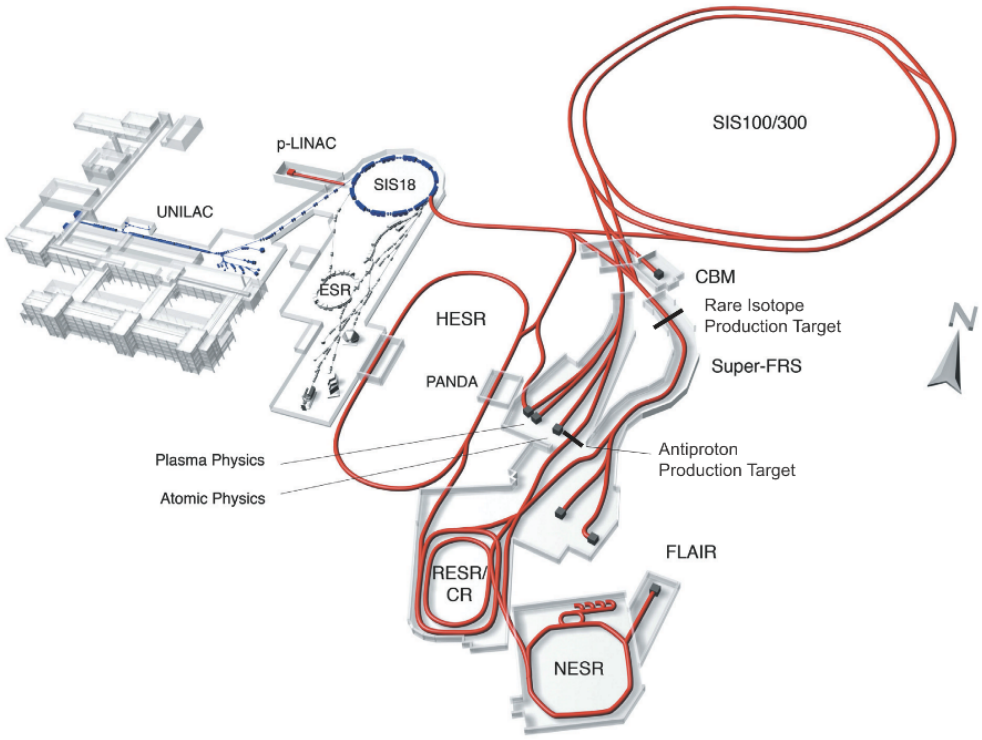

Figure 1.2: Schematic of various accelerators and experiments in the upcoming FAIR facility

At maximum intensity (1.5×10^{10} ions per spill), the slow extraction from the synchrotrons provides long pulses ($10 - 100$ seconds) of continuous beam. This fact together with the various operational modes of the synchrotrons demand for a high dynamic range of the intensity measurements at the synchrotrons and in the HEBT sections.

1.2 Intensity Measurements at FAIR

In general, one can think of beam diagnostics as the "organ of senses" which gives the perception of what are the properties of a particle beam and how it behaves at any position of an accelerator. The diagnostics requirements begin right from the commissioning of an accelerator to adjust and optimize the beam transport through various sections and to check the function, e.g. of the cavities. Most important quantities defining the characteristics of a beam are intensity, position, profile and angle, energy and energy spread, loss and luminosity (in case of particle colliders). Depending on operational modes, a number of diagnostics devices is required to cover the complete spectrum of beam parameters. In general individual particle accelerators have specific diagnostic requirements depending on different operating conditions and beam properties.

Beam intensity is one of the first diagnostic quantity to be measured in an accelerator since one should know how many particle are in the machine. The ratio between extracted and injected particles (transmission) is particularly important. Intensity is also important for determination of several other machine properties such as the life times of coasting beams in case of a circular machine and transfer efficiencies in case of beam transfer lines. The intensity measurements in an accelerator facility are in general spread over a wide range. For instance, in case of a *linac*, the beam to be measured passes only once through the diagnostic device with a large number of accelerating cavities causing different beam parameters at different points. Since a *linac* is a pulsed system, each pulse is unique in the sense that each may vary from shot to shot and hence very short pulses needs to be detected and the beam generated signals need to be analyzed separately. In cases of a synchrotron or a storage ring, the number of accelerating cavities is rather small and in most cases, there are periodical solutions as the beam reaches an equilibrium state. Hence high precision can be achieved by averaging and the beam current is either stable or a slowly varying parameter. The frequency range to be measured in a single accelerator ranges from DC to its RF frequency components and is commonly expressed in particle per second (alternatively particle per spill) *(pps)* or as a flux of charges expressed in Ampere (typically $nA - mA$ range). An overview of frequently used beam intensity measurement systems for accelerator facilities can be found in Ref.[9].

With an intensity in the range 10^4 to 10^{12} particle per spill at the slow extraction lines of FAIR, the intensity monitors need to be able to detect a beam current in the range of $1\,pA$ to $0.45\mu A$ depending on the species (assuming an extraction time of 1 second). Although simple techniques such as Faraday cups offer high resolution measurements (down to $10\,pA$) [10], the destructive nature of stopping the beam in the cup limits their applications. In addition, Faraday cups cannot be used for high energy beams (typically above $100\,MeV$). Since the beam is to be transported further to various experiments, non-disturbing methods or techniques with minimum possible interactions with the particle beam are highly desirable.

1.2.1 Beam Current Transformers

In principle, both electric and magnetic fields associated with charged particle beams can be used for the non-destructive intensity measurements. However measuring the electric field of the

beam (mostly by capacitive electrodes) has limited low frequency response and is - as a matter of principle - an indirect measurement. At the same time, magnetic materials are available with high permeability values (μ_r) which can be efficiently used for detecting very low magnetic fields associated with the ion beam. Hence beam current transformers (BCTs) are widely used as standard beam intensity measurement devices. Different types of BCTs are used depending on the nature of the beam from simple ac current transformers (ACCTs) to dc current transformers (DCCTs) [11], both require highly sophisticated ring core design and analog electronics.

The general priciple of these transformers is as follows: A particle beam passes through the center of a high permeability torus like the primary winding of a classical transformer with single winding number ($N_p = 1$). The time varying magnetic field induces a current in the secondary winding, which is wound around the torus with N_s turns and an inductance L_s. The output signal corresponding to the signal produced in the secondary coil is readout across the load resistor after amplification. A feedback circuit improves the low frequency response of the transformer which is otherwise limited by the inductance of the secondary winding and the load impedance.

The main purpose of the high permeability torus is to guide the magnetic field lines within the secondary windings along the azimuthal direction. In order to avoid the mirror current flowing through the metallic beam pipe which would cancel the resulting field outside the beam pipe, a ceramic gap is an essential part of the BCT installations [12]. The detection threshold of current transformers is limited by unavoidable thermal noise (mainly from the load resistor), Barkhausen noise [13] and magnetic interferences. Additionally, the performance of BCTs is also influenced by temperature fluctuations, amplifier noise and moreover by the the magnetic core design. Typically the minimum detectable beam current of a standard room temperature transformer is around $1\,\mu A$. To meet the requirements of the high current (>70 mA) and high bunch frequencies (1.2 MHz) at FAIR, alternative current transformer schemes are currently under development at GSI [14].

1.2.2 Devices for Low Beam Intensities

For experiments in particle, atomic and nuclear physics, ion beam energies typically higher than 100 MeV are used. Due to the detector types used in these experiments, slowly extracted beams from the synchrotron are required in most of the cases. During slow extraction, the intensity typically ranges from 10^4 particles per second to 10^{12} particles per second which corresponds to a beam current of $1\,pA$ to $1\,\mu A$. This range is below the detection threshold of normal beam current transformers. Since the beam has to be transported to further experiments and due to high particle energies, Faraday cups and similar destructive techniques can not be used to measure the intensity. Therefore a number of particle detectors are used as standard devices to measure the beam current. They generally use the charged particles energy loss in matter to detect the beam intensity and are hence considered as intercepting techniques. Here three examples of particle detectors which are used in the SIS18 extraction lines are briefly described together with the alternative solution of a Cryogenic Current Comparator (CCC). Figure 1.3 gives an overview of their application ranges.

Scintillators

When a particle beam impacts on a scintillating material, fluorescent photons are emitted. These photons are detected by a photo-multiplier tube and subsequently converted into electrical pulses by a discriminator and counted by a scaler as a measure of the number of particles in the beam. The scintillating material, exposed to a particle beam, emits the energy transferred by the collision in the form of photons in the visible wavelength - a phenomenon called *luminescence*, ensuring high efficiency at the photo-multiplier tube [15]. To achieve high counting rate, *fluorescent materials* are used as scintillators which emits the absorbed energy as photons within several nanoseconds. Plastic scintillators are most widely used since they are cheap and easy to produce in nearly any mechanical shape. Plastic scintillators also have relatively short decay times of few nanoseconds. Scintillators give the absolute number of particles without an external calibration required. With this method, up to 10^6 particles per second can be measured, which is useful either for direct current measurement or for calibration of devices which are suitable for higher intensities, like Ionization Chambers (see below).

Ionization Chambers

The ionization chamber (IC) is a simple and reliable method to measure the beam current in a medium intensity range (see figure 1.3). The particle beam passing through the chamber filled with a gas (typically Ar) causes partial ionization of the gas molecules and generates electron-ion pairs. The active volume, normally confined within two electrodes (metalized plastic foils) is kept at a potential difference of about $1\,{}^{kV}/_{cm}$ to separate the charges produced in the gas volume. Hence a secondary electron current is produced in one of the electrodes and is amplified with a sensitive current amplifier. The metallic foils act as electrodes typically have a thickness in the order of $100\,\mu m$. The thickness is carefully chosen so that the foil causes minimum possible energy loss to the beam.

The secondary electron current produced by a particle beam at an energy E within the active length Δx of the chamber is given by,

$$I_{sec} = \frac{1}{W} \cdot \frac{dE}{dx} \cdot \Delta x \cdot I_{beam} \tag{1.1}$$

where W is the average energy to produce an electron-ion pair. The ratio ${}^{dE}/_{dx}$ is an empirically calibrated value, calibrated against scintillators where absolute measurement is possible. Secondary electron currents down to $1\,pA$ can be measured precisely with this technique. The upper threshold of the current measurement is normally influenced by the presence of gases with high electron affinity, such as O_2 or H_2O. The secondary electron current is kept below an upper limit of about $\sim 1\,\mu A$ to avoid saturation effects in the IC measurements [15].

Secondary Electron Monitors

Secondary electron monitors (SEM) provide beam intensity measurements in the higher range compared to ionization chamber and scintillators by the emission of secondary electrons from a metallic surface after penetration of particle beam through the surface. A typical SEM set up

consists of three thin foils of Aluminum (or Titanium) with first and third foil biased typically around $100\,V$. The middle foil is connected to a sensitive current amplifier. The secondary electrons released up on the beam passage are subsequently drifted away by the bias electric field and produce a secondary electron current which is amplified and measured. The secondary electron current is given by,

$$I_{sec} = Y \cdot \frac{dE}{\rho dx} \cdot I_{beam} \tag{1.2}$$

where Y is the yield factor which describes the number of secondary electrons emitted per unit energy loss at the surface of the foil. ρ is the density of the foil material and $\frac{dE}{dx}$ describes the energy loss of the beam per unit thickness of the foil. The yield factor is an empirically estimated value which could be changed by the irradiation and aging effects on the surface of the foil causing changes in the work function. The working principle and current measurement details of the SEM is described in detail in chapter 4 where the current measured by the CCC is compared with SEM output.

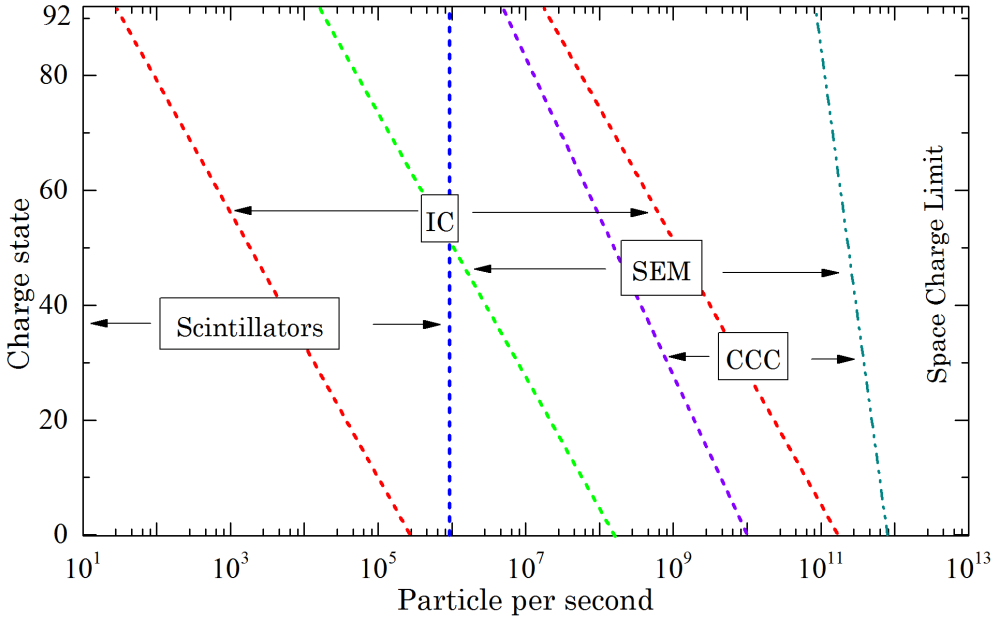

Figure 1.3: Ranges of different intensity measurement techniques used for the slow extraction at GSI synchrotron. Figure courtesy, P. Forck [10]

Cryogenic Current Comparator

A possibility to fill the gap between the detectors for lowest intensities and the beam transformers (as well as a possibility to calibrate these detectors) is to use a SQUID based Cryogenic Current Comparator (CCC) as a beam intensity monitor. This device works on the principle of precise detection of the azimuthal magnetic field of the ion beam. A toroidal pickup unit detects the beam magnetic field with high resolution by making use of the principles of superconductivity. The detected signal is amplified using one of the most sensitive magnetic flux sensor, the dc

SQUID (Superconducting Quantum Interference Device). By absolute calibration of the output to a known current, the CCC offers intensity measurements independent of energy or position of the particles inside the beam tube. The CCC developed at the GSI beam diagnostics group lead by A. Peters [16] has been shown to measure the beam current with high resolution ($< 1^{nA}/\sqrt{Hz}$) and high dynamic range ($10\,kHz$). With a number of improvements on the performance, advanced CCC systems are planned to be installed in the upcoming FAIR facility and related other experiments. Figure 1.4 shows the planned locations of CCCs in the FAIR accelerator beamlines. The investigation and optimization of a new improved CCC unit with advanced sensor components is the main topic of this thesis.

1.3 Motivation and Structure of this Thesis

With the ever increasing beam energy and intensity limits for particle beams, the dynamic ranges of standard beam diagnostic techniques are pushed to their theoretical limits by replacing the sensing materials with more advanced ones and enhanced read out schemes. Another challenge in this field is to reduce the noise contributions from various sources which limits the performance. The intensity measurement requirements for the FAIR facility are a typical example for the demand of beam diagnostic devices with high resolution and broader dynamic ranges especially at the slow extraction sections of the synchrotrons. Slowly extracted beams with energy well above $1\,{}^{GeV}/_{u}$ with spill duration over several seconds and with high intensity (above 10^{10} particles per pulse) give a number of challenges to the existing techniques. As the extracted beams are to be transferred to various experiments, non-intercepting techniques are preferred at the extraction sections over the standard intensity measurements, which have limitations due to the interaction of beam with the sensing element. Moreover to control beam losses and extraction efficiencies at regular intervals, non-intercepting techniques are required at certain locations. As a natural choice for the measurement of new intensity ranges as demanded by FAIR, six CCC units are planned to be installed at various locations as shown in figure 1.4.

For the design of improved CCC units to be installed in the FAIR facility, the system originally developed at GSI was recommissioned. This system was used as a prototype to test new improved components. Refurbishing the existing CCC system enabled the characterization of individual components with respect to their performance. Secondly, the prototype was tested inside an accelerator beamline to optimize the system performance in a realistic environment. Hence the first phase of this work was dedicated to recommission this CCC system by replacing various vacuum and cryogenic components. After successful operation, test measurements in the lab environment were carried out. The main components responsible for the high resolution of the CCC compared to other non-intercepting techniques are the DC SQUID and associated FLL electronics unit. Based on the comparative studies done by R. Geithner [17], DC SQUID and the FLL electronics were purchased from commercial vendors and installed in the GSI - CCC prototype. A detailed description of the theory of current measurement using DC SQUID and FLL electronics is shown in chapter 2. The technical concept and details of various components of the GSI-CCC prototype are discussed in chapter 3.

In the second part of this work, the CCC system was installed in an extraction beamline

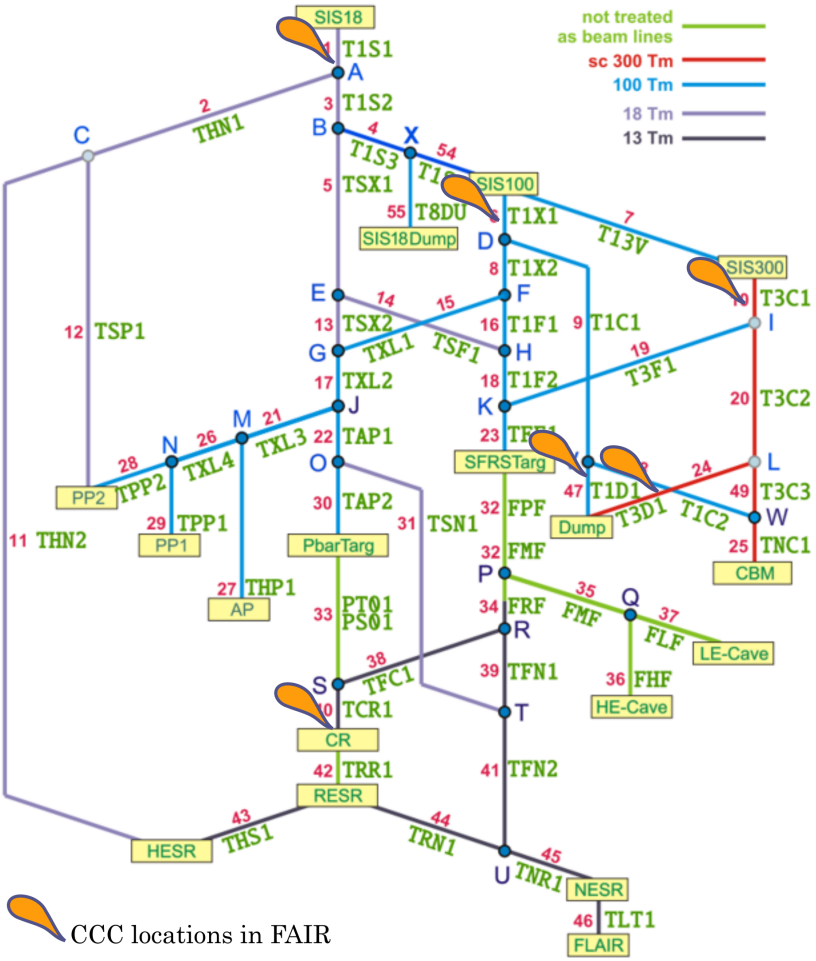

Figure 1.4: Planned installation locations of CCC (shown by the marker) in the first modularized start version of the FAIR facility. Beam from different rings are shown in different colors as indicated in the legend.

of the GSI synchrotron SIS18 to measure currents of slowly extracted ion beams with varying parameters. Besides a number of characterization studies, the GSI - CCC prototype was successfully used to measure ion beam current down to $2\,nA$. A set of bunched and unbunched beams with different intensities and extraction times were measured and compared with standard beam intensity measurement techniques as discussed in chapter 4. The current fluctuations driven by a number of noise sources are found to limit the absolute current resolution offered by the CCC. To address the influence of these factors on the measurements, detailed investigations were carried out. The dependence of temperature and pressure fluctuations on the current offset drift are discussed in chapter 5.

With a number of advanced CCC systems foreseen to be installed in FAIR and its related experiments, an outlook into an advanced CCC systems is discussed in chapter 6. Several possible investigations on further system improvements are discussed in this chapter and the thesis work is summarized in chapter 7 .

Chapter 2

Current Measurement using DC SQUIDs

As discussed in the previous chapter, by detecting azimuthal magnetic field associated with the particle beam, one can measure the beam current with high precision. However the sensitivity in case of beam current transformers which work on this principle are highly limited by the noise in case of low intensity beams ($< 1\,\mu A$) [10] in detection of the field as well as in amplification of the detected signal. By using a cryogenic pickup and readout unit, Cryogenic Current Comparators overcome these limitations to realize beam current detection with extremely high resolution. The CCC detects the magnetic field of the beam using a superconducting pickup unit (see section 3.3.1). Conversion of the detected signal to measurable output voltage is achieved with the highest sensitive magnetic flux sensor, the Superconducting Quantum Interference Device (SQUID).

In this chapter, the basic concepts of the dc SQUID and its readout electronics - which together form the magnetic flux sensor unit in the Cryogenic Current Comparator - is discussed. A simplified theoretical model of the sensor unit is developed for the quantitative understanding of the system. In the first section, evolution and basic principles of superconductivity are briefly described leading to the development of the dc SQUID. The working principle of the dc SQUID as a magnetometer and its noise figure is discussed in the second section. For the practical readout of the output signal, the dc SQUID is operated in the so called Flux Locked Loop (FLL) mode as explained in the third section. In this section, also different readout schemes in FLL mode of operation are discussed with focus on the direct-coupled readout scheme which is applied in our CCC system. The basic noise figure characterizing the performance of the readout scheme along with the dynamic performance and bandwidth of the system is presented in the fourth section. The flux transformer, which couples the beam current signal to the SQUID sensor is described in the final section.

2.1 Superconductivity Basics

An ideal superconductor is a material which exhibit zero electrical resistivity[1] and perfect diamagnetism when it is cooled below a particular temperature called critical temperature (T_C). This phenomenon of superconductivity was first observed by Heike Kamerlingh Onnes in 1911, three years after he succeeded to liquify Helium. Onnes observed the dc resistivity of mercury falls to zero when it was cooled down to 4.15 K. In the following years new metals such as Lead ($T_C = 7.2\,K$), Tin ($T_C = 3.7\,K$), Niobium ($T_C = 9.2\,K$) which are not very good conductors at room temperatures were found to be superconducting. Later the superconductivity was observed in a wide range of materials at various transition temperatures and the quest still continues with the ultimate goal of achieving superconductivity at room temperature [18, 19, 20].

Soon after the discovery of the superconductivity, Onnes observed [21] that current density in superconductors has a temperature dependent threshold value above which the property of zero electrical resistivity is lost. This threshold value is called critical current (I_C).

The second distinguishing characteristics of superconductors - perfect diamagnetism- was first observed by Meissner and Ochsenfeld (in 1933). This property causes that the superconducting surface doesn't permit any magnetic field to penetrate that surface and expels it from the material. This observation was later modified by Fritz London and Heinz London in the sense that the magnetic field can penetrate into the superconducting surface as far as a transition layer of thickness λ, called *London penetration depth*. Two London equations proposed by the London brothers connected electric and magnetic field to the current density on a superconducting surface. The first London equation describes the perfect conductivity of a superconductor having a super-current density $\overrightarrow{J}$ is given by,

$$\overrightarrow{E} = \frac{m}{n_s e^2} \cdot \frac{\partial \overrightarrow{J}}{\partial t} \tag{2.1}$$

where m is the mass, e its charge and n_s is the density of superconducting electrons (super-electrons). The second London equation describes the effect of applied magnetic field $\overrightarrow{B}$ on the superconducting material. As given by the Meissner effect, when a field $\overrightarrow{B}$ is applied to the superconducting material, a magnetic field is formed at the superconducting surface such that the applied magnetic field cancels out within the penetration depth, λ. A superconductor with a super-current density $\overrightarrow{J}$, this magnetic field is given by,

$$\overrightarrow{B} = -\mu_0 \lambda^2 \cdot \nabla \times \overrightarrow{J} \tag{2.2}$$

where μ_0 is the permittivity of free space ($\mu_0 = 4 \cdot \pi \times 10^{-7}\,{}^{H}/_{m}$).

Similar to the critical temperature limit, superconductors also posses a critical magnetic field (H_C). A superconductor placed in a magnetic field higher than H_C loses its superconducting properties. Based on the response of the material to the external magnetic fields, superconductors are generally classified as type- I and type- II superconductors. Those which totally exclude the magnetic flux from the interior within the critical magnetic field limit are called Type-I

[1] Falls down to a factor of at least 12 of the room temperature resistivity, and hence for all practical purposes it is taken as zero.

superconductors. Popular examples are Lead (Pb), Mercury (Hg), Indium (In) etc.. Type-I superconductors normally have critical temperatures, T_C below $10\,K$ and have a unique critical magnetic field, H_C in the range of $10 - 100\,mT$ [22]. Type- II superconductors are also perfect conductors of electricity but with more complex magnetic properties, having two critical magnetic fields H_{C1} and H_{C2}. Totally expelling magnetic fields when applied field is below H_{C1}, type- II superconductors are termed to be in *Meissner phase.* But when the applied field is within the range H_{C1} and H_{C2}, type- II superconductors get in to a *Mixed phase* (also known as *Shubnikov phase*) in which they loose the perfect diamagnetic properties and the magnetic field penetrates in to the material in the form of quantized vortices.

A theoretical explanation to the macroscopic superconductivity was given by Ginzburg and Landau (GL theory) in 1950 by defining a complex order parameter ψ, the physical significance of which is that, $\mid \psi^2 \mid$ is proportional to the density of the superconducting electrons. The London equations were explained as a natural consequence of the GL theory. In 1957, J. Bardeen, L. Cooper and J. R. Schrieffer proposed the first microscopic explanation of superconductivity by the BCS theory which could derive most of the important theoretical predictions. The BCS theory assumes that an energy gap between the superconducting and normal conducting states is generated by the formation of a bound electron pair in the superconducting state. These electron pairs with charge $2e$ have a common center of mass and are known as Cooper pairs. According to BCS theory, exchange of virtual phonons give rise to the attractive interactions within the Cooper pairs [23]. The electrons of a Cooper pair have opposite momenta and spin and have relatively large distance of the order of 10 to $1000\,nm$ between them. Therefore the wave functions of the individual Cooper pairs in a superconductor are in a strongly overlapped state. This results in a *phase locked state*, which can be described by a single wave function, also described as the order parameter similar to what was proposed by GL theory. As a result, when considering the total number of particles, the phase will be conserved and hence the macroscopic variables such as current can depend on the phase φ. The macroscopic quantum wave function is be given by,

$$\Psi(\overrightarrow{r},t) = \Psi_0(\overrightarrow{r},t)\, exp(i\varphi(\overrightarrow{r},t)) \tag{2.3}$$

where $\Psi_0(\overrightarrow{r},t)$ is proportional to the density of the Cooper pairs within the superconductor. The macroscopic quantum wave function describes the behavior of the entire ensemble of the charge carriers in the superconductor. By considering as a quantum mechanical probability current, the current density inside a superconductor is given by,

$$J_S = \frac{\hbar n^* q^*}{m^*}\{\nabla\varphi(\overrightarrow{r},t) - \frac{2\pi}{\Phi_0}A(\overrightarrow{r},t)\} \tag{2.4}$$

where $\hbar = {}^{h}/_{2\pi}$ (h is the Planck's constant), n^* is the number, q^* is the charge and m^* is the mass of the Cooper pairs and $A(\overrightarrow{r},t)$ is the magnetic vector potential. Equation 2.4 shows that the current density inside a superconductor is proportional to the gauge invariant phase difference in the macroscopic wave function.

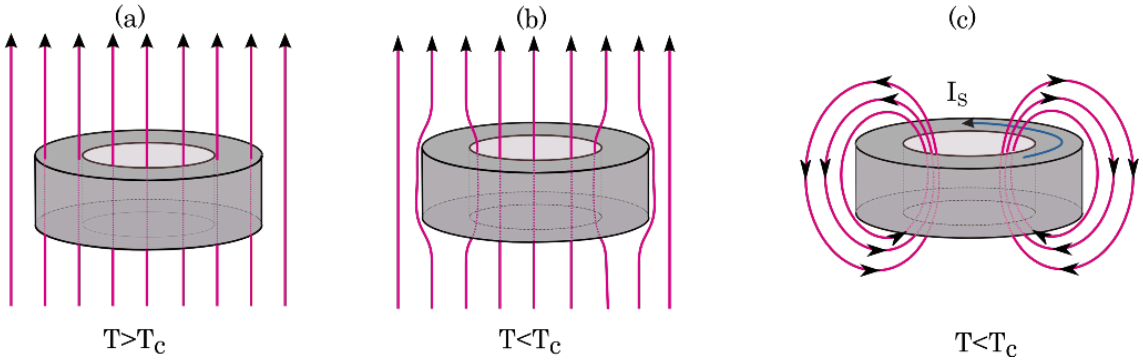

Figure 2.1: Meissner effect and evolution of flux quantization in superconducting rings

2.2 Flux Quantization and Josephson Effect

In case of a type-I superconductor, the Meissner effect gives that the externally applied magnetic field (less than H_C) is excluded from penetrating the material if the temperature is below T_C. This effect can be explained as follows; any magnetic field applied in a direction perpendicular to the superconducting surface creates screening current in closed contours on the surface of the material in such a direction that the magnetic field produced by this current is equal and opposite to applied magnetic field. The effect is particularly interesting considering the case of a superconducting ring as shown in figure 2.1. When the temperature is above T_C, the field penetrates the material as shown in figure 2.1 (a). However as the temperature is brought below T_C, the shielding current develops so that the external magnetic field inside the superconducting material is nullified by the field produced by the screening current. In other words, the applied field is expelled out of the material as shown in figure 2.1 (b). The total magnetic flux threading inside this superconducting ring has special characteristics. This flux cannot be varied in a continuous manner but only by field values corresponding to integer multiples of the flux quantum ($\Phi_0 = 2.068 \times 10^{-15} Wb$, $1\,{}^{Wb}/_{m^2} = 1\,T$). This phenomenon is termed as flux quantization. If the applied field is switched off as shown in figure 2.1 (c), the shielding current doesn't decay and will carry on circulating the ring as long as the ring is in superconducting phase. As a result, the flux associated with this current remains trapped around the ring [24, 25].

The flux quantization can be explained theoretically by the condition that the macroscopic wave functions must be single valued around the superconducting loop. This condition arises from the fact that a stationary state for the super-current along the ring can be expected only if the macroscopic wave function (describing the whole ensemble of Cooper pairs) is interfering non-destructively. Hence in case of a superconducting loop threaded by n quanta of magnetic flux, the phase around the loop is quantized by $2\pi n$. Flux quantization in the superconducting ring was the first consequence of the macroscopic quantum nature of superconductivity.

The second consequence of the macroscopic quantum nature of superconductivity is the Josephson effect. The Josephson effect is observed when two superconductors are separated by a thin layer of resistive or insulating material (as shown in figure 2.2) to form weakly coupled [26] superconducting junctions known as Josephson Junctions. In the absence of an externally applied electric or magnetic field, Cooper pairs tunnel through the junction producing a phase difference

between the either side of the two superconductors. This phase difference causes a dc current to flow spontaneously through the superconductors without forming a voltage across the junction. The super-current through the Josephson junction is given by the first Josephson equation,

$$I = I_C sin(\delta)$$

where δ is the difference between the phases of two superconducting electrodes and I_C is the critical current of the Josephson junction. Any current above the critical current flowing through the junction will be normal electrons governed by Ohm's law. That is when a current greater than I_C is flowing through the junction, a finite voltage V will be formed across the junction and is termed to be in resistive state. This voltage induce a phase difference δ in the macroscopic wave function given by the second Josephson equation.

$$\frac{d\delta}{dt} = \frac{2eV}{\hbar} = \frac{2\pi V}{\Phi_0} \tag{2.5}$$

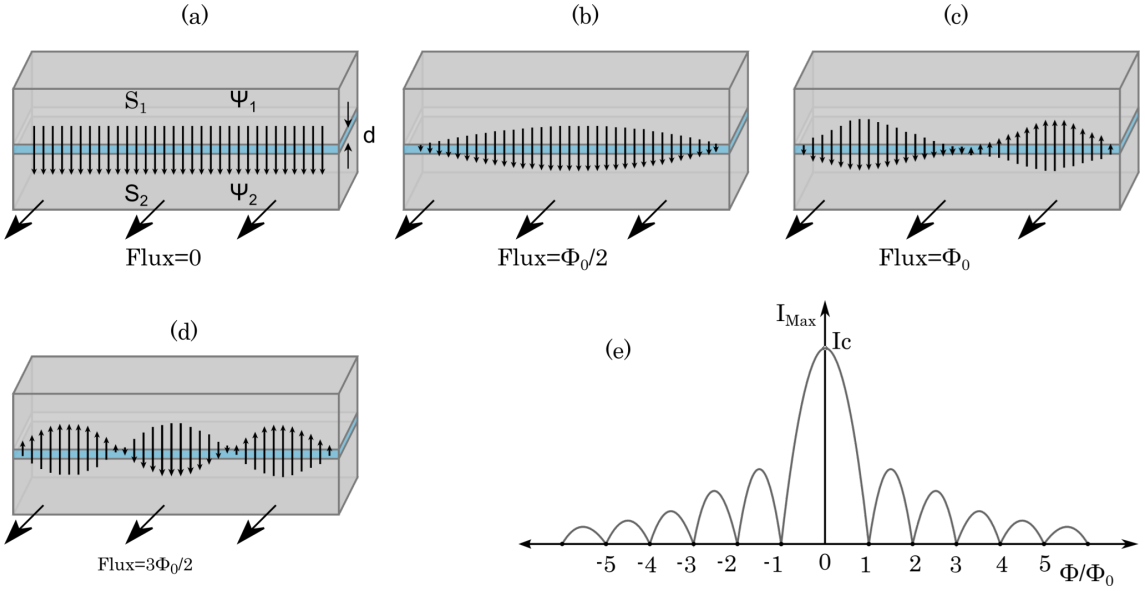

Figure 2.2: Tunneling current oscillations across a Josephson junction formed by two superconductors S_1 and S_2 separated by a thin insulator of thickness d. Ψ_1 and Ψ_2 indicate the wave functions associated with the superconducting elements. Four cases of current density oscillations when a magnetic flux is applied parallel to the plane of the junction from $\Phi = 0$ to $\Phi = {}^{3\Phi_0}/_2$ are shown from (a) to (d). Josephson-Fraunhofer diffraction showing maximum critical current oscillations when the current density is uniform across the junction (e).

When a magnetic field is applied in a direction parallel to the plane of the Josephson junction, the maximum Josephson current undergoes oscillations that follows the Josephson junction diffraction equation. This oscillation, as shown in figure 2.2(e) has the shape of Fraunhofer diffraction pattern in optics and is given by,

$$I_{max} = I_C \frac{\sin({}^{\pi\Phi}/_{\Phi_0})}{{}^{\pi\Phi}/_{\Phi_0}} \tag{2.6}$$

The Josephson junction diffraction pattern can be understood from figures 2.2 (a) - (d). When the applied magnetic field parallel to the Josephson junction is zero, total tunneling current across the junction, I_{max} (total integral of the surface current over the junction area) is maximum. However as the magnetic field is increased, the super-current starts to flow across the junction forming closed loops within a penetration depth λ in a direction such that the magnetic field is opposed by the current loops and hence forming Josephson Vortices [27]. When the applied field is such that the flux in the junction is equal to one Φ_0 or its integral multiples, the total phase change across the breadth of the junction reaches 2π. At these phase values, total integral of the current density over the junction area becomes zero and reaches maxima for each half integral values..

2.3 Principle of the DC SQUID

A simple Josephson junction can be used as a magnetic flux sensor, which can count the flux as an integer multiple of Φ_0, based on the diffraction behavior explained above. However, for practical applications, the sensitivity of this device has to be increased, both, the sensing area as well as the sensitivity of the detector. A practical method is to usea parallel arrangement of two identical Josephson junctions which form a superconducting loop. In this way the phenomenon of flux quantization and Josephson effect is combined to form an extremely sensitive magnetic flux sensor termed as Superconducting Quantum Interference Device (SQUID).

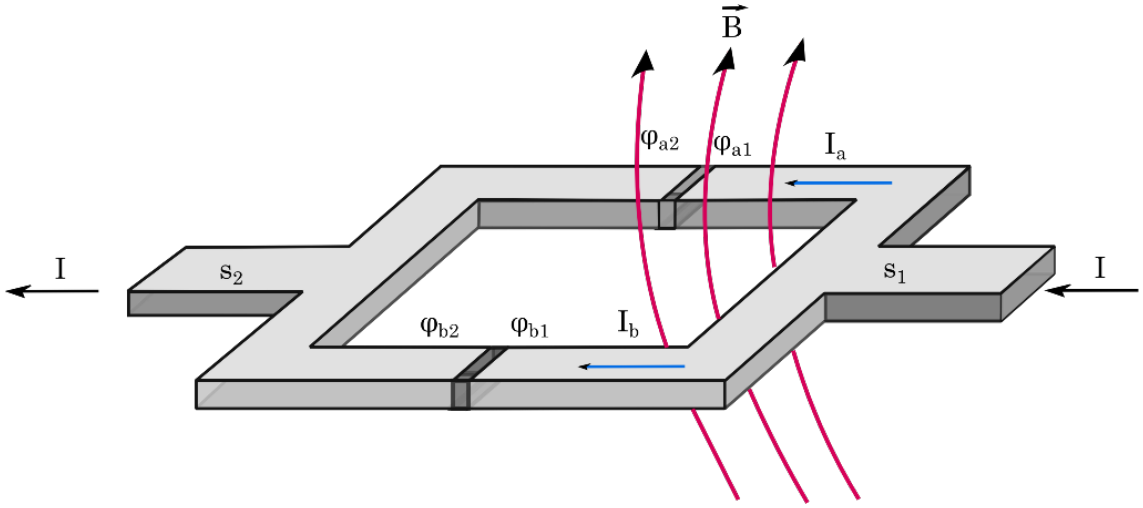

Figure 2.3: Superconducting loop containing two weak links a and b forming a SQUID in the presence of applied current $I_a + I_b$. φ_a and φ_b describes the phase of the superconducting wave function and $\vec{B}$ is the magnetic field coupled with the loop.

A superconducting loop containing two identical parallel Josephson junctions a and b with negligible individual junction areas is shown in figure 2.3. When an external magnetic flux ($\Phi = B \cdot A_{eff}$, B being the applied field and A_{eff} is the effective area within the ring) goes through the SQUID loop, a phase difference in the macroscopic wave function is produced by each of the Josephson junctions. If δ_a is the resulting phase difference of the wave function between either side of the junction a (given by $\delta_a = \varphi_{a2} - \varphi_{a1}$) and δ_b is the phase difference at

the junction b (given by $\delta_b = \varphi_{b2} - \varphi_{b1}$), from flux quantization,

$$\delta_a = \delta_b + {}^{2\pi\Phi}/_{\Phi_0} \tag{2.7}$$

then the total current passing through the branches of the superconducting loop will be the sum of individual currents I_a and I_b, with each of the junctions satisfying its own Josephson equations,

$$I = I_a + I_b = I_{Ca} \sin \delta_a + I_{Cb} \sin \delta_b \tag{2.8}$$

Assuming the junctions are identical($I_{Ca} = I_{Cb} = I_C$) 2.8 can be written as,

$$I = I_C[\sin \delta_a + \sin(\delta_a - {}^{2\pi\Phi}/_{\Phi_0})] \tag{2.9}$$

with the maximum current obtained when the phase values are at, $\delta_a = {}^{\pi}/_{2} + {}^{\pi\Phi}/_{\Phi_0}$ and $\delta_b = {}^{\pi}/_{2} - {}^{\pi\Phi}/_{\Phi_0}$. The magnitude of the maximum current is then given by,

$$I_{max} = 2I_C |\cos(\frac{\pi\Phi}{\Phi_0})| \tag{2.10}$$

The maximum current oscillates between 0, at $\Phi = (n + {}^{1}/_{2}\Phi_0)$ and $2I_C$, at $\Phi = n\Phi_0$ as shown in figure 2.4. In the case $I_{Ca} \neq I_{Cb}$, the maximum current through the loop oscillates between $I_{Ca} - I_{Cb}$, at $\Phi = (n + {}^{1}/_{2}\Phi_0)$ and $I_{Ca} + I_{Cb}$, at$\Phi = n\Phi_0$. However for practical applications, the two junctions should be matched within few percent to avoid significant performance degradation [28].

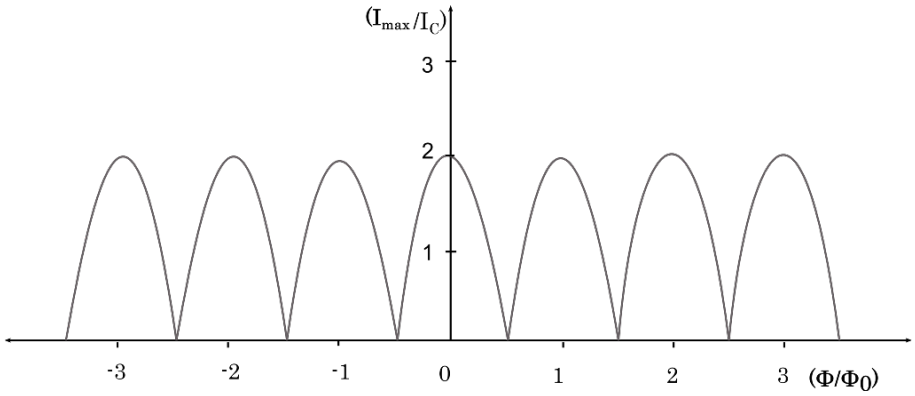

Figure 2.4: Dependence of maximum current through the the Superconducting loop with identical Josephson junctions on the applied magnetic flux (normalized relative to the flux quantum).

By measuring the critical current oscillations, one can directly detect the change in the externally applied magnetic field. One way to measure the change in critical current is by varying a bias current (I_B) untill a dc voltage is formed across the SQUID at a certain critical current value and measure the voltage for each change in the applied magnetic field. The easier and more practical method is to measure the change in magnetic field by keeping the bias current constant above critical current of the junction ($I_B > 2I_C$) and measure the time averaged voltage difference across the SQUID, which is modulated with a period of one Φ_0 (as shown in figure 2.6). In this way the SQUID directly acts as a flux to voltage transducer like shown in section 2.3.2.

Due to the loop geometry and the readout type, this SQUID type is termed as 'dc SQUID'. Another type of SQUID is formed by a superconducting loop consisting of a single Josephson Junction coupled to an LC-tuned circuit, known as rf SQUIDs. In rf SQUIDs, no dc electrical connections to the readout electronics are necessary unlike dc SQUIDs. A change in the flux coupled to the superconducting loop causes a change in the loading of the tuned LC circuit. The resulting change in the rf voltage across the circuit is measured as the output, which is responsible for the name 'rf SQUID'. The details of this devices can be found in most superconductivity text books (e.g., [22]).

Modern SQUIDs are fabricated on thin films by photo-lithography or electron beam lithography methods. They normally have a square washer structure with superconducting input coil in spiral shape with insulating layer (usually SiO_2) in between. Hundreds of batches of such devices are deposited on oxidized silicon wafers with the entire structure made of Nb except the shunt resistors, which are typically made of Mo or Pd. Since the input coils are superconducting, the impedance of the input coils is purely inductive. The junctions are patterned from a $Nb-AlO_X-Nb$ which itself was an important development in the SQUID fabrication technology as these junctions are highly reproducible and are nearly indestructible. A detailed description on the fabrication of the dc SQUIDs can be found in [29].

2.3.1 Shunt Resistance - RCSJ Model

Since the dc SQUID working principle is based on its superconducting and resistive behavior, one of the basic requirement for its fabrication is to have a stable, non-hysteric Current-Voltage (I-V) characteristics. Otherwise as the bias current is increased from zero the voltage will abruptly increase when the bias current exceeds I_C and return back to zero only when bias current is brought to a value much less than I_C. Intrinsically high quality tunnel junctions posses a hysteric voltage-current characteristics due to their large capacitance. The easiest way to remove the hysteresis is by using external shunt resistors as described by the *Resistively and Capacitively Shunted Junction* model (RCSJ model) [30] as schematically shown in figure 2.5. The RCSJ model defines the so called *tilted washboard potential*, U_J of the Josephson Junction, where the phase difference δ introduced by the bias current I_B is analogized as a particle moving on a tilted washboard given by the equation of motion,

$$\frac{\Phi_0}{2\pi}C\ddot{\delta} + \frac{\Phi_0}{2\pi}\frac{1}{R}\dot{\delta} = I_B - I_C \sin\delta = -\frac{2\pi}{\Phi_0}\frac{\partial U_J}{\partial \delta} \tag{2.11}$$

where the I_C is the critical current of the Josephson junction which is in parallel with its own parasitic capacitance, C and its resistance R. It should be noted that, here the current noise associated with the resistance is not considered for simplicity. To consider the limiting cases in the solution of this differential equation, the Stewart-McCumber parameter is introduced as,

$$\beta_C = \frac{2\pi R^2 I_0 C}{\Phi_0} \tag{2.12}$$

The favorable limiting case for a non-hysteric behavior of the junction is obtained in the case of *strongly overdamped limit* ($\beta_C \ll 1$) in which the junction capacitance is negligible and hence

reduces to RSJ (Resistively Shunted Junction) model [30]. For the fabrication of dc SQUIDs, this model is most widely used. However, influence of the parasitic capacitance of the dc SQUID are shown to have certian influence on the I-V characteristics in practice, hence on the stable biasing of the dc SQUID [31].

In the RCSJ model, the junction capacitance is analogue to the inertial term which is assumed to be negligible in the RSJ model. Hence reducing the bias current from above I_C, get trapped instantly in one of the minima of the non-inertial washboard potential at $I_B = I_C$, giving rise to a non-hysteric I-V characteristics, just like a particle get trapped instantly in one of the minima of the tilted washboard. The RSJ model is realized in dc SQUIDs by an external shunt resistor R connected in parallel to each of the Josephson junctions. For the optimum performance of the SQUID with minimum hysteresis, the shunt resistor should be small enough to give $\beta_C \leq 0.7$ [32]. Figure 2.5 shows the simplified schematic of a shunted dc SQUID where the self capacitance C and a resistance R are connected in parallel to the SQUID.

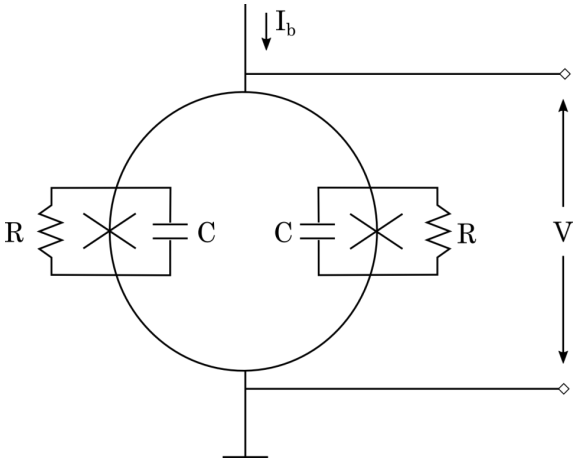

Figure 2.5: Schematic of a dc SQUID described by the RCSJ model. The crosses indicate the weakly coupled Josephson junctions.

In the early stages of SQUID development, rf SQUIDs were preferred to dc SQUIDs because they were easier to fabricate by using a simple point contact instead of two identical weak links on a single loop. However J. Clarke *et al.* showed that the energy sensitivity of the dc SQUIDs can be improved by using external shunted junctions, outperforming the rf SQUID at 4.2 K [30]. This finding together with the development of thin film technology where planar dc SQUID with an integrated multi-turn input coil are placed on a small semiconductor wafer made dc SQUIDs more preferred in applications requiring high resolution. Today nearly all commercial LTS (low temperature superconductor) SQUIDs are dc SQUIDs. However the energy sensitivity of both types of SQUIDs are comparable in case of higher temperatures and rf SQUID are attractive for many high temperature based SQUID applications [33].

2.3.2 DC SQUID as a Magnetometer

A dc SQUID can be operated in small signal mode for the detection of a magnetic flux, where a small variation in the magnetic flux coupled with a biased dc SQUID produce a voltage across the

SQUID. This voltage may be amplified by low noise preamplifier to measure a detectable voltage at the output. This method is not applied in practical readout schemes, since the sinusoidal flux to voltage characteristic limit the linear relation of voltage to applied flux to a very small flux range - hence limiting the dynamic range of the system. The schematic of the operation of the dc SQUID biased above the critical current and the resulting $V-\Phi$ characteristics are shown in figure 2.6. The linear flux range in the $V-\Phi$ characteristics can be described by Φ_{lin} with a maximum slope at the mid point as shown in figure 2.6(c) where typically the working point W for the SQUID operation is set.

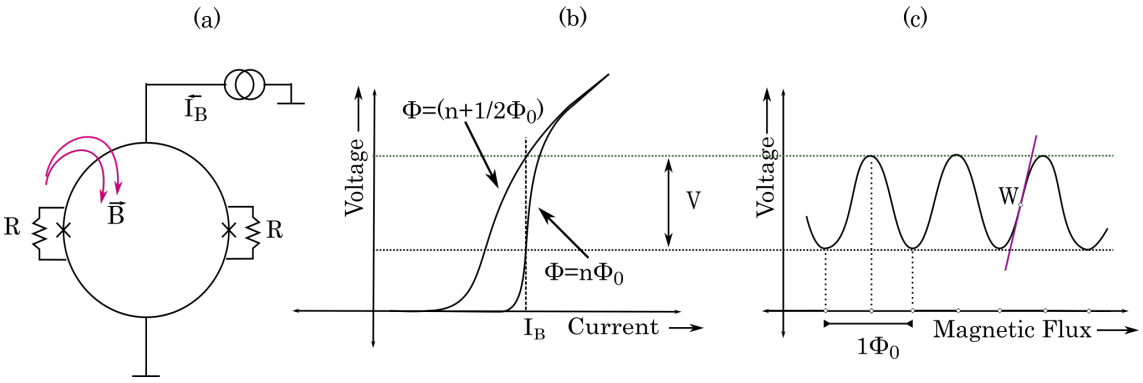

Figure 2.6: (a). Typical I-V characteristic of the non-hysteretic SQUID with a bias current I_B applied just above the critical current of the junction at zero flux coupling the SQUID loop (b). When a field equivalent to $n\Phi_0$ is applied to the SQUID loop, the critical current of the junction will be at maximum. The critical current goes to a minimum at a flux $n+1/2\Phi_0$. W shows the point in the $V-\Phi$ curve with maximum slope where the working point of the SQUID is set (c).

For a sinusoidal $V-\Phi$ characteristic, the linear flux Φ_{lin} region ($\pm\Phi_{lin}/2$ on either directions) can be approximated as ,

$$\Phi_{lin} = \frac{V_{pp}}{|V_\Phi|} \lesssim \frac{\Phi_0}{\pi} \tag{2.13}$$

This equation is valid in case of a small external magnetic flux $\delta\Phi$ (considerably less than Φ_{lin}) coupled with the dc SQUID which is biased at the working point W. The working point is defined by the bias values V_B ,Φ_B , and I_B. The flux causes a deviation in the current δI through the SQUID and therefore a deviation in the voltage across the SQUID. This voltage deviation is related to the deviations in the current and flux by,

$$\delta V = V_\Phi \delta\Phi + R_{dyn}\delta I = V_\Phi(\delta\Phi + M_{dyn}\delta I) \tag{2.14}$$

where V_Φ is the transfer coefficient for a constant current through the SQUID $I = I_B$. The transfer coefficient is the slope of the $V-\Phi$ curve at the working point. Obviously the transfer coefficient is maximum at the center of the $V-\Phi$ characteristics. R_{dyn} is the voltage/ current relation (dynamic resistance) of the SQUID at a constant applied flux Φ. M_{dyn} defines the current sensitivity which scales with the inductance of the SQUID.

To measure the flux coupled to the SQUID, two schemes are applied following the small signal operation described by equation 2.14. The first scheme is to use the SQUID as a flux to

voltage converter in *current bias mode*. In this scheme, a constant bias current is passed through the SQUID and the voltage across the SQUID is measured as shown schematically in 2.7 (a). In this case, applying $\delta I = 0$ in equation 2.14 gives that $\frac{\delta V}{\delta \Phi} = V_\Phi$. Alternatively one can also keep the voltage across the SQUID constant and measure the current I through the SQUID in *voltage bias mode*. In this case the SQUID acts as a flux to current converter with a transfer coefficient $\frac{\delta I}{\delta \Phi} = -\frac{1}{M_{dyn}} = \frac{V_\Phi}{R_{dyn}}$ at constant bias voltage V_B (shown in 2.7) Though both bias schemes are widely used in practice, since the preamplifier noise is fed directly back into the SQUID in the case of voltage bias, maximum achievable system bandwidth is smaller compared to current bias.

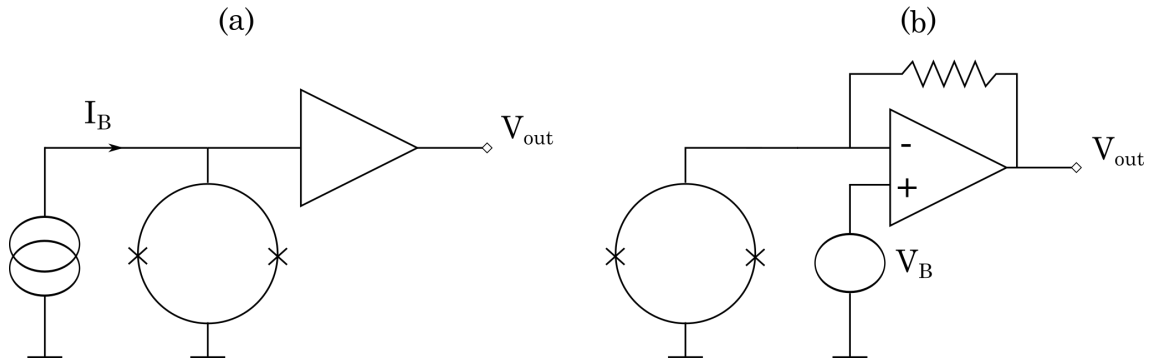

Figure 2.7: Schematic of the two small signal operational modes of SQUID. Current bias scheme where the SQUID is working as flux to voltage converter (left) and voltage bias scheme with trans-impedance amplifier (right).

2.3.3 Noise Influence on the SQUID performance

Generally the noise behavior of the SQUID is characterized by the flux noise, which can be estimated from the total voltage noise associated with the SQUID. The characterization of the SQUID must be done at a specific temperature of operation and its particular loop inductance. Since it is required to take the bandwidth into account, the noise typically is expressed in terms of spectral density, which is the root mean square of the noise magnitude per unit frequency interval. The spectral density of the flux noise is given in $\Phi/\sqrt{Hz}$. Alternatively in case of current measurements using CCC, current noise is also often used in terms of $\mathrm{nA}/\sqrt{\mathrm{Hz}}$.

Detailed computer simulations are required to precisely estimate an overall noise figure associated with a dc SQUID due to a large number of parameters required to characterize it. However an estimate of the relative weight of the different parameters can be approximated by considering only the most dominating source of these noise which is the thermal noise in the shunt resistors. For a dc SQUID operating at a temperature T and in optimum conditions, the thermal noise produce a noise current through the SQUID. The spectral density of this current $S_I(f)$ at a frequency f is given by the Johnson-Nyquist formula,

$$S_I(f) = \frac{4k_B T}{R} \tag{2.15}$$

where k_B is the Boltzmann's constant and R is the shunt resistance of the SQUID.

The thermal noise appear as a white noise (frequency independent) on the frequency spectrum. Another white noise source arise from the critical current fluctuations which produce a circulating noise current around the SQUID loop inducing noise into any input circuit coupled to it. At liquid ^4He temperature ($4.2\,K$), the flux noise of the low-T_C SQUIDs is in the order of $1\,\mu\Phi_0/\sqrt{Hz}$ [34].

In an ideal dc SQUID with identical Josephson junctions, exactly half of the applied bias current flows through each of the Josephson junctions. However, this current distribution, in real case is subject to statistical fluctuations [35]. These fluctuations cause another noise contribution, called $1/f$ noise (also called 'flicker noise') due to its inverse dependence on frequency. $1/f$ noise is prominent at very low frequency ranges, typically below 0.1 Hz. A second major source for $1/f$ noise in the SQUID is the motion of magnetic flux lines which are trapped within the body of SQUID. The$1/f$ noise is predominant in high-T_C Josephson junctions. It is at least 3 times larger than what observed in low temperature junctions [36].

Most of the practical SQUID devices are cooled by the liquid helium bath cryostat. Even though the cryostat holding this cryogenic system is normally designed to bear very low thermal load on to it this thermal load along with the measurement electronics, the system undergoes certain thermal fluctuations. Larger thermal fluctuations can potentially break the Josephson coupling above a certain limit. To keep a reasonable degree of Josephson coupling, this limit is normally given as the thermal noise to be less than the average junction current, with maximum critical current I_{max} as indicated in figure 2.4. For a first approximation, the thermal noise current I_{th} can be given in terms of the temperature T by [30],

$$I_{th} = \frac{2\pi}{\Phi_0} k_B T \tag{2.16}$$

From equation 2.16, for a dc SQUID working at $4.2\,K$, this limit corresponds to an average current of 176 nA. However in the normal operating conditions, the equivalent noise current should be less than an order of magnitude. In general the conditions for optimum SQUID performance (with lowest possible noise energy)can be summarized as follows,

- **Bias Current**: The slope of the $V - \Phi$ curve is largest at a bias current just above the critical current of the junction, $2I_C$. Hence the bias current should be set just above the critical current of the SQUID.

- **Flux Bias**: The flux to voltage transfer coefficient is maximum at $(2n+1)\frac{\Phi_0}{4}$. So for optimum bias, the flux bias should be close to this value.

- **Critical Current**: The junction critical current should be much larger than the thermal noise current to avoid deterioration of V_Φ. Typically for the dc SQUID working at 4.2 K, the critical current should be greater than $1\,\mu A$.

- **Loop Inductance**: For the optimum performance of the SQUID at a given temperature, the thermal noise flux should be considerably smaller than Φ_0 . The thermal energy $k_B T$ causes an rms thermal noise flux in the loop,

$$< \Phi_{th}^2 >^{1/2} = \sqrt{k_B T L_S}$$

The loop inductance of the SQUID also has to be kept low so that a sufficient coupling of the phase difference of the two junctions is possible. Another condition to avoid the non-hysteric behavior of the junction in the $V-\Phi$ characteristics following the discussion in the previous section is given by keeping the screening parameter $\beta_L(=\frac{2I_CL}{\Phi_0}) < 1$. This condition can again be satisfied by keeping the loop inductance of the SQUID sufficiently low. However in case of practical dc SQUIDs, a combination of asymmetry between two arms of the SQUID loop and a damping resistor can improve the transfer function even over the optimal value of the symmetric SQUID and are widely applied in practical dc SQUIDs which have screening parameter β_L typically above 5.

- **Shunt Resistance**: As described in the previous section, to avoid hysteresis in the I-V characteristics, the Stewart-McCumber parameter must be <1. Though this can be done by choosing a shunt resistor smaller than the resistance of the SQUID, the shunt resistance has to be large enough to avoid reduced voltage amplitude of $V-\Phi$ characteristics. Hence normally the shunt resistance is chosen so that $\beta_C \simeq 0.7$.

2.4 SQUID Electronics and Flux Locked Loop Mode of Operation

The SQUID should be able to operate over a wide range of input magnetic field, typically much more than an equivalent flux of one Φ_0. To achieve a wide dynamic range with stable operation independent of the working point fluctuations, the dc SQUID is usually operated in the Flux Locked Loop (FLL) mode. In this mode of operation, the SQUID is set to detect zero (or constant) net flux by compensating any change in flux coupled to the SQUID via negative feedback. In this way it is able to measure a field corresponding to a tiny fraction of Φ_0.

Two schemes widely used in FLL mode of operation are flux modulation and direct coupled readout-scheme. While the flux modulation scheme is commonly in many different applications, the direct-coupled feedback scheme - as a simplified modification of flux modulation - is mostly used in commercial SQUID electronic readout systems,(especially wide band and multi-channel systems) because of simplicity, low cost and low power consumption.

The principle of flux modulation is schematically shown in figure 2.8. A square-wave modulation[2] at a frequency f_{mod} (typically around $100\,kHz$), which is periodically switched between two adjacent working points W^+ and $W^-$is set to the positive and the negative slope respectively in the $V-\Phi$ characteristics. If the applied flux is zero, the output of the SQUID and hence the signal measured will be zero. If a flux change is introduced, a step-up transformer increases the corresponding SQUID voltage and is further amplified, rectified and given to the lock in amplifier (referenced at f_{mod}). The lock in amplifier detects this voltage at the modulation frequency. The signal is then integrated and an equivalent current is fed back to the feedback coil via a feedback resistor R_f. Hence the feedback coil which is inductively coupled to the SQUID (by the mutual inductance M_f) compensates any change in the external flux by threading an equal and opposite flux in to the SQUID. The output voltage, which will be a linearized signal, is measured across

[2]Sinusoidal signal can also be used, but with slightly higher noise level[37]

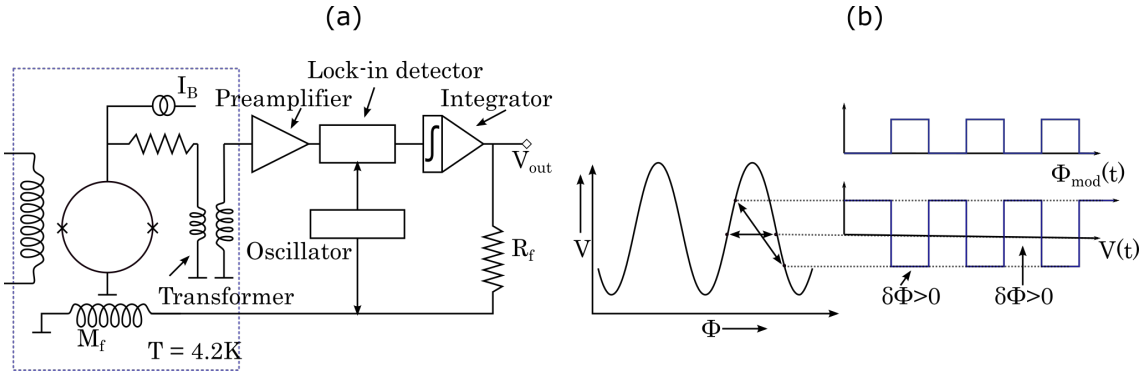

Figure 2.8: SQUID readout with flux modulation: (a) FLL circuit and (b) V–Φ characteristic. A square-wave modulation flux mod switches the SQUID periodically between working points W + and W − . The area shown within dotted rectangle is working at 4.2 K.

the feedback resistor. A small resistance is provided between the SQUID and the step-up transformer to avoid the SQUID being shortcut by the transformer. The turn ratio of the transformer is chosen in a way that the dynamic resistance matches the optimum source resistance to the preamplifier. A detailed description of the flux modulation scheme can be found in Ref [37].

In the direct-coupled readout scheme, the cooled transformer and the flux modulation is avoided. The SQUID is biased at a single working point W as in the case of small signal mode. The deviation in the output voltage due to the applied magnetic field is amplified, integrated and fed back into the SQUID inductively via a feedback coil of mutual inductance M_f (see figure 2.9). Assuming infinite gain of the integrator, the applied flux is compensated by the feedback loop and hence the SQUID is working as a null detector. The voltage V_O across the feedback resistor R_f which is linearly dependent on the applied flux is measured at the output.

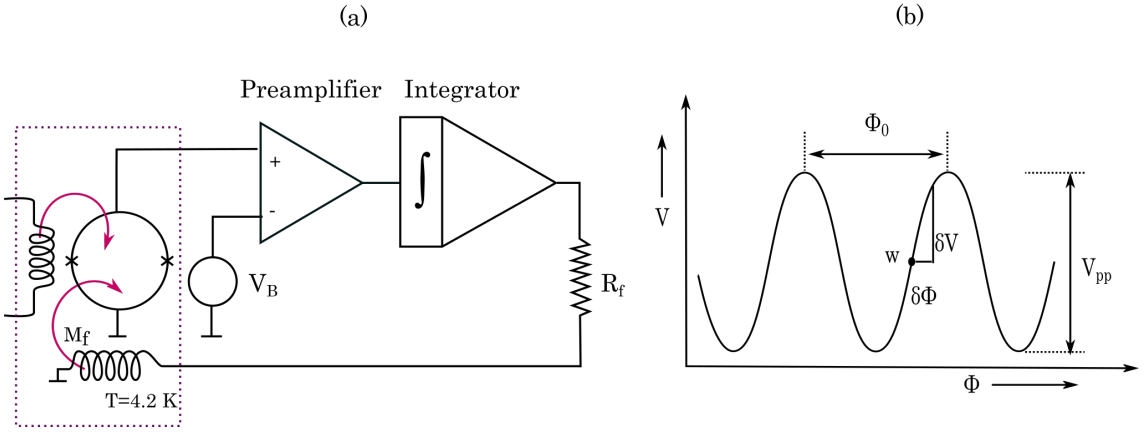

Figure 2.9: Simplified schematic of a basic direct-coupled readout circuit operated in voltage bias scheme (a). Flux - voltage characteristics at constant bias voltage V_B (b).

An advantage of using directly coupled readout scheme is that the SQUID can be operated at a well defined point in the $V - \Phi$ characteristics where the noise is very low. In flux modulation scheme, a modulating flux with peak to peak amplitude of $\Phi_0/2$ is applied to the SQUID and hence the noise is a measure of the averaged noise over this region of SQUID dynamics. Although

in direct coupled readout preamplifier white noise and $\frac{1}{f}$ noise are in principle higher, these effects can be reduced significantly, by additional positive bias and bias reversal techniques [37]. Typically the resistance of the feedback resistor R_f is in the order of several $k\Omega$ to keep the impedance of the feedback coil insignificant. Another advantage of directly coupled scheme is that since ac modulation is not required, high bandwidths are easily achievable.

2.4.1 Noise Figure and Sensitivity in FLL Mode of Operation

The noise in the dc SQUID systems are quoted differently in the SQUID community based on its application area. Generally the noise figure is given by power spectral density in terms of magnetic flux sensitivity ($\Phi_0/Hz^{1/2}$), energy sensitivity (J/Hz), field sensitivity ($T/Hz^{1/2}$) or field gradient ($T/cm \cdot Hz^{1/2}$). The distinction between these terms are important because a system with a SQUID having excellent energy sensitivity can still posses poor field sensitivity due to the readout electronics. Generally while the energy and flux noise define the figure-of-merit of a bare SQUID, complete measurement system is often described by its field sensitivity as its figure-of-merit. In case of beam current measurements using CCC, the performance of the SQUID can be described by its current sensitivity ($nA/Hz^{1/2}$) along with the flux noise.

Equivalent flux noise is the first parameter to describe the noise in the SQUID system, the power spectral density of which at a frequency, f is given by,

$$S_\Phi(f) = \frac{S_V(f)}{V_\Phi^2} \tag{2.17}$$

where $S_V(f)$ is the intrinsic flux voltage noise density of the SQUID. The noise energy ε is also a fundamental parameter of the dc SQUID which basically describes the noise of a bare dc SQUID and is given by,

$$\varepsilon = \frac{S_\Phi(f)}{2L_S \cdot k^2} = \frac{S_V(f)}{2L_S \cdot k^2 \cdot V_\Phi^2} \, [J/Hz] \tag{2.18}$$

Here, L_S is the inductance of the SQUID and k is the coupling constant between the SQUID and the input coil. For the planar dc SQUIDs with integrated multi-turn input coil, a coupling constant in all practical calculations can be assumed to be one. . As it can be seen from equation 2.18, for maximum energy resolution at a given voltage noise, the loop inductance and the flux to voltage transfer coefficient have to be maximized.

For the dc SQUID system in FLL mode of operation, the flux noise can be described as the sum of the noise contributions from the bare SQUID noise, the preamplifier voltage noise, $S_{V,amp}$ and current noise, $S_{I,amp}$ and is given by,

$$S_{\Phi,FLL}(f) = S_\Phi(f) + \frac{S_{V,amp}(f)}{V_\Phi^2} + \frac{S_{I,amp}(f) \cdot R_{dyn}^2}{V_\Phi^2} \, [\Phi_0^2/Hz] \tag{2.19}$$

In FLL mode, the transfer coefficient is nearly independent on the working point W of the SQUID, but it depends mainly on the feedback resistor R_f and the mutual inductance M_f. Dynamic range can be easily increased by reducing the feedback resistance R_f or by increasing the mutual inductance M_f. Often the dynamic range of the SQUID readout system is limited by

the resolution of the analog to digital converter (ADC). The noise level measured by SQUID is often several order of magnitude below the Least Significant Bits (LSB) of standard ADC's. This problem can be solved by setting the feedback range of the integrator to integer multiples of Φ_0 using a reset circuit. The integrator will be reset each time the applied flux exceeds the feedback range and the corresponding Φ_0 steps are counted. With the counted number of flux quanta combined with the ADC output, measurement a very high resolution is possible. A detailed description of the SQUID and direct-coupled readout unit used for the measurements in this thesis is presented in section 3.4.2

The dynamic performance in the FLL mode can be described by considering the SQUID readout unit as a simple model consisting of an ideal dc SQUID, a preamplifier and an ideal integrator. As long as the total flux coupled to the SQUID loop $\delta\Phi = \Phi - \Phi_f$ is within the limit $\frac{\pm\Phi_{lin}}{2}$, the SQUID behaves like a linear element with the transfer coefficient V_Φ, where Φ and Φ_f are the applied input flux and Φ_f is the feedback flux respectively. If G_S is the gain of the SQUID loop and G_E is the gain of the electronic unit, the total FLL gain can be split up into two parts as,

$$G_S = V_\Phi \cdot \frac{M_f}{R_f} \tag{2.20}$$

$$G_E = \frac{f_{GBP}}{jf} \tag{2.21}$$

Here the term f_{GBP} is the gain bandwidth product of the complete feedback electronic unit consisting of the preamplifier and integrator at a frequency f, j is the imaginary unit.

2.4.2 Feedback Schemes

One of the main challenges of SQUID readout schemes is the noise level of the room temperature preamplifier used to amplify the SQUID signal. This noise level (given by the second term in equation 2.19) is often much higher than the intrinsic noise levels of dc SQUIDs. To make the preamplifier noise considerably lower than the intrinsic noise, the transfer coefficient has to be increased. In the flux modulation scheme, the cooled step-up transformer is used in front of the preamplifier to achieve this. In case of direct-coupled readout scheme, the transfer coefficient is enhanced by the use of Additional Positive Feedback (APF).

The APF scheme is schematically shown in figure 2.10. It consists of a serially connected resistor R_{APF} and an inductor L_{APF}, the inductor being magnetically coupled to the SQUID loop via the mutual inductance M_{APF}. Considering the case of a dc SQUID set up at a working point W giving the maximum transfer coefficient V_Φ and assuming that the working point is set at the positive slope in the $V - \Phi$ curve, any change in the external flux produces a voltage V across SQUID, which again produces an equivalent current in the inductor L_{APF}. This current induces an additional flux in the SQUID loop enhancing the flux to voltage coefficient. In the same way, the SQUID set up in the negative slope of the $V - \Phi$ curve enhances the transfer coefficient, resulting in a strongly asymmetric $V - \Phi$ characteristic. An efficient way is to use a cooled field effect transistor (FET) as a tunable APF resistor [38].

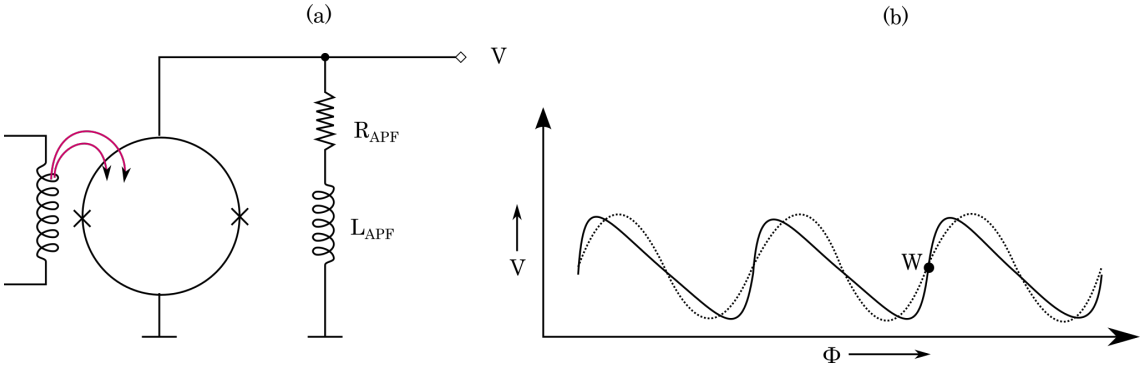

Figure 2.10: DC SQUID with additional positive feedback scheme for the increase of transfer coefficient (left). Modified $V - \Phi$ characteristics in the APF scheme, dotted line shows the sinusoidal behavior which is steepened as shown by solid line at the working point W(right).

Due to capacitive effects in the preamplifier current noise, given by the third term in equation 2.19 is dominant at low frequencies. With APF, however this noise contribution remains not influenced. To further reduce the preamplifier current noise the Bias Current Feedback (BCF) technique can be used. In this scheme, a bias current feedback coil is connected in series to the SQUID, coupling magnetically to the SQUID loop with a mutual inductance M_{BCF}. Assuming a current noise δI causes a voltage δV in the SQUID loop via the dynamic resistance of the SQUID. Due to the magnetic coupling between the SQUID loop and the BCF coil, any change in voltage δV produced in the SQUID loop can be canceled by the BCF coil at correct polarity. Hence a zero net dynamic resistance of the SQUID can be achieved around the working point so that no excess voltage noise from the preamplifier current noise across the SQUID is present.

As described in section 2.3.3, the major source for $1/f$ noise is the statistical fluctuations in the bias current distribution. As the direction of this noise corresponds to the polarity of the bias current the $1/f$ noise can be reduced by periodic inversion of the bias current polarity. SQUID readout schemes normally incorporate the so called bias reversal schemes to minimize any $1/f$ noise influence. In this scheme, the bias current is modulated with an alternating signal at a frequency f_B which is higher than the $1/f$ corner frequency, which one would measure in the case of static bias. Different bias reversal schemes are applied in practical dc SQUID readout units, some of which can be found in ref. [35, 39, 40].

A complete schematic of the direct-coupled dc SQUID electronics is discussed in section 3.4.2.

2.5 Principle of a Flux Transformer

In most of the practical applications of SQUID, the direct coupling of the SQUID to the magnetic flux is not practically possible, either due to the large area of measurement or the excessive interference of the field at the point of interest or simply for geometrical reasons - prime example for this situation is the case of beam current measurements. A higher effective area in the SQUID loop increases the field sensitivity, but increases the intrinsic noise of the SQUID at the same time. To reduce the flux noise of the SQUID, typical effective areas of SQUID sensors usually have a size in the range of 10^{-4} to 10^{-2} mm^2.

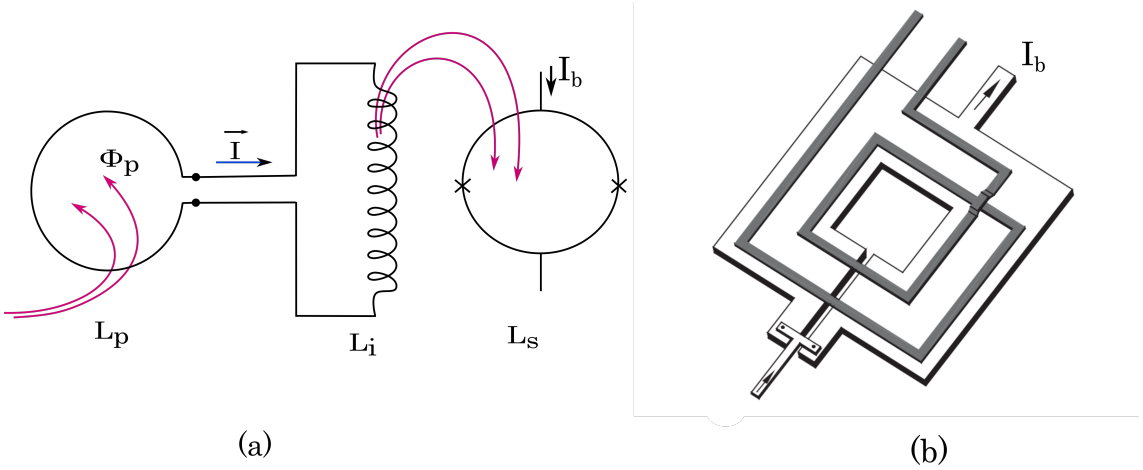

Figure 2.11: (a) Schematic representation of external magnetic flux coupled to the SQUID through flux transformer. (b) Model of the input coil of a flux transformer integrated to the dc SQUID. The Josephson junctions of the dc SQUID are located at the outer edge of a square washer and is biased using a dc current I_b. Only two turns are shown in the image for simplicity, however a large number of turns are introduced in practical dc SQUIDs. Figure courtesy, Ref. [32]

One way to achieve large effective detection area maintaining a low flux noise is by using a superconducting flux transformer as shown in figure 2.11. The flux transformer is a closed loop with the primary coil acting as a pick up coil (with the inductance L_p). It detects the flux and is then coupled to the SQUID through the input coil via the mutual inductance $M_i = k_i\sqrt{L_s L_i}$. L_s and L_i are the inductance of the SQUID and input coil respectively. For simplicity, the noise voltage induced in the flux transformer due to the current noise in the SQUID is ignored. Ideally the inductance of the SQUID in presence of the flux transformer is reduced, so it is also neglected in this case. For a superconducting closed loop, a small flux change $\delta\Phi_p$ at the pickup coil will produce a persistent shielding current J_s following the flux conservation,

$$\delta\Phi_p + (L_p + L_i)J_s = 0 \tag{2.22}$$

This shielding current produces an equivalent change of flux in the SQUID loop $\delta\Phi_s = M_i|J_s|$, which is given by,

$$\delta\Phi_s = \frac{k_i\sqrt{L_s L_{ii}}\delta\Phi_p}{(L_p + L_i)} \tag{2.23}$$

A small change in the external magnetic field δB_{ext} produce a flux change in the pick up coil given by,

$$\delta\Phi_p = \delta B_{ext} \cdot A$$

where A is the area of the pickup loop. Hence the external field sensitivity for a single turn pickup coil can be expressed as:

$$B_{ext}(f) = \frac{1\,(L_p + L_i)}{A\,k\sqrt{L_i L_s}}\Phi_s \tag{2.24}$$

To optimize the sensitivity of the system the natural selection would be to choose the minimum value for equation 2.24. Hence choosing $L_p = L_i$, that is matching the inductance of the pick up coil and the input coil to each other maximizes the sensitivity of the detection system. The equation 2.24 also shows that the resolution of the magnetic noise field can be increased by increasing the size of the pickup coil. Since the area of the pickup coil is fixed due to geometrical reasons, a given L_p in equation 2.24 provides maximum field sensitivity if $L_i = L_p$. Hence from 2.24, the optimized flux sensitivity of the flux coupling loop can be given by,

$$\Phi_{ext,n} = \frac{2}{k}\sqrt{\frac{L_p}{L_s}} \cdot \delta\Phi_{ns} \tag{2.25}$$

Although selecting the inductance of the input coil will give optimum flux coupling with the pickup coil, this method has practical limitations. The input coil is normally integrated into the SQUID microchip to maximize the coupling with the SQUID (Hence the input coil coupling factor can be taken as unity in practical purposes). An efficient method of optimization is adding a superconducting flux transformer to the flux coupling circuit like shown in figure 2.12. By introducing a coupling loop (matching transformer) in between the input coil and pickup coil, the inductance can be matched. The optimum coupling can be achieved by adjusting the turn-ratio of the primary and secondary winding of the flux transformer. Another means for optimizing the coupling is by using fractional turn pickup coils [41] used in several applications.

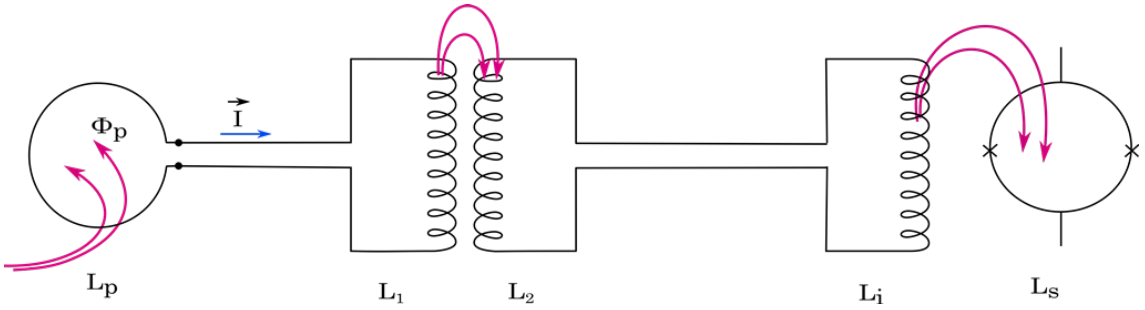

Figure 2.12: Schematic of a typical superconducting flux transformer circuit used in the CCC

By expanding equation 2.24 with the inductance of the flux transformer and using flux conservation theorem, flux sensitivity of the flux transformer circuit can be written as [42],

$$\Phi_{ext,n} = \frac{(L_p + L_1)(L_2 + L_i) - M_f^2}{M_f} \cdot M\Phi_{s,n} \tag{2.26}$$

where, M_f is the mutual inductance of the flux transformer which is given by, $M_f = k_f\sqrt{L_1 L_2}$. With k_f being the coupling factor and assuming $k_f < 1$, the optimized condition for the minimum flux noise can be obtained when,

$$L_1 = \frac{L_p}{\sqrt{1 - k_f^2}};\ L_2 = \frac{L_i}{\sqrt{1 - k_f^2}} \tag{2.27}$$

This gives the condition,

$$\frac{L_1}{L_2} = \frac{L_p}{L_i} \tag{2.28}$$

The inductance L_1 and L_2 of the flux transformer can be written in terms of corresponding current flowing through the superconducting loops as,

$$\frac{L_1}{L_2} = \frac{n_1^2 \cdot I_p}{n_2^2 \cdot I_i} \tag{2.29}$$

From equations 2.26 and 2.27, the flux sensitivity of the system can be written as,

$$\Phi_{ext,n} = \frac{\sqrt{1 - k_f^2} + 2}{k_f k_i} \sqrt{\frac{L_p}{L_s}} \Phi_{s,n} \tag{2.30}$$

Hence by using the matching transformer, optimum coupling between the pickup coil and the SQUID sensor is realized by adjusting the turn-ratio of inductors L_s and L_p. From the equation 2.30, it is also evident that if a matching transformer is introduced instead of direct flux coupling, the coupling factor k_f also has to be taken into account for the optimum coupling [43].

Chapter 3

The GSI - CCC Prototype

The first Cryogenic Current Comparator was developed by I. K. Harvey [44] in 1972 for the precise measurement of dc current and resistance ratios. With this system, he achieved an accuracy better than 0.01 ppm using an rf SQUID. Based on this concept a CCC was developed at Physikalisch-Technische Bundesanstalt (PTB), Berlin for measuring electron beam current produced by a van de Graff generator. This CCC system comprised of an rf-SQUID and was able to measure a beam current of $108\,nA$ [45]. The investigation showed that with a strong shielding to isolate the beam's magnetic field from the environmental magnetic field components, the SQUIDs can be used in an accelerator environment for the precise beam intensity measurements. Following these developments, a CCC was developed at GSI by A. Peters *et. al* [16] in 1992 for the online measurement of heavy ion beam current down to nA range.

With a dc SQUID, "$UJ\,111$" and associated FLL electronics designed and manufactured at the Friedrich-Schiller University, Jena, Germany [46], the CCC system was successfully used to measure ion beam currents. Several test measurements were carried out during the period, 1995 to 1999 [16, 47, 48]. A beam current down to $10\,nA$ was measured with a current resolution of $250\,{}^{pA}/\sqrt{Hz}$ [48].

Since it provides an excellent workbench for further investigations, the old CCC system was upgraded to work as a prototype for the development of new system for future facilities. With improved vacuum and cryogenic units and with an advanced sensor and electronics, this system was recommissioned and is installed in the beam diagnostic test bench at the slow extraction section of GSI synchrotron, SIS18.

The technical concept of the recommissioned GSI - CCC prototype is presented in the first section of this chapter. In the second section, detailed mechanical concepts and cryogenic considerations are presented. Different parts of the CCC system are classified into cryogenic and vacuum unit, sensor unit, cryogenic pickup unit and data acquisition unit and are presented in the succeeding sections. A brief note on the mechanical vibrations and their characterization is presented, however detailed analysis of the influence of mechanical vibrations on the CCC installed in the beamline are discussed in the fourth chapter.

3.1 Technical Concept of the CCC System

Due to available infrastructure and space, the cryostat for the CCC had to be a 'stand alone' solution, which was mountable on a support in standard height (1.8 m) of the GSI beamlines. The vertically installed outer vacuum chamber of the CCC system has two arms extending to the beam line from its cylindrical vessel on either side as schematically shown in figure 3.1. The central part of the CCC system is the liquid helium bath cryostat housing the cryogenic pickup and sensor units. The special design of the cryostat includes a "warm-hole" passing through its center for the passage of ion beams to be measured. The cryostat is designed to provide minimum possible thermal load on to the cold mass. This ensures longer measurement time and more importantly reduces thermal fluctuations at the sensor components due to the boiling of liquid helium. These thermal fluctuations have a huge impact on the current measurements as discussed in chapter 5. A super-insulated radiation shield (which is open to the beam vacuum) isolates the liquid helium cryostat from the outer vacuum chamber. Moreover the radiation shield also acts as a Faraday cage to shield the sensing components from electromagnetic interferences. Mounted on the top of the cold head of a Gifford-McMahon (GM) refrigerator, the radiation shield is kept at about $32 - 50\,K$ depending on the temperature of the cryostat.

Electrical feed-throughs and liquid helium inlet and exhaust lines are isolated from the beam vacuum by vacuum sealed flex-lines. The helium gas exhaust is connected to the recovery line, where the gas is purified, compressed and preserved for further liquefaction.

3.2 Mechanical and Cryogenic Design

3.2.1 Outer Vacuum Chamber

The outer vacuum chamber of the CCC is a cylindrical vessel of $650\,mm$ in diameter and $1.20\,m$ in height. Two arms of the vacuum chamber is extended to $380\,mm$ on either side of the beamline. Ultra High Vacuum conditions (UHV - of the order of $10^{-7} - 10^{-9}\,mbar$) provide optimum insulation vacuum for the liquid helium cryostat. Hence there is no separate isolation vacuum required for the liquid helium cryostat and is thus directly operated in the beam vacuum. To reduce the influence of mechanical vibrations along the beamline, both sides of the arm are connected to the beamline via thin walled metallic flanges. To further reduce vibrations from the support structure, the vacuum chamber is mounted on four rubber bearings. A GM refrigerator is mounted at the bottom of the vacuum chamber using a vacuum sealed CF flanges with a diameter $150\,mm$.

3.2.2 Enthalpy Cooled Radiation Shield

According to Stefan - Boltzmann equation, the power radiated from a hot surface on to a cold body is given by,

$$P = e \cdot A \cdot \sigma \cdot T^4 \tag{3.1}$$

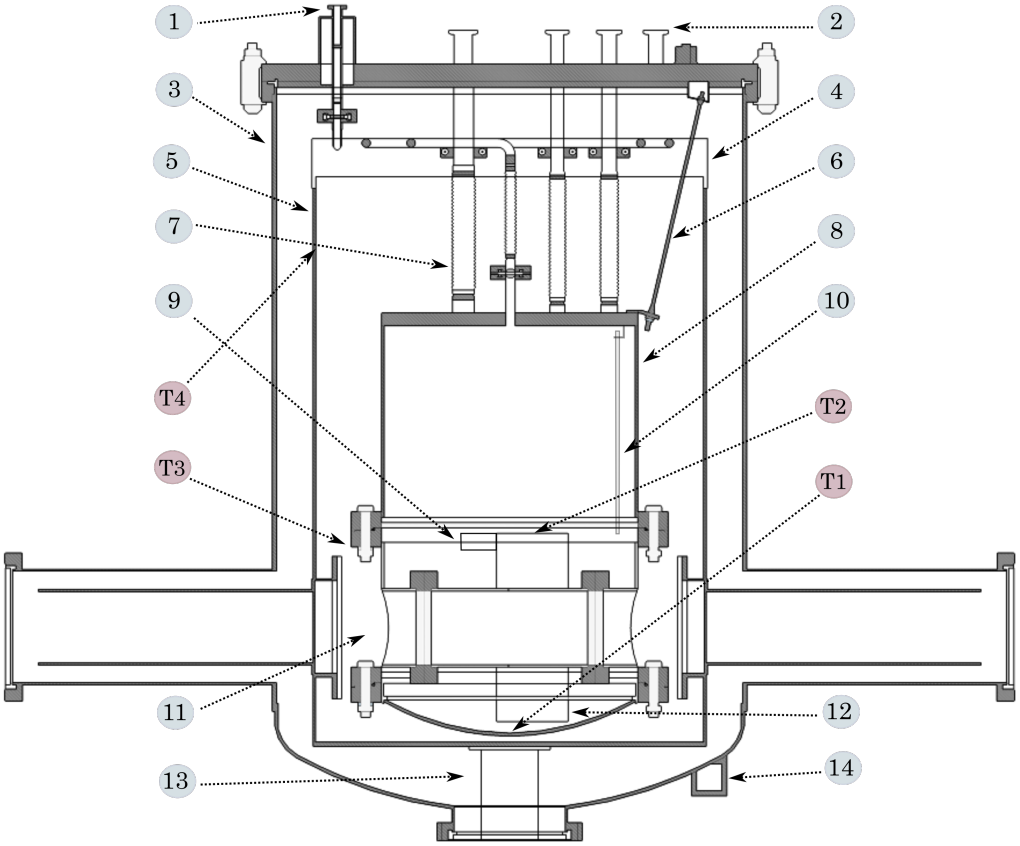

Figure 3.1: Schematic representation of the mechanical setup of a CCC unit

Number	Description
1	Cold helium exhaust connection to the recovery line
2	Feedthroughs (total 4)
3	Outer vacuum chamber
4	Top plate of the radiation shield
5	Radiation shield covered with MLI
6	Titanium Alloy suspension (total 3)
7	Flex lines
8	Liquid helium cryostat
9	dc SQUID cartridge + matching transformer
10	Liquid helium level sensor
11	Warm-hole for the beam passage
12	Superconducting Magnetic shield
13	Cold-head of the G-M refrigerator
14	Rubber bearings (total 4)
T1, T2, T3, T4	Temperature sensors

Table 3.1: Description of various parts of the system numbered in the schematic

where e is the emissivity, A is the surface area and T is the absolute temperature of the hot body. σ is the Stefan Boltzmann constant ($\sigma = 5.67 \times 10^{8}\, W/m^2.K^4$). As it is obvious

from this equation, the heat radiation on the cryostat at $4.2\,K$ by a warm surface at $300\,K$ is 4 orders magnitude more than the heat radiation from a $32\,K$ surface. Hence to reduce the radiative load on the liquid helium cryostat, a radiation shield is placed in between the liquid helium cryostat and the outer vacuum chamber. The radiation shield is a cylindrical copper vessel of thickness $3\,mm$ installed concentric to the vacuum chamber having a space of $5\,cm$ from the vacuum chamber. It is also extended to the beam pipe inside the outer vacuum chamber, hence minimizes the angle of radiation from the room temperature beamline to the liquid helium cryostat.

The shield is cooled down by a single stage GM refrigerator (Oerlikon Leybold Vacuum GmbH, Cologne, Germany). It works in a closed helium gas cycle according to the Gifford-McMahon principle. In this process, helium gas is compressed to a very high pressure (about $24\,Bar$) at a water-cooled compressor unit (Model: RW4000). This pressure is then released in the "cold-head" (Model: RGS 120) by adiabatic expansion removing the heat and hence generating low temperature on the surface of the cold-head [49]. The radiation shield is cooled down to about $50\,K$ with a cooling power of about $50\,W$ at $50\,K$. Hence it acts as a thermal anchor for the liquid helium cryostat.

The high enthalpy of the cold helium boil-off gas is efficiently utilized to further cool down the radiation shield. The boil-off gas is routed spirally around the top plate (cross-cut of the top part as shown in figure 3.2), which cools down the radiation shield to $32\,K$ when liquid helium is filled inside the cryostat with the support of the GM refrigerator. Thermal contact between the top and bottom parts of the radiation shield is enhanced by thick copper strips fixed on both sides.

To improve the thermal insulation of the radiation shield, 30 rounds of Multi - Layer-Insulation (MLI) are wrapped around its outer surface. Each aluminized polymer films are separated by "fiberglass" mesh between the layers. By introducing n layers of MLI, the radiative heat load can be reduced by a factor $n+1$ [50]. The MLI layer is also extended to the two arms extending towards both directions of the beam pipe. With the liquid helium cryostat at $4.2\,K$, the thermal load exerted by the radiation shield was calculated to about $26\,mW$.

3.2.3 Liquid Helium Bath Cryostat

The liquid He bath cryostat is a cylindrical stainless steel vessel with a height of $50\,cm$ and a diameter of $35\,cm$, comprising two massive DN350CF flanges (see figure 3.2). With a liquid helium capacity of $30\,liters$, the cryostat weighs about $100\,kg$. It is suspended by three titanium alloy rods ($Ti-6Al-4V$) of $6\,mm$ thickness from the top plate of the outer vacuum chamber. The low thermal conductivity of titanium alloy suspensions [51] also ensures minimum thermal load on the cryostat (total thermal load was calculated to $12\,mW$). Similarly the flex-lines connecting the cryostat to outside are thin walled stainless steel bellows which have low thermal conductivity at low temperature (thermal load$\approx 5\,mW$ at $4.2\,K$)

The warm-hole of the liquid helium cryostat has a diameter of $100\,mm$ and is equipped with a ceramic gap made of Al_2O_3. The ceramic gap interrupts the parasitic wall currents flowing through the beam pipe which would nullify the beams magnetic field as discussed in section 1.2.1.

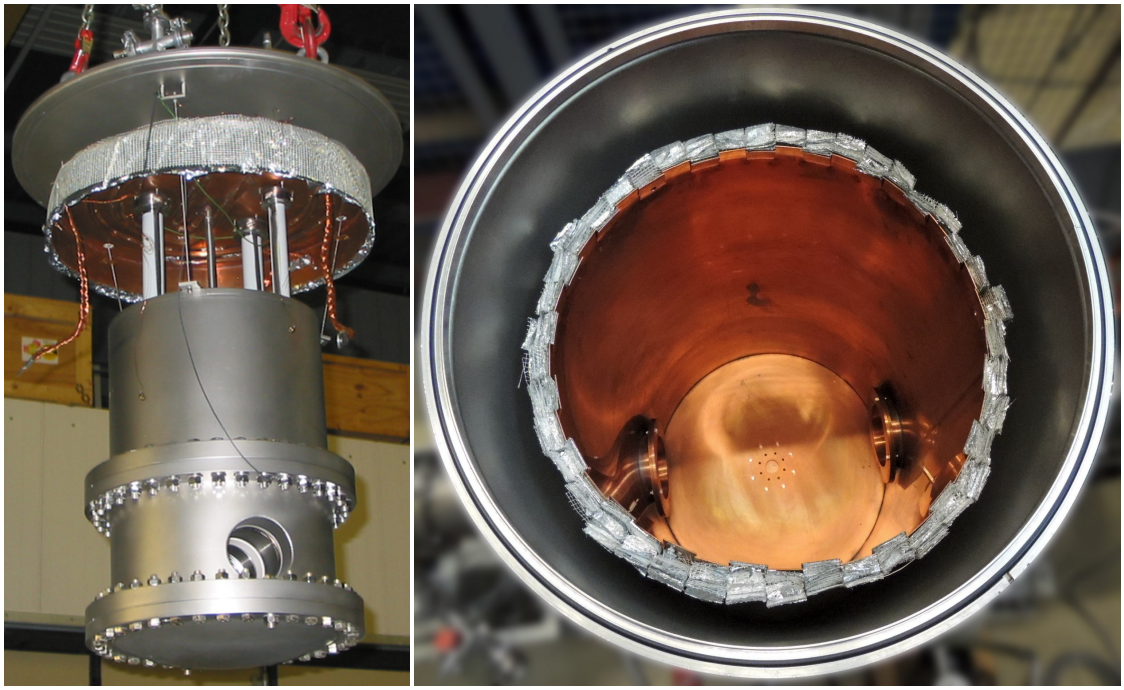

Figure 3.2: Left: Photograph of the liquid helium cryostat which is suspended inside the vacuum chamber. The top plate of the radiation shield with the spirally routed helium exhaust line is also shown. Right (the cylindrical part): Bottom vessel of the radiation shield is covered with multi-layer-insulation. The top and bottom part of the radiation shield are connected by copper strips. The extension of the copper shield into the two arms of the cryostat can be seen at the bottom of the tank.

A bellow on the warm-hole compensates possible thermal contraction/expansion during the cooling cycles. The superconducting pickup unit is fixed on a PEEK (*Polyether ether ketone*) support around the warm-hole. The SQUID cartridge enclosing the dc SQUID and the matching transformer is mounted on the superconducting magnetic shield, which houses the pickup coil and the ring core. The two CF flanges above and below the warm-hole (see the figure 3.2) enable access to the sensor components inside the cryostat for any modification.

The signal measured by the dc SQUID sensor is fed into the room temperature FLL electronic unit via a feed-through stick made of low thermal conductivity German silver (a ternary alloy of copper, zinc and nickel).

3.2.4 Temperature and Liquid Helium Level Control

Silicon diode temperature sensors (Model DT-670B from Lake Shore Cryotronics. Inc. [52]) are used to monitor the temperatures at various locations in the CCC system as marked in the schematic. These sensors help to monitor the temperatures at various stages of cooling down (see section 4.1.1). Temperature sensor T1 measures the temperature at the outer surface at the bottom of the liquid helium cryostat. As the first point to be cooled down while liquid cryogen passage, this sensor indicates the presence of liquid cryogen inside the cryostat. As the liquid helium is filled up in the cryostat, sensor T2, installed at the top of the superconducting magnetic shield (in the same level that of SQUID cartridge) indicates whether the complete sensor and

pickup unit is immersed in liquid helium. Temperature sensor T3 monitors the temperature of the outer surface of the CF flange of the cryostat. While warming up the cryostat, this part warms up at the slowest rate and the sensor ensures the point is at room temperature and the vacuum can be vented. Temperature sensor T4 monitors the temperature of the radiation shield and hence the operation of the GM refrigerator.

A liquid helium level monitor (Model 136 from American Magnetics, Inc.) measures the liquid helium level in the helium container. It measures the helium level by monitoring the linear voltage change produced by a small Niobium-Titanium($NbTi$) wire which turns superconducting when immersed in liquid helium and normal conducting otherwise. The sensor is mounted inside the cryostat with its lowest point at the level of the SQUID cartridge so that the zero point indicates that the sensor unit start to warm up.

With the GM refrigerator keeping the radiation shield at $32\,K$, a total thermal load of $125\,mW$ is exerted on the liquid helium cryostat from various sources. Proper alignment of the warm-hole and two arms of the radiation shield are extremely important while the beam passes through CCC. High energy ion beam incidence on any of these parts can cause blowing up of liquid helium due to heating. Hence precise adjustments are performed to compensate the thermal contraction of the titanium suspensions (estimated to$1.5\,mm$ when cooled down to $4.2\,K$) and on the orientation of the liquid helium cryostat and the radiation shield. Liquid helium is transferred to the cryostat through flexible vacuum jacketed transfer lines from transport canes by standard filling up procedure. The boil-off helium gas is transferred to a helium recycling unit, where the helium gas is purified, compressed and stored for further liquefaction.

3.3 Cryogenic Pickup Unit

3.3.1 Superconducting Magnetic Shield

In principle the magnetic field produced by the beam current can be detected by surrounding the beam with a toroidal coil. However in most cases, the field associated with the beam, will be several orders of magnitude lower than the magnetic noise fields from the nearby equipment and natural sources. To put it into perspective, a beam tube of diameter $100\,mm$ carrying a beam current of $100\,nA$ produces an azimuthal magnetic field of about $0.4\,pT$, compared to an average Earth's magnetic field of $50\,\mu T$. In addition to the Earth's magnetic field component, a number of other stray magnetic field components are produced by, various instrumentation close to the CCC installation locations. These include bending magnets and vacuum pumps and electrical ground loops. These magnetic field components need to be attenuated which is, in case of the CCC, realized with a superconducting magnetic shield.

The superconducting magnetic shield is a parallel arrangement of thin superconducting plates formed into a meander shaped geometry. The step-wise formation of the shield geometry is portrayed in figure 3.3. Following the figure, the superconducting cylinder (a) having a finite length expels field penetrating the surface, by Meissner effect. But the azimuthal magnetic field is present on both inside and outside of the cylinder given by Ampere's law. This cylinder can be folded into a coaxial type from (b) and (c). Hence any non-azimuthal magnetic field components

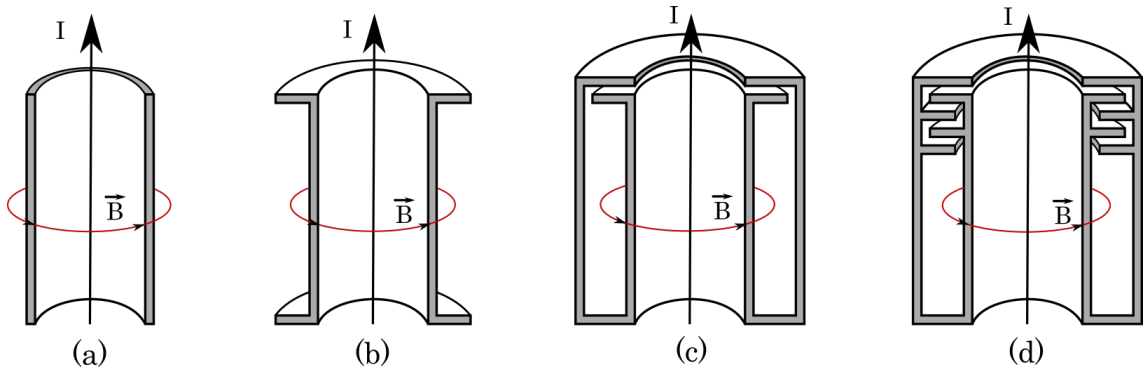

Figure 3.3: Conversion of a superconducting tube (cross-sectional view) into a folded type magnetic shield.

can only be propagated through the tiny slit formed at the opening of the folded geometry at the top. By adding further superconducting plates to form a meander shaped path, keeping a small gap between them (d) one can further improve the shielding against external magnetic field while permitting the azimuthal magnetic field of the beam to be present at the interior. The folded type magnetic shield geometries were proposed and studied analytically by Grohmann, *et. al*, [53]. The study ensures exponential attenuation of any non-azimuthal magnetic field components while passing through the meander shaped geometry while the azimuthal magnetic field of the beam remain unattenuated.

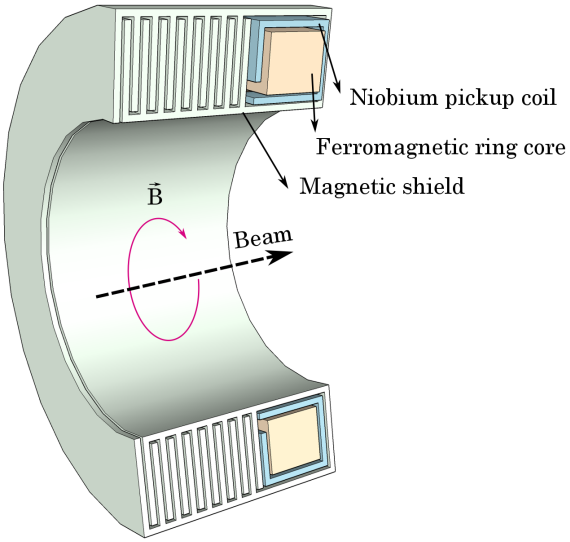

Figure 3.4: Schematic of a superconducting cylindrical cavity as shown in 3.3 transformed into meander shape to form magnetic shield geometry along with the high permeability ring core and niobium pickup coil.

For the realization of the superconducting magnetic shield used in the GSI- CCC prototype, Lead plates (critical temperature,$T_C = 7.2\,K$) were used. With a gap width of $0.8\,mm$ between the consecutive plates, each of them are isolated by Teflon foils. With an inner diameter of $154\,mm$ and an outer diameter of $254\,mm$, the magnetic shield geometry has a total of 10 lead

plates, each having a thickness of $3\,mm$. FEM (Finite Element Model) simulations on the field attenuation showed that for a folded type magnetic shield with 10 meander shaped units, the longitudinal component of the magnetic field undergoes an attenuation of $176\,dB$ [54]. Details on the simulations on the field attenuation and various geometrical influence on it will be discussed in detail on chapter 6.

3.3.2 High Permeability Ring Core

The toroidal ring core of the pick up coil is an important parameter defining the noise level of the CCC system. Heterogeneity in the core material leads to magnetization noise. For the toroidal ring core of outer and inner radii R_a and R_i respectively having a thickness of d, the inductance is given by,

$$L = \mu_0\mu_r \cdot \frac{d}{2\pi} \ln(\frac{R_a}{R_i}) \tag{3.2}$$

where μ_0 is the permeability of free space and μ_r is the relative permeability of the core material. When an ion beam with intensity I_b passes through the center, the superconducting screening current produces a magnetic field B in the pickup coil inducing a current I_s which can be written as,

$$I_s = \int_A \frac{B \cdot dA}{L} \tag{3.3}$$

For an ideal loss-less material at a temperature $4.2\,K$, the current noise I_n due to thermal fluctuations is given by the equipartition theorem [55],

$$I_n^2 = \frac{k_B \cdot T}{L} \tag{3.4}$$

where k_B is Boltzmann's constant and T is the working temperature. Combining equations 3.3 and 3.4 results in,

$$\frac{I_s}{I_n} \propto \sqrt{L} \Longrightarrow \frac{I_s}{I_n} \propto \sqrt{\mu_r}$$

Hence to decrease the current noise, the ring core material should have maximum permeability and low losses. However standard iron powder based composites cannot be used as they exhibit decrease in permeability to about two orders of magnitude when cooled down. In the CCC system, the toroidal ring core was manufactured from amorphous metal "Vitrovac 6025-F" (from Vacuumschmelze GmbH, Hanau, Germany). This material was chosen based on extensive studies by W. Vodel, *et. al.* at FSU Jena, Germany [56]. It shows a high permeability of about $25,000$ at $4.2\,K$ [57].

Generally the toroidal strip wound cores ensure higher uniformity of magnetic domains within the material and reduce eddy currents. Another important figure of merit of the ring cores is

the frequency dependence of the permeability at low temperatures. Extensive studies on the frequency dependence on several ring core materials were carried out by R. Geithner *et.al.*[58, 59], presently Nanoperm material was found to have better performance over a wide frequency range and is planned to be used in the future CCC systems.

3.3.3 Superconducting pickup coil

The superconducting pickup coil is wound around the ring core and is connected to the flux transformer via niobium wires. This geometry covering the ring core emulates a single turn coil which maximizes the flux sensitivity. Made of Niobium, the superconducting pick-up coil has an outer and inner diameters $263\,mm$ and $127\,mm$ respectively with an axial thickness of $130\,mm$. By covering nearly the complete area of the ring core, the pick-up coil also averages out any possible heterogeneity in the ring core and hence the magnetization noise is minimized. Following the discussion in section 2.5, by matching the inductance between the primary and the secondary of the flux transformer (or by choosing proper number of turns), the coupling of the beam signal to the SQUID can be optimized for minimum flux noise or maximum gain.

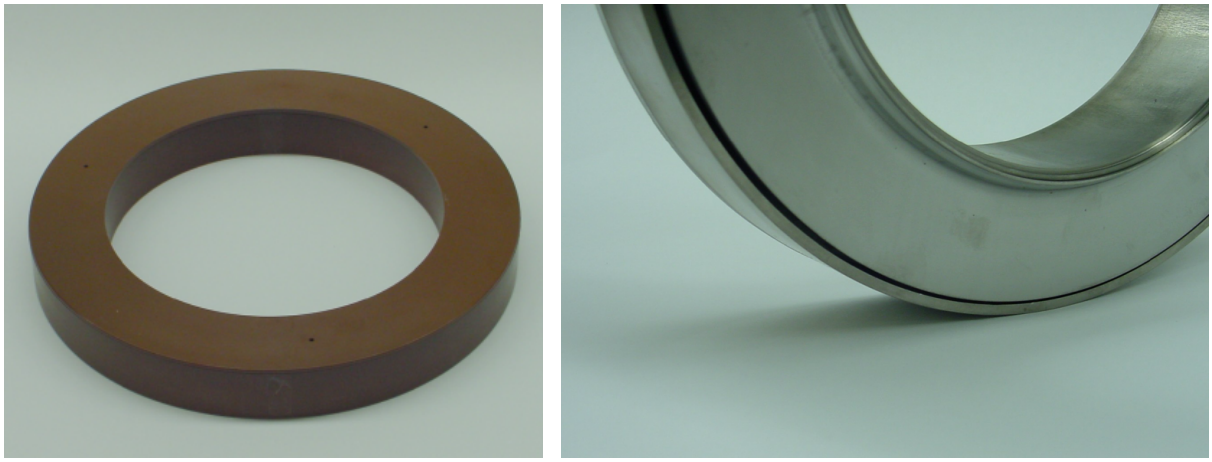

Figure 3.5: Left: Photograph of the high permeability toroidal ring core (Vitrovac 6025-F) housed in a 'Vespel' insulator. Right: Superconducting niobium pickup coil enclosing the high permeability ring core. Image courtesy, W.Vodel [60].

For the GSI-CCC prototype, the pickup unit ($L_P = 37.4\,\mu H$ at $4.2\,K$) and the SQUID input coil are coupled by a flux transformer via superconducting Niobium wires. The flux transformer has inductance values $L_1 = 23.7\,\mu H$ at the pickup coil side (primary) and $L_2 = 0.533\,\mu H$ at the input coil side (secondary), at $4.2\,K$. With these inductance and according to the equation 2.29, the turn radio required for the matching is set to be $7:1$.

3.4 SQUID Electronics and Data Acquisition Unit

Since several CCC units were foreseen at FAIR , the sensor unit was chosen from commercial vendors to allow for a serial production of the advanced CCC unit. The selection of the dc SQUID and FLL electronics were based on the comparative studies done by R. Geithner [17] on several

dc SQUIDs and electronic units. With the smallest current noise level over wide bandwidth, the combination of dc SQUID, "CP2S Blue" (from company Supracon AG, Jena, Germany) and the FLL electronic unit, XXF-1 (Magnicon GbR, Hamburg, Germany) were chosen and installed in the GSI - CCC prototype. With the possibility of remote operation and characterization of the entire SQUID electronics, the FLL electronics provide a wide bandwidth up to $20\,MHz$ [61].

The dc SQUID sensor is mounted on a PCB (as shown in figure 3.6) where the flux transformer unit is fixed and is encapsulated with a niobium cartridge to exclude any interfering magnetic noise fields. The input (bias and feedback circuits) and output signals to the SQUID sensor are controlled by the FLL electronics installed at the top of the CCC vacuum chamber. The SQUID and FLL electronics are connected by a feed-through via 10 pin lemo^{TM}-type connectors on either sides. As the SQUID sensor is highly susceptible to noise due to electromagnetic interference and floating ground loops, an excellent, loop-free ground connection to the whole electronic setup is essential for the proper working of the sensor.

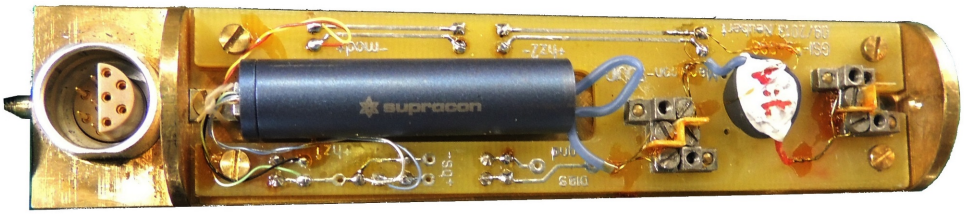

Figure 3.6: Photograph of the dc SQUID sensor 'CP2S Blue' mounted on the PCB (shown in blue colour). The matching transformer is shown at right hand side to the SQUID sensor (in white). The 10 pin "lemo type" connector which connect the SQUID cartridge to the FLL electronics can be seen in the left hand side.

3.4.1 The SQUID Sensor

The SQUID sensor CP2S is a low T_C-dc SQUID chip fabricated from Nb/Al-AlOx/Nb technology. Having a critical current of $22\,\mu A$, the SQUID has an inductance (at open input coil) of $270\,pH$ at $4.2\,K$. The input coil made of niobium wire wound coils are integrated into the SQUID system and has an inductance of $460\,nH$ at $4.2\,K$. This couples the input flux to the dc SQUID with a mutual inductance of $10.5\,nH$. Complete list of parameters of CP2S dc SQUID is given in table 3.2.

The sensor is equipped with a current feedback coil inductively coupled with the input coil that can compensate any coupling of magnetic field with the SQUID loop through a mutual inductance of $21\,nH$. However, the flux modulation coil which is originally provided for the operation in flux modulation scheme is used for the current feedback in our system. Hence instead of coupling the current feedback to the input coil, the current modulation coil directly couples feedback current to the dc SQUID with a mutual inductance of $200\,pH$.

The SQUID microchip shown schematically in figure 3.7 is equipped with two heaters connected via an encapsulated thermal switch. With a current upto $100\,mA$, the heaters can introduce a resistance upto about $30\,\Omega$ in the input circuit thereby removing any flux trapped in the

Parameter	Value
Critical Current, I_C	$22\,\mu A$
SQUID Resistance, R_n	$2.17\,\Omega$
Voltage Swing, ΔV	$25\,\mu V$
SQUID - Feedback Coil Mutual Inductance	$200\,pH$
Flux Feedback Coupling, ΔI_{mod}	$10.5\,\mu A$
SQUID Inductance	$270\,pH$
Input Coil Inductance	$460\,nH$
Input Coupling, ΔI_{EK}	$0.195\,\mu A$
Equivalent Flux Noise, S_Φ	$5.6\,{}^{\mu\Phi}/\sqrt{Hz}$
Maximum heater current to expel frozen flux	$100\,mA$

Table 3.2: Characteristic parameters of the dc SQUID at $4.2\,K$ which is applied in the CCC system

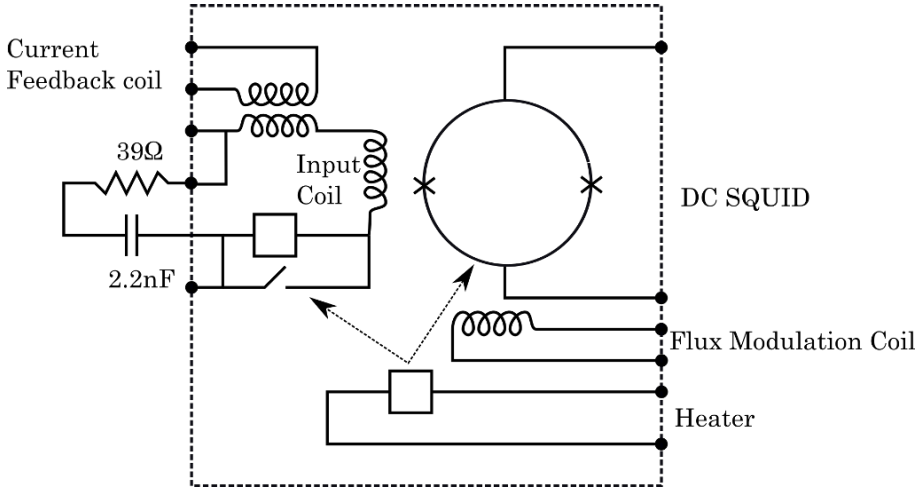

Figure 3.7: Circuit diagram of the dc SQUID installed in the GSI- CCC prototype. The SQUID microchip is shown by the dotted rectangle.

superconducting coils, dc SQUID and the input coil. Trapped fluxes inside the superconducting coils are generated if these coils are cooled down below their critical temperature in presence of magnetic fields (such as Earth's magnetic field components). The presence of trapped fluxes in any of the superconducting coils near the Josephson junctions cause a number of undesired influences on the SQUID performance [62]. The trapped flux can reduce the critical current of the Josephson junction [63] which reduces the voltage modulation. Reduction in voltage modulation substantially increases the white noise level of the sensor. Another influence of trapped fluxes in the vicinity of dc SQUID is the $1/f$ noise originating from the thermal motion of the flux vortices.

3.4.2 The FLL Electronics

The directly coupled FLL electronic unit, XXF-1 amplifies and linearizes of the signal detected by the dc SQUID sensor and produce a measurable output. The working principle of the directly coupled readout scheme is discussed in chapter 2.4. In practice, the electronics box is connected to the SQUID sensor via a feed-through of total length of $72\,cm$. The analog output voltage

($\pm 10\,V$ maximum) from the FLL electronics is fed through a "connector box" via shielded $50\,\Omega$ coaxial cables to the data acquisition unit. Various input/output signals are controlled by a *LabView*® application called SQUID Viewer™. The electronics unit encloses two integrated waveform generators which can modulate the current and voltage sources in the electronics. This signal generators are used for producing $V - \Phi$ oscillations and hence set up the working point of SQUID operation.

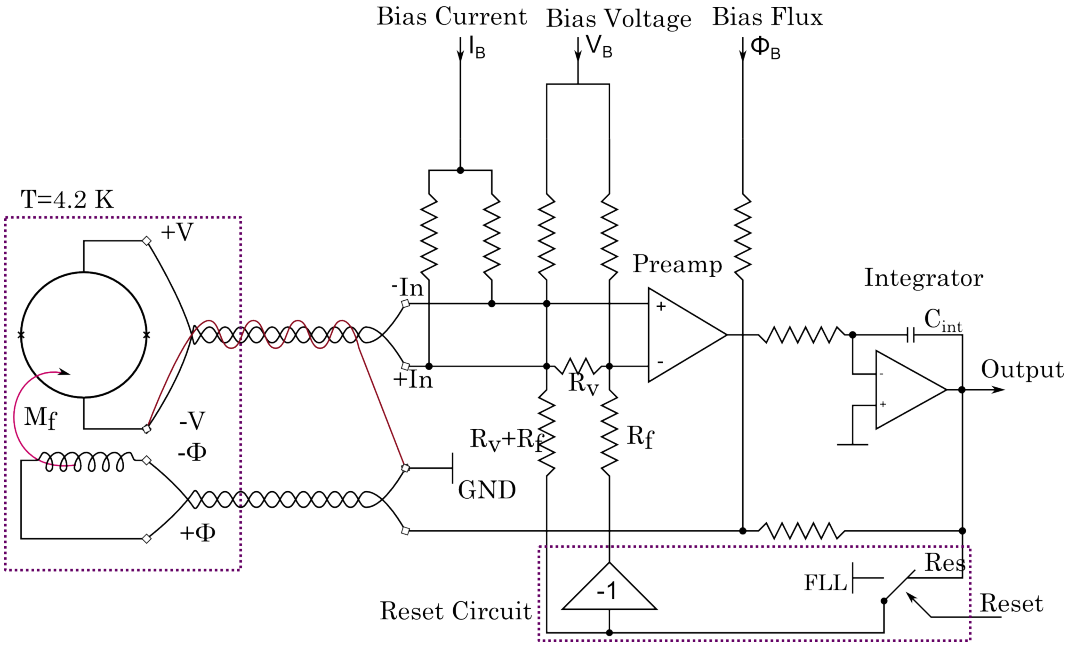

Figure 3.8: Schematic diagram of the direct-coupled FLL electronics with bias reversal scheme. For simplicity, the heater connection, internal generator and the input coil are excluded from the schematic.

The connector box distributes the SQUID signal to the Magnicon XXF - 1 electronics and to the heater at the matching transformer via 24 pin and 10 pin lemo - type connectors respectively. Similar to the heater at the input coil, the heater connection at the matching transformer is also used to remove any trapped fluxes coupling with the matching transformer. With the help of a $100\,\Omega$ resistor, the heater current is adjusted to about 60-70 mA.

The readout system has two modes of operation. The FLL mode and amplifier (AMP) mode. In the AMP mode, the electronics works as an amplifier and hence provides a convenient adjustment of working point. It can also be used as an alternative small signal open loop mode of SQUID readout. In the FLL mode, the SQUID voltage is linearized to get a linear transfer function as discussed. To provide a wide dynamic range, the feedback resistor can be chosen between $0.7\,k\Omega$ and $100\,k\Omega$ and the gain bandwidth product in the range $230\,MHz$ to $7.2\,GHz$. To increase flux gain, additional Positive Feedback (APF) is used to enhance the flux gain at the working point. A simplified circuit scheme is shown in 3.8.

The connector box of the electronics is equipped with an anti-alias filter at the output with a cut-off frequency set to $10\,kHz$ ($\pm 2.5\%$). Enabling this second order Bessel type filters limit the bandwidth of the output signals and thereby reduce the possible high frequency noise at the connector box.

3.4.3 Data Acquisition Unit

The data acquisition unit of the CCC consists of a high resolution oscilloscope and FFT analyzer. The oscilloscope (Model HD4096, Teledyne LeCroy) provides high sample rate with 12-bit ADCs and hence a resolution of 0.024% of the maximum voltage. In addition the oscilloscope is capable of reading out the output at a sampling rate of $2.5\,^{GS}/_{s}$. The high resolution signals from the SQUID readout can be saved for offline data processing. For the measurement of beam current, a remote measurement scheme is employed which will be shown in section 4.2. Combining the pickup and sensor unit, the simplified schematic of the beam current measurement scheme with CCC can be found in figure 3.9

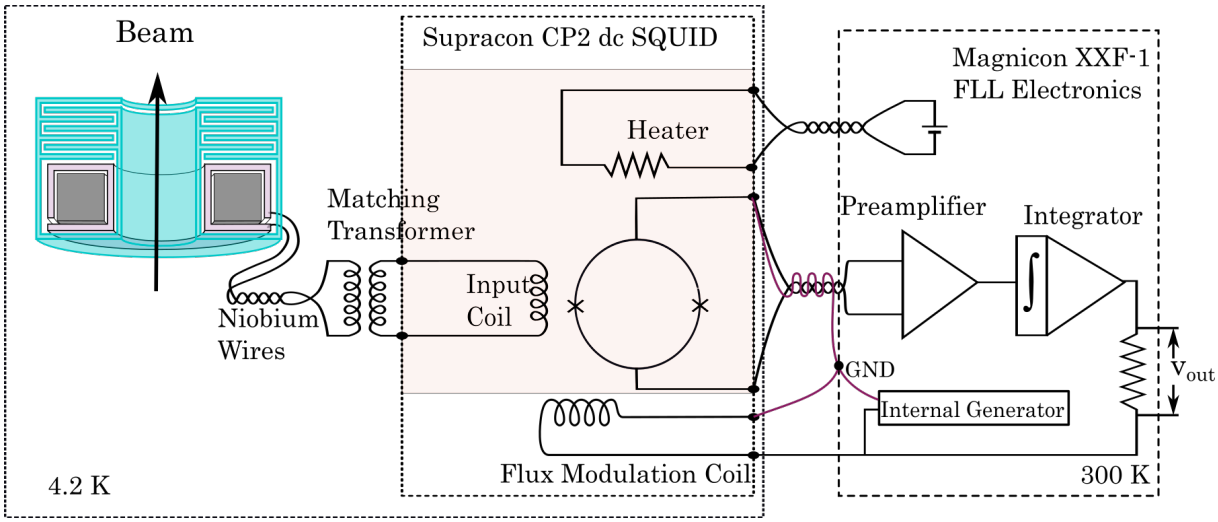

Figure 3.9: Simplified schematic representation of the sensor and pickup unit. The highlighted box in Supracon dc SQUID shows the components in the SQUID microchip. A unique ground connection to all the components are mandatory to minimize zero drifts and noise in the output caused by any difference in ground potentials.

3.5 Final Tests of the Cryostat

3.5.1 Vacuum and Cryogenic Tests

As pointed out before, the cryostat vacuum is directly connected to the beamline vacuum. Therefore before the installation at the beamline, the CCC vacuum conditions need to satisfy the leakage rate specifications. Apart from the typical vacuum leakage limitations, a small leak in the exhaust helium (having the smallest atomic size) vapor can influence beam vacuum conditions. Hence several leakage tests are performed on the cryostat as well as the outer vacuum chamber. CCC is installed in the beamline with an overall leak rate below $10^{-8} mbar/s$.

With minimized thermal load on to the liquid helium cryostat, the CCC was designed and shown to have long "hold time" (~ 3 days) with liquid helium so that a complete measurement campaign can be carried out without further refilling [16]. However test measurements after the re-commission showed a much less liquid helium hold time of about 9 hours. Detailed

investigations converged to possible aging of the copper radiation shield and resulting oxidization which result in reduced thermal emission coefficient.

3.5.2 Mechanical Resonances

Whenever the natural frequency of a system coincide with an external excitation, the system undergoes resonant vibrations. At resonant frequencies, the amplitude of the system's response will be much higher than the amplitude of the excitation. Like any other mechanical systems, each part of the CCC possesses natural modal frequencies given by the geometry and the building materials. Although CCC cannot be completely decoupled from mechanical vibrations, the resonant vibrations need to be suppressed. This can be realized by small geometric or material modifications defining the resonances.

A number of mechanical driving terms can introduce microphonics (mechanical oscillations transformed to electrical noise at the output) in CCC measurements. They are mainly vibrations caused by vacuum pumps, and electrical motors (with well defined frequency as shown in figure 3.10) or broadband (relative to the bandwidth of the mechanical modes) ambient sources. The broadband vibration sources contribute to the noise floor as well as excite the resonant mechanical modes of the system. With extremely sensitive pickup and sensor units, CCC is highly susceptible to all these vibrations. Mechanical vibrations cause superconducting coils inside the CCC system (ring core, flux transformer and the SQUID itself) to oscillate in the presence of magnetic field inducing current noise at the input of the dc SQUID which scales with the magnitude of the vibrations.

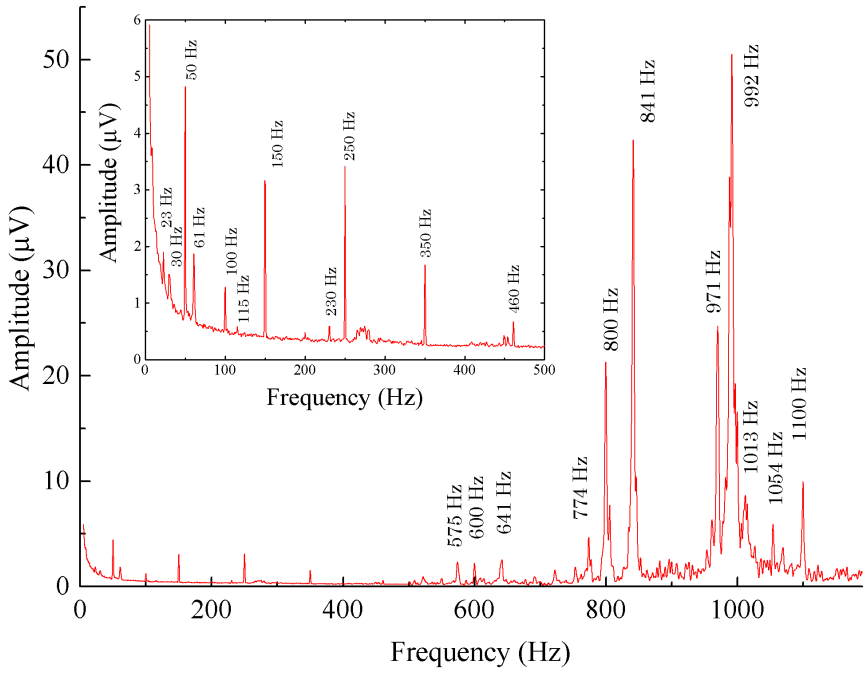

Figure 3.10: Vibration frequency spectrum of the CCC system measured at a typical lab environment. The accelerometer is mounted on the surface of the outer vacuum chamber of the CCC. Inset shows the lower frequency range of the spectrum.

Generally one can consider the vibrations acting on the CCC system as deterministic (the magnitude of the excitation is known) with a measurable set of sources that can cause vibrations coupling with the system. However external vibrations originating from vibration of the building etc. (in our case, FAIR related construction works in the premises were found to be a strong source of vibrations), also causes random vibrations at a given time. Since most of the vibrations can be characterized as periodic, the microphonic noise can be estimated by the frequency analysis. Since the resonant modal vibrations of various components of the system are visible in the frequency spectrum, one can try to identify the origin of a particular peak. By identifying the individual source of resonant vibrations, one can damp them by slight modifications on the geometry or materials, so that the resonant frequency is modified. In the GSI - CCC prototype, efforts were limited to identify the mechanical modes of the system rather than damping them.

The noise caused by the resonant vibration of the mechanical parts of the cryostat normally correspond to low frequencies (typically below $100\,Hz$, at room temperature) and posses $1/f$ characteristics to the frequency. A typical response of an accelerometer mounted on the outer surface of the CCC system is given in figure 3.10. A short impulse (which has a flat frequency spectrum) from a hammer strike excites the resonant modes of the system. The accelerometer (ICP sensor, Model 482A06, PCB Piezoctronics, Inc.) signal is read out to a spectrum analyzer to plot the Fast Fourier Transform (FFT) spectrum.

In the vibration response of the accelerometer, $50\,Hz$ and its harmonics are dominated at low frequencies. These peaks originate from the vibrations of rotating shafts and bearings inside the induction motors which are operated at line frequency, $50\,Hz$. It has to be noted that the induction motors produce magnetic as well as mechanical noise which will be acting independently to the system noise when they are operated in the premises[64]. Frequencies around $30\,Hz$, $61\,Hz$, $115\,Hz$ and its harmonics originate from the mechanical modes of the CCC system itself.

At higher frequency range, frequencies corresponding to $841\,Hz$ and $991\,Hz$ are the most prominent contributions in the noise spectrum. These signals corresponds to various vacuum pumps in the premises of the cryo-lab facility where the frequency response are recorded. Obviously, the spectrum measured by the accelerometer mounted on the outer surface of the vacuum chamber does not take into account the resonant vibration modes of the cryostat and radiation shields at low temperature. However the noise spectrum taken by the dc SQUID output as discussed in section 4.1.4 shows the absence or considerable reduction in the amplitude of most of the frequencies observed by the accelerometer due to mechanical damping.

Chapter 4

Beam Current Measurement with the CCC

With the previous sensor unit replaced by advanced dc SQUID and control electronics, the recommissioned GSI - CCC prototype was installed in the GSI beamline for beam current measurements. In this chapter the performance of the advanced CCC unit in the accelerator environment is characterized and successful beam current measurements of slowly extracted beam are discussed.

A typical measurement campaign of the CCC, already under high vacuum conditions, starts with cooling down of the cryogenic components to $4.2\,K$. This is followed by the preparation of the dc SQUID working point for the optimum performance. The measurement preparation is completed with the calibration of intrinsic output voltage to equivalent current using a precise known current source. In the first section of this chapter, various stages of preparation of the CCC system for the beam intensity measurements are discussed. A complete scheme of the beam measurements and the mechanism of various components involved are presented in the second section.

The beam current measurements using the CCC system are presented in the third section of this chapter. This section starts with a brief explanation of the charged particle beam inside a synchrotron and its slow extraction mechanism. Beam parameters and machine settings used for the extraction of beam from SIS18 to the measurement section of the extraction beamline are discussed in the next topic. In the subsequent parts, measurements of slowly extracted beams using CCC are presented.

4.1 Preparatory Work

4.1.1 Cool Down Procedure

A beam measurement campaign typically starts with filling the liquid helium bath cryostat. The cryostat is filled about an hour prior to the start of measurements so that the thermal fluctuations due to liquid helium boil-off is minimized. Since this mechanically sensitive cryogenic system is suspended inside HV conditions within the accelerator beamline, cooling down is carried out in

several steps. As the first step, the multi-layer insulated radiation shield is cooled down to about $50\,K$ with the GM refrigerator. The GM refrigerator is kept running permanently to reduce the thermal load on the helium container. Only during the measurements the refrigerator is shortly switched off to avoid the influence of its vibrations. With the cryostat still well above $200\,K$, in the second step, liquid nitrogen is filled inside the cryostat so that all sensor components are cooled down to $77\,K$. Liquid nitrogen is used because of two reasons, first it is easily available and less expensive at the same time pre-cooling with nitrogen (with latent heat $161\,^{kJ}/_{l}$) is more efficient means to bring the temperature of the system from room temperature down to $77\,K$than using liquid helium (latent heat $2.6\,^{kJ}/_{l}$).

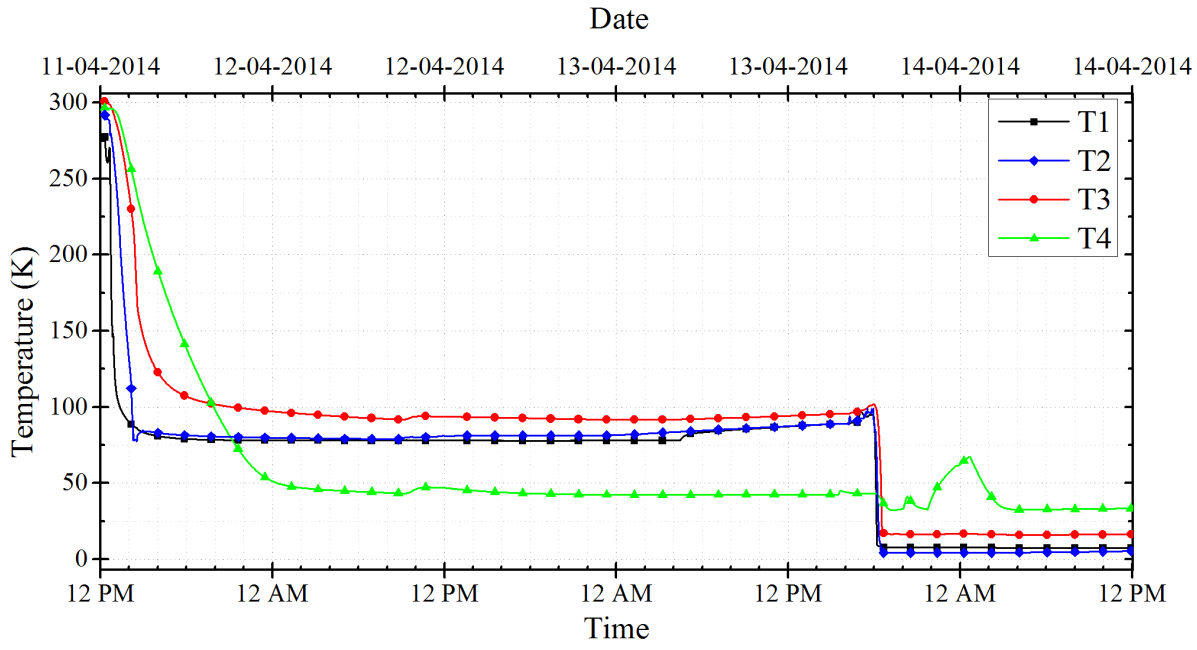

Figure 4.1: Cooling cycle of a typical CCC measurement campaign. In this case, pre-cooling with liquid nitrogen and GM refrigerator were started at the same time. All four temperature sensor locations follow the nomenclature defined in chapter 3.

Once the cryostat is at $77\,K$, entire liquid nitrogen has to be completely removed from the cryostat before further cooling down to $4.2\,K$. To ensure complete removal of nitrogen residue inside, the cryostat is flushed with warm helium gas and pumped out several times. Once the nitrogen is completely removed from the cryostat (indicated by temperature sensors well above $77\,K$), liquid helium is transferred into it using an insulated and evacuated transfer line. During the filling process, the liquid helium level is continuously controlled with the help of temperature sensors and liquid helium level sensor. The temperature record of a typical cool down cycle of the CCC system is shown in figure 4.1. Increase of temperature indicated by the time around 10 PM on 13-04-2014 on the temperature sensor T4, which is connected to radiation shield indicate the starting of a CCC measurement session during which the GM refrigerator was switched off.

4.1.2 Working Point Setup and SQUID Characterization

Once the cryogenic pickup and sensor units in superconducting state, the SQUID electronics can be tuned to its optimum working point. As discussed before, the SQUID transfer coefficient is maximum at the mid point of the increasing or decreasing slope of the flux voltage characteristics. Hence this point is favorable for setting the working point. To produce the $V - \Phi$ modulation, an internal generator, embedded inside the FLL electronics unit is used. The SQUID electronics is operated in the "amplifier (AMP) mode" to display the $V - \Phi$ characteristics. In this mode of operation, the FLL electronic unit acts as an amplifier with adjustable gain between 1100 to 2000. A current signal from the internal generator, that is high enough to produce at least a single flux quantum (Φ_0) in the SQUID loop is applied through the current feedback coil. This produce a periodic output in the FLL electronics as the current in the feedback coil is increased. The electronics also generates a mirror signal of amplitude $1\,Vpp$ (peak to peak) having the same waveform and frequency as that of the internal generator. This signal is read out at the oscilloscope along with the SQUID output and the sum of the two signals produce $V - \Phi$ modulation signal at the oscilloscope. By adjusting the bias voltage and bias flux to (0,0) in the oscilloscope, the feedback coil compensates any voltage at the SQUID and hence corresponds to the optimum working point.

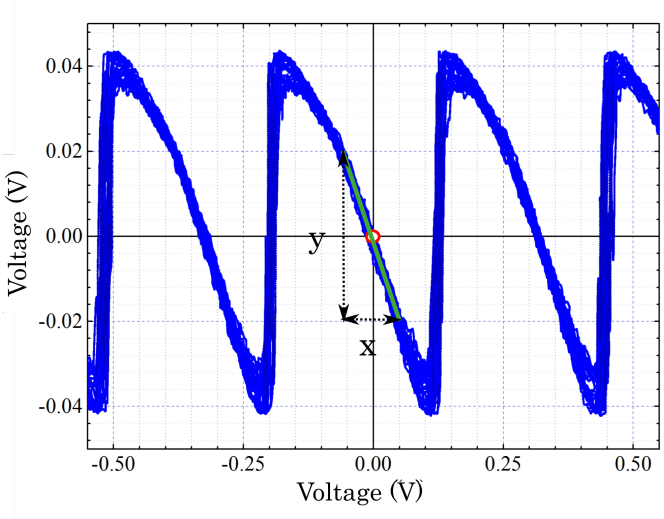

Figure 4.2: $V - \Phi$ characteristics of the SQUID electronics with working point set.

Though a perfect sine wave can be chosen as an optimum behavior of a $V - \Phi$ characteristic curve, the application of additional positive feedback can considerably deform the sine wave eventually increasing the value of transfer coefficient as discussed in section 2.4.2. Once the working point is optimized the sensor unit can be switched to FLL mode. In this mode, the input signal of the SQUID is amplified, linearized and fed back into SQUID via feedback coil, producing an equivalent voltage across the feedback resistor (R_F). With the system working in the FLL mode, proper values for the feedback resistor and gain bandwidth product (GBP) are

selected. As discussed in section 2.4.1, the maximum sensitivity of the system can be achieved by setting the maximum value of the feedback resistor of $100\,k\Omega$ with minimum dynamic range. The GBP value is chosen for the most stable response of the system over the complete range of measurements and is set as $0.38\,GHz$.

The $V-\Phi$ characteristic curve with the system in the amplifier mode is given in figure 4.2. By applying an additional feedback resistance of $10\,k\Omega$, the $V-\Phi$ curve can be deformed such that the slope is increased to obtain higher transfer coefficient. However since the working point turned out to be unstable due to strong noise interferences, it was set at the decreasing side of the curve as shown in the figure.

From the $V-\Phi$ characteristic curve, the peak to peak voltage (V_{PP}) produced by the applied flux is measured to $80\,mV$. This corresponds to a maximum voltage swing of $40\,\mu V$ in the $V-\Phi$ characteristics with an amplification of 2000 in the AMP mode. Similarly, V_{period} - which corresponds to the voltage produced when one Φ_0 of flux coupled with the SQUID - is measured to $0.32\,{}^{V}/_{\Phi_0}$. Within the linear region of the $V-\Phi$ curve, the slope $s = {}^{y}/_{x}$ is measured to 0.3. Based on these values, a number of characteristic parameters of the SQUID and the FLL electronics can be calculated and hence, the gain of the dc SQUID and its $3\,dB$ bandwidth can be estimated.

The first quantity to calculate is the transfer coefficient (V_Φ) of the SQUID, which is the slope of the $V-\Phi$ characteristic curve at the working point and can be estimated as,

$$V_\Phi = \frac{\partial V}{\partial \Phi} = s \cdot \frac{V_{period}}{2000}$$

where the factor 2000 indicates the amplification of the voltage in the amplifier mode. Hence from the $V-\Phi$ characteristics, the transfer coefficient, V_Φ is calculated to $48\,{}^{\mu V}/_{\Phi_0}$. With the mutual inductance M_F between the SQUID loop and the feedback coil, the flux coupled with the SQUID loop by the application of a feedback current I_F is given by,

$$\Phi_{SQ} = M_F \cdot I_F$$

Hence for a unit flux quantum Φ_0 to be coupled to the SQUID, the current required to produce in the feedback coil can be given by,

$${}^{\mathrm{I_F}}/_{\Phi_0} = \frac{1}{M_F}$$

Hence with a feedback resistor in the AMP mode set as $30\,k\Omega$, the reciprocal value of mutual inductance (${}^{1}/_{M_F}$) which is the current required in the flux coupling loop, to produce unit flux quantum in the SQUID can be calculated as ,

$$\frac{1}{M_F} = \frac{V_{period}}{R_F} = 10.67\,{}^{\mu A}/_{\Phi_0} \tag{4.1}$$

From these values, the SQUID gain G_S can be calculated as,

$$G_S = \frac{V_\Phi \cdot M_F}{R_F} = 1.5 \times 10^{-4} \tag{4.2}$$

The $3\,dB$ system bandwidth (the point where the spectral density is half its maximum value) of the CCC system can be estimated from the gain of the SQUID. With the gain-bandwidth product (GBP) set at $0.38\,GHz$, unity gain bandwidth of the system is given by,

$$f_1 = GBP \times G_S = 57\,kHz \tag{4.3}$$

The $3\,dB$ bandwidth of the system can be approximated to the unity gain bandwidth up to $1\,MHz$ [65]. Hence the system bandwidth can be given as $57\,kHz$. However in case of intensity measurements of the slowly extracted beams, measurements typically below $10\,kHz$ are interesting. To reduce the excess noise, the anti-aliasing filter is applied at the output of the CCC signal. The low pass characteristics of the anti-alias filter limit the bandwidth of the measurements to $10\,kHz$. Figure 4.3 shows the noise floor of the signal measured by the CCC and its improvement by the application of the anti-alias filter. Details of measurements without the anti-alias filter are discussed in chapter 5. From the oscilloscope output, the current resolution which corresponds to a signal-to-noise ratio (defined as the ratio of rms amplitude of the signal to the rms amplitude of the noise) of 2 was measured to $2.3\,nA_{rms}$, whereas the signal without the anti-aliasing filter gives a current resolution of $3.6\,nA_{rms}$.

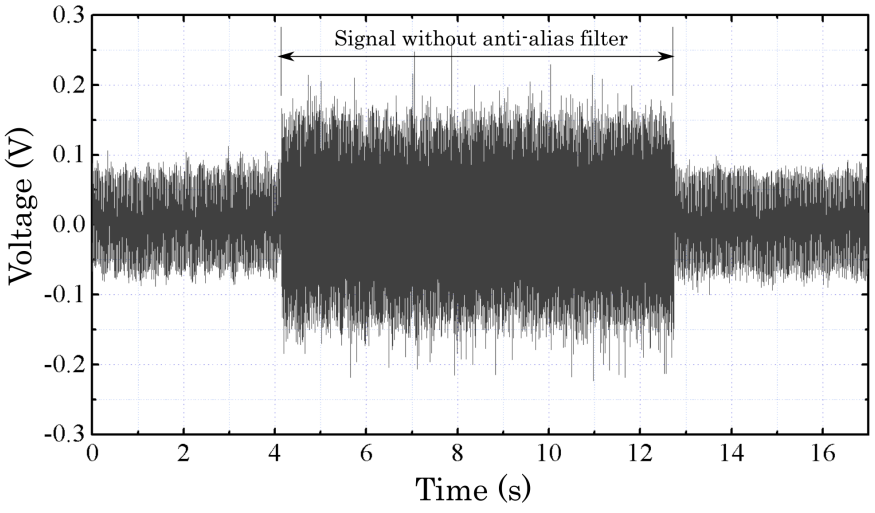

Figure 4.3: The output of the CCC signal measured at the oscilloscope showing the influence of an anti-aliasing filter on the output signal.

4.1.3 Current Calibration

Intrinsically the output of the SQUID electronics is measured as the voltage across the feedback resistor as discussed in the previous chapter. To express the beam signal in terms of current, the output voltage of the SQUID is calibrated to a known current using a calibration loop wound around the magnetic shield in parallel to beam direction.

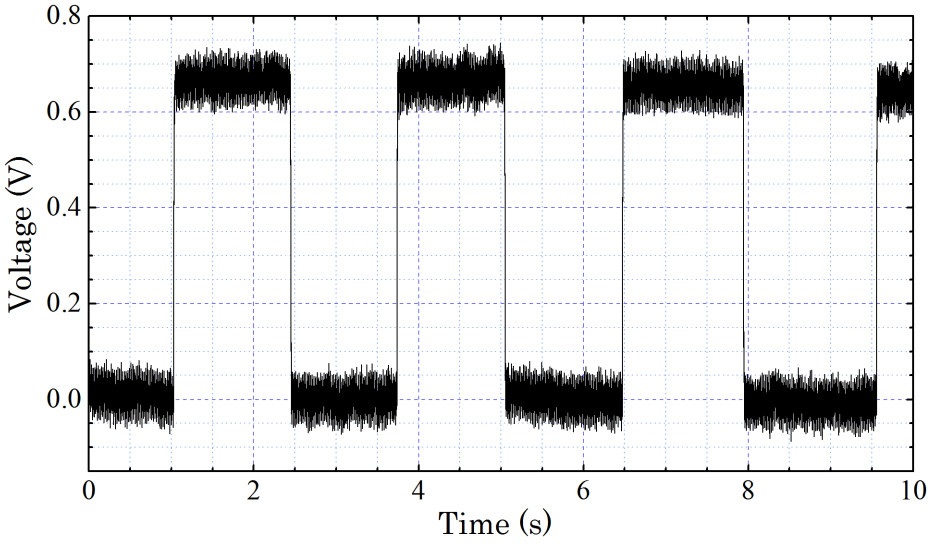

Figure 4.4: Typical response of CCC to a 50 nA test current signal applied through the calibration wire loop.

As shown in section 3.3.1, the magnetic field measured by the pickup unit is independent of the position of the current element. Consequently, a wire loop wound around the magnetic shield geometry produces an azimuthal magnetic field which can be measured by the pick up unit. This magnetic field produced by the current carrying element is comparable to that of an ideal dc beam current. Therefore with an accurate value of the applied current, the output voltage can be calibrated.

For precise calibration of the CCC output to the applied current, the current produced by a precision current source (Keithley 261 picoampere source) is used. The current source has a range of $10^{-14}\,A$ to $10^{-4}\,A$ which can supply the current within an error of 0.1% of the input current at $10^{-11}\,A$. To reduce any influence of external noise signals, the current from the source is applied through a low pass filter having a cut-off frequency $170\,Hz$. Figure 4.4 shows the response of a $50\,nA$ test pulse applied to the calibration wire loop. The SQUID electronics is operated in the FLL mode with a feedback resistor set to $100\,k\Omega$.

From a set of known current values applied in the range of $5\,nA$ to $1\,\mu A$, the CCC system measured the output voltage and this voltage is plotted across the applied current to produce the current calibration plot as given in figure 4.5.

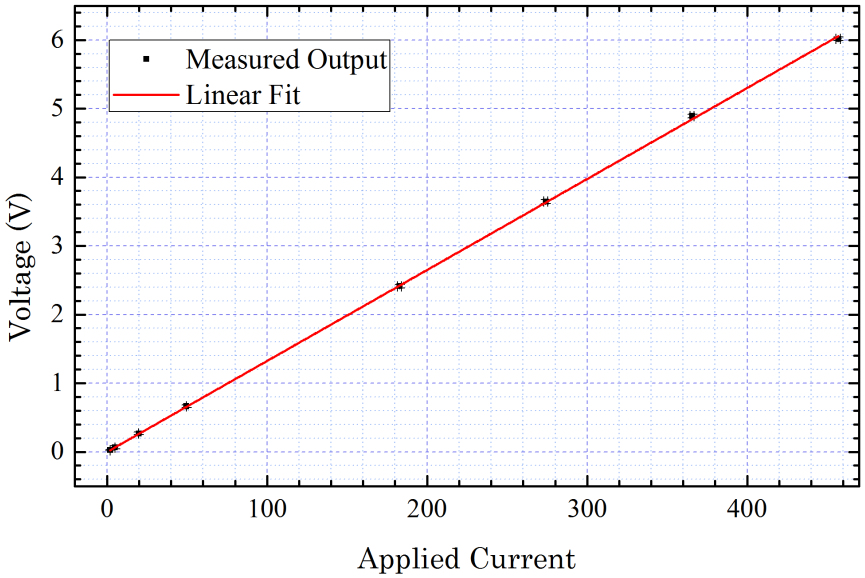

Figure 4.5: Current calibration plot produced by plotting the sensor output voltage against the known current applied through the calibration winding.

From the slope of the current calibration curve, the current calibration factor κ_V with the highest sensitive range of the CCC at $R_F = 100\,k\Omega$ is calculated as $74.2\,{}^{nA}/_{V}$. With a a corresponding output voltage, V_{out} measured at the output of FLL electronics, a current of ${}^{V_{out}}/_{R_F}$ is flowing through the feedback coil. As pointed out before, the current in the feedback coil is required to produce one flux quantum in the SQUID sensoris given by, $\frac{1}{M_F} = 10.67\,{}^{\mu A}/_{\Phi_0}$ The number of flux quanta produced by $1\,V$ output at the oscilloscope as given by,

$$\Delta\Phi = \frac{V_{out} \times M_F}{R_F}$$

It can also be seen from this relation that when a unit flux quantum coupled to the SQUID, a voltage of $1.067\,V$ is produced at the output. From this, the current calibration can also be expressed independent of the feedback resistance value as,

$$\kappa_\Phi = 69.53\,{}^{nA}/_{\Phi_0}$$

The CCC was kept at the same FLL settings (R_F and GBP) throughout the beam measurement campaign so that the calibration values remain unchanged during the complete measurement session.

4.1.4 Current resolution and Flux Noise

To determine the noise characteristics, a noise spectrum of the system was recorded as shown in figure 4.6. To obtain the intrinsic characteristics of the CCC system in the experimental

environment, the output was readout at the HTP beamline. The time domain spectra were recorded with the Oscilloscope (Lecroy HDO 4096) and the fast Fourier transform is taken offline using the data analysis program Origin®. The CCC with its output calibrated, was kept at minimum noise environment with the GM-refrigerator switched off and the electrical feed-throughs of the system such as temperature, LHe level sensors disconnected.

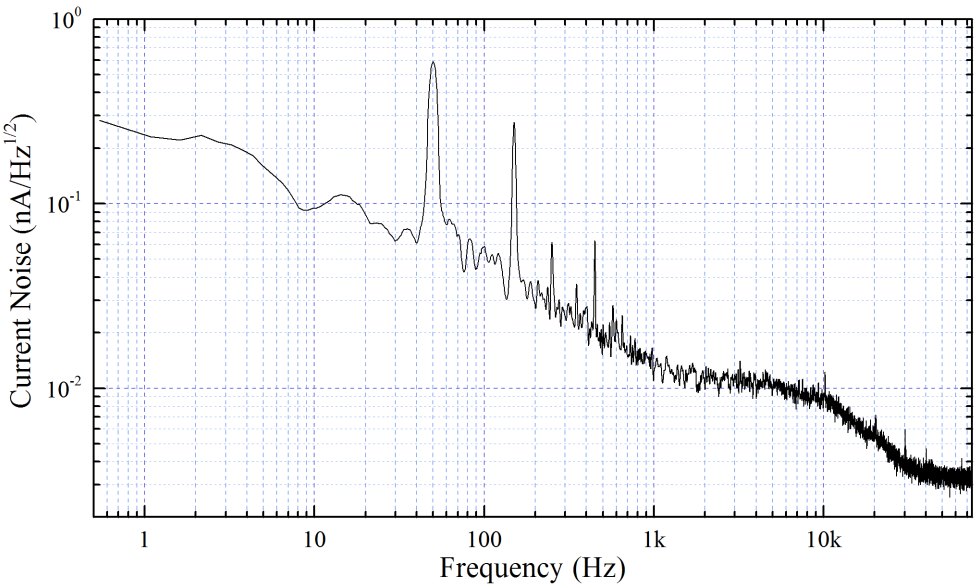

Figure 4.6: Noise spectrum of the CCC system installed in the beamline.

From the noise spectra shown in figure 4.6, the white noise level of 11 $^{pA}/\sqrt{Hz}$ at around $2\,kHz$ corresponds to a flux noise of $80\,\mu\Phi_0/\sqrt{Hz}$. The decrease in the amplitude above $10\,kHz$ is caused by the anti-aliasing filter. Apart from the $50\,Hz$ and its harmonics, peaks corresponding to $62\,Hz$, $574\,Hz$ were the main observable peaks in the spectrum. However, In addition to the intrinsic noise of the ring core, a large number of low frequency noise around the installation such as water supply, air and nitrogen gas supply lines were found to dominate the lower frequency range suppressing the $1/f$ corner frequency which is typically expected below $100\,Hz$.

As an alternative figure of merit of the CCC system, with a flux noise value of $80\,\mu\Phi_0/\sqrt{Hz}$ and the SQUID inductance of $270\,pH$, the energy sensitivity of the complete SQUID readout can be estimated as,

$$\varepsilon = \frac{S_\Phi(f)}{2 \cdot L} = 5.06 \times 10^{-29}\,{}^{J}/_{Hz}$$

4.2 Experimental Setup at the SIS18 Extraction Line

For beam current measurements, the CCC system was installed in the beam diagnostics test bench (beamline section termed as HTP) at the High Energy Beam Transport (HEBT) section

of the SIS18. A number of beam diagnostics devices are installed and tested, the majority of which is for the installation in the FAIR facility. Along with the CCC, standard intensity measurement devices, like Ionization Chambers, Secondary Electron Monitors and Scintillators are installed for various test measurements. Other beam diagnostic installations in the HTP section are an ac beam transformer, a beam loss monitor (BLM) [66], a test setup for Beam Induced Fluorescence (BIF) [67] and Optical Transition Radiation (OTR) measurements , and a mounting ladder for the test of scintillating screen materials.

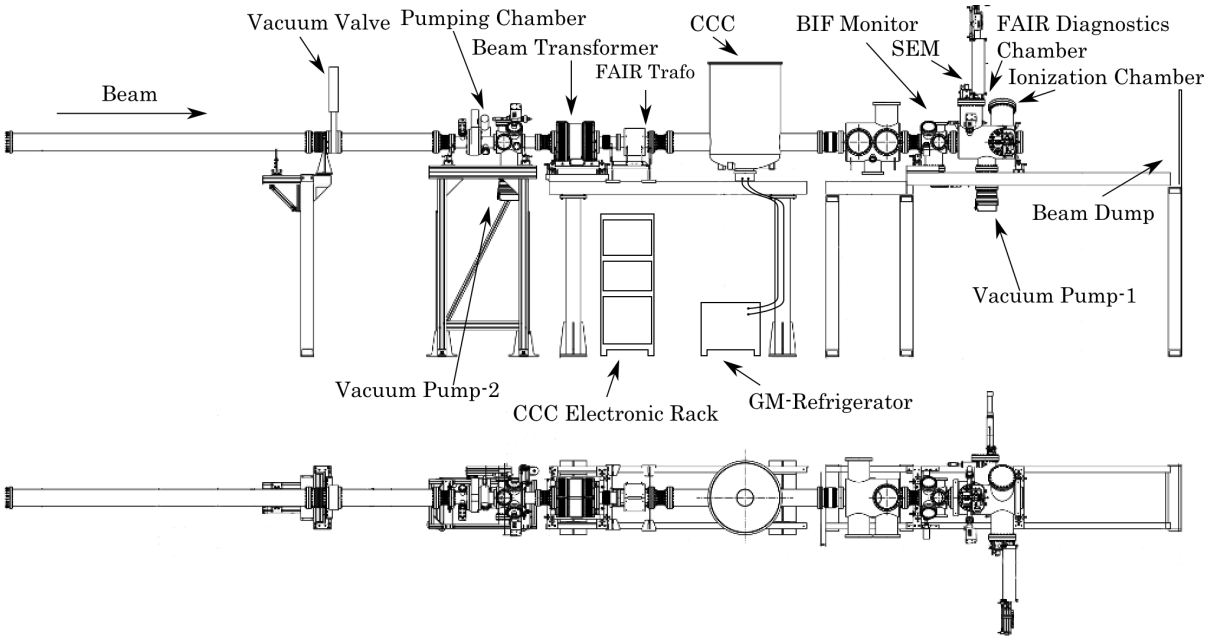

Figure 4.7: Side-view (top) and overhead-view (bottom) of CCC installation in the beam diagnostic test bench, at the extraction section of SIS18, HTP.

The schematic of the instrumentation at the HTP beamline at the time of the 2014 CCC measurement campaign is shown in figure 4.7. From the vacuum point of view, the HTP is equipped with two turbo molecular pumps at both sides of the CCC installation, and one additional pump in the diagnostics box nearby the CCC (see figure 4.7). At the end of the beamline, the ion beam is dumped on to a copper dump (towards right hand side in the image).

For the preparation of the SQUID and electronic system and for current calibration measurements, the output is read out directly to the data acquisition unit at the CCC location. However, for the beam signal measurements and other optimizations during beam experiments, remote measurements are required due to the radiation safety measures. Hence the beam signals are measured at a measurement room about $70\,m$ away from the installation point of the CCC. In case of test measurements at the beamline, the SQUID output is amplified at the FLL electronics and is read out through a connector box to the oscilloscope at the beamline.

In the remote measurement scheme, the signals were amplified using a custom made optically

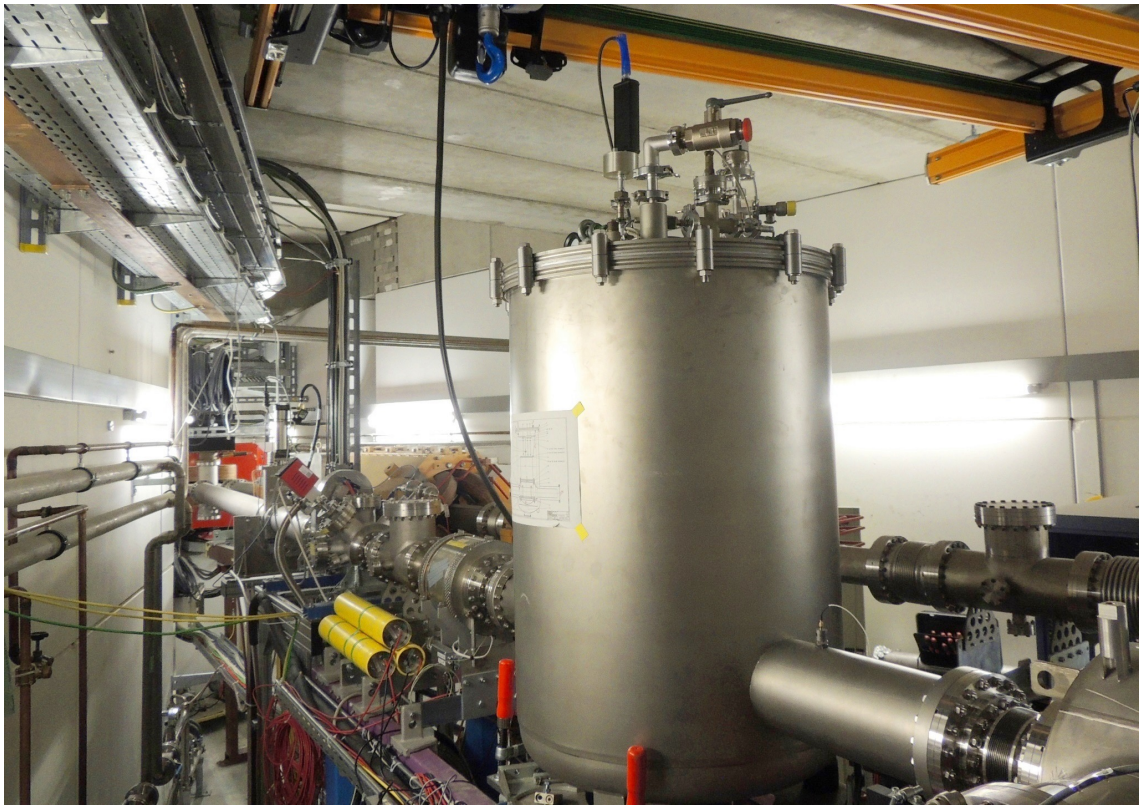

Figure 4.8: Photograph of the CCC system installed in the HTP section. The beam is directed towards right hand side of the image.

isolated amplifier and are sent to the data acquisition system at the measurement room. The amplifier has differential mirror outputs (equal in magnitude but with opposite polarity) which can be averaged at the read out unit. Hence the noise interfering along the long cables from amplifier to the data acquisition unit can be reduced. The amplifier has an output gain of 0.1995 at the differential terminals.

Hence the differential output voltages V_1 and V_2 are read out at the oscilloscope in the measurement room and is combined to give the CCC output as,

$$V_{scope} = \frac{|V_2 - V_1|}{2 \times 0.1995} \tag{4.4}$$

By integrating the spill structure, one can obtain the total charge (total area by integration, A_{spill}) contributing to the beam current. Hence, with the current calibration factor $\kappa_V = 74.2\,^{nA}/_{V}$, the beam current over the extraction time, τ can be given by,

$$I_{beam} = \frac{74.2 \times 10^{-9} \cdot A_{spill}}{\tau} \tag{4.5}$$

The beam signals measured with the CCC are compared with the output of a Secondary Electron Monitor (installed about $1\,m$ downstream from the CCC installation point, shown in

the schematic 4.9). Secondary electron current produced up on the beam passage through SEM foils are amplified by a trans-impedance amplifier (Model No. DHCPA-100, FEMTO Messtechnik GmbH, Germany) which has a bandwidth of $220\,kHz$ to $200\,MHz$ depending on the gain. It has a switchable gain of $1 \times 10^2\,{}^V/_A$ to $1 \times 10^8\,{}^V/_A$ and can be controlled by remote access. By adjusting the gain depending on the beam intensity, the voltage signal corresponding to the secondary electron current is read out at the measurement room along with the CCC output.

The secondary emission current due to the beam passage is given by the Sternglass formula [68],

$$I_{sec} = Y \cdot \frac{dE}{\rho dx} \cdot I_{beam} \tag{4.6}$$

where the term Y is an empirically obtained term which describes the amount of secondary electrons emitted per unit energy loss at the surface of the SEM foil. $\frac{dE}{dx}$ is the mean differential energy loss going directly into the production of secondary electrons and ρ is the density of the *Al* foil.

With the help of the program SRIM[1], the term $Y \cdot \frac{dE}{\rho dx}$ can be calculated for a particular energy and ion species. Hence from the secondary electron current and the gain settings in the trans-impedance amplifier, the beam current can be calculated.

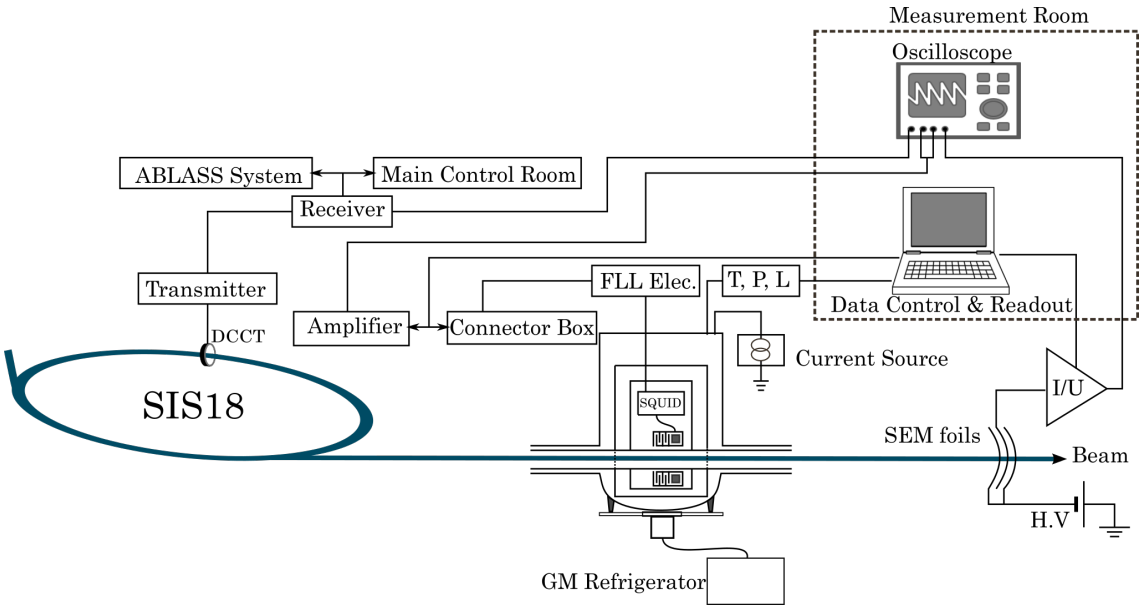

Figure 4.9: Simplified scheme of the beam current measurement by CCC, SEM and DCCT.

In addition to the intensity measurements using CCC and SEM, The intensity of the beam in the synchrotron was monitored with a DC Current Transformer (DCCT). Output of the DCCT

[1] a collection of software packages used for calculating energy loss of ions in matter and related transport calculations [69]

is send to the electronics room where the data is stored into the ABLASS[2]. This signal is read out at the main control room[3]. To monitor the extraction cycle of the beam, a parallel connection from the receiver of the DCCT was read out to the CCC at measurement room and was compared to the CCC and SEM signals as shown in the schematic in figure 4.9.

4.3 Beam Measurements

The passage of a charged ion beam through various sections of the GSI accelerator chain can be briefly described as follows. The particle beam once produced from the ion source is pre-accelerated in a linac, injected into the synchrotron SIS18, during a short period with certain losses to achieve its final energy. These energetic beams are then either injected into into the storage ring, ESR or extracted out of the accelerator for experiments. A typical intensity plot during various phases of charged particle motion inside the synchrotron can be seen from the DCCT measurement given in figure 4.10.

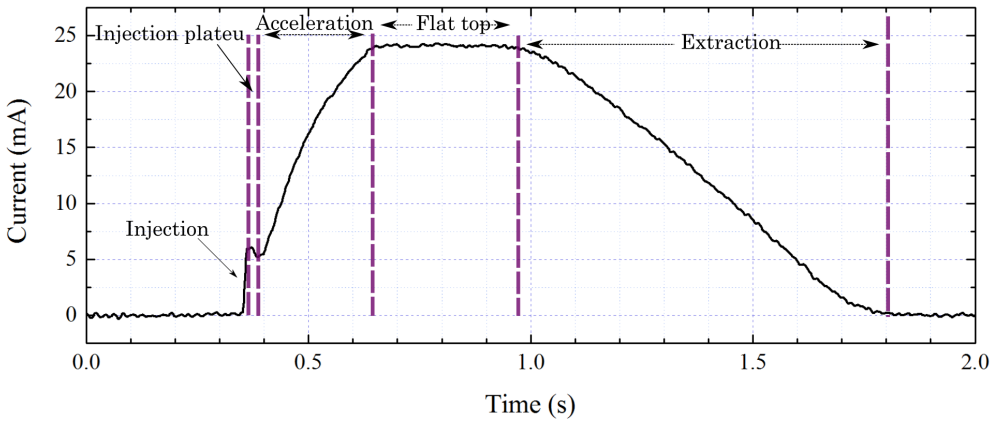

Figure 4.10: Acceleration scheme in a synchrotron between injection and extraction given by the intensity values measured with a DCCT.

4.3.1 Slow Extraction of Particles from a Synchrotron

Inside a synchrotron the beam trajectories are basically defined by the settings of its magnetic elements such as dipoles, quadrupoles and sextupoles. The accelerating fields are provided by one or more rf cavities. While dipole magnets are used for bending and quadrupole magnets for focusing/de-focusing the beam, sextupole magnets compensate the chromatic aberrations. These electromagnets which control the confinement of the beam in the synchrotron is collectively referred to the beam optics. To consider the collective behavior of the charged particles, ideal

[2]ABLASS (A Beam Loss measurement And Scaling System) is a centralized system which was established to count the particles and pulse modulated signals all over the SIS18 and its High Energy Beam Transport (HEBT) sections [70]

[3]Signals from all electrically controllable components of the accelerator such as diagnostic devices, magnets and vacuum pumps are read out and controlled at the control room

synchronous particle with a nominal momentum $|\vec{p_0}|$ can be defined. The trajectory of this particle is considered to be the reference orbit. Its revolution frequency of can be given by $f_0 = {}^{C}/_{|\vec{v_0}|}$, where C is the circumference of the synchrotron (in case of SIS18, $C = 216\,m$) and $|\vec{v_0}|$ is the relativistic velocity.

While circulating in the synchrotron, the charged particles undergo transverse oscillations - known as *betatron oscillations*. The number of betatron oscillations per one complete revolution inside the synchrotron are called *betatron tune*. The position of a random particle in the charged particle beam can be described by the phase space ellipse, the area of which is constant at any position or time in the synchrotron if the particle does not gain or dissipate energy by any non-conservative interactions [71]. In case of a particle undergoing betatron oscillations reaches the same point in the phase space after a certain number of revolutions, a resonance condition occurs. In this case, any imperfections on the force acting on the particle, such as magnet alignment errors or field errors, lead to resonant growth of the amplitude of betatron amplitude which leads to particle losses in the beam. Hence the resonance conditions of lower order have to be avoided.

The longitudinal motion of the particle inside the synchrotron can be described by two modes, i.e. as continuous *coasting beam* and as bunched beam. In the absence of any longitudinal forces the particles revolve inside the synchrotron with a constant angular velocity maintaining their original momentum. Depending on the relative energy ΔW, the particle moves forward or backward relative to the synchronous particle. However, in the presence of a sinusoidal voltage U_{rf} provided by an rf cavity[4], the beam is separated into one or several packages (*bunches*) and will be revolving in the synchrotron in the form of a bunched beam. An ideal particle finds the synchronous phase Ψ_0 of the electric field in each turn, the particles with an energy deviation oscillate around the synchronous particle and hence synchronous phase. However the particle beyond a certain momentum will not oscillate around the synchronous particle and instead float around the synchrotron as shown in figure 4.11. These particles are unstable and are lost during the acceleration process. The boundary which separates the stable and unstable particle energies in the W/ϕ diagram is called the *separatrix*. Analogue to the oscillations in a potential well, the particles of the bunch will undergo longitudinal oscillations around the ideal phase, which are called synchrotron oscillations. The frequency of this oscillations, called synchrotron frequency is given by,

$$f_s = f_{rev}\sqrt{|\frac{\eta \cdot Q \cdot U_{rf} \cdot h \cdot \cos\Psi_0}{2\pi\beta^2 E}|} \tag{4.7}$$

where, f_{rev} is the revolution frequency of the particle in the synchrotron, U_{rf} is the rf acceleration voltage, h is the harmonic number of the synchrotron, E is the total energy of the beam, η is the slippage factor given by $\frac{1}{\gamma_T^2} - \frac{1}{\gamma}$, γ is the Lorentz's factor and β, the velocity to speed of light factor. In the case of bunching by beam without acceleration, Ψ_0, the phase of the reference particle can be taken as zero.

For investigations on interactions of high energy beams with matter, the accelerated beam from the synchrotron is extracted to fixed target experiments. Fixed target experiments normally

[4](in SIS, two identical rf cavities are used to realize four rf buckets, hence harmonic number, $h = 4$ [72])

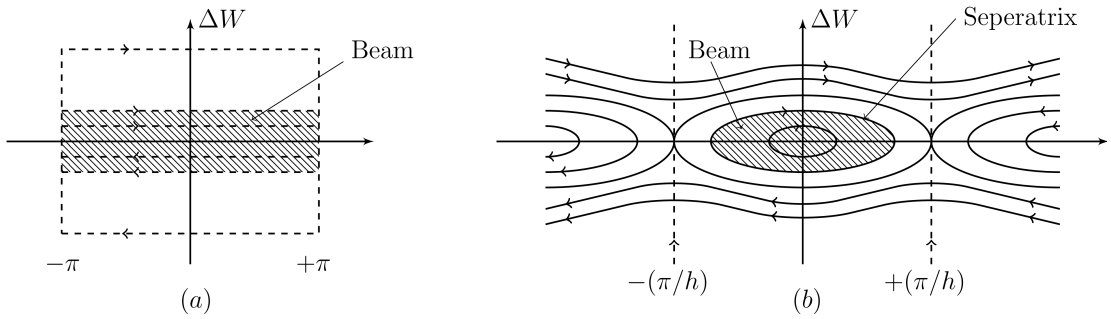

Figure 4.11: Longitudinal Phase space for coasting (a) and bunched beams (b). Figure courtesy, Ref. [71]

require slowly extracted ion 'spills' from the synchrotron. An optimum slow extracted beam should have a smooth, uniform spill of hundreds of milliseconds to several seconds length. An example where the slow extraction with high spill homogeneity required is for the hadron therapy with its precisely controlled "pencil" beams and uniform dose deposition [73]. In most cases, the slow extraction is realized by controlled excitation of the non-linear resonance of betatron oscillations [74] inside the synchrotron, and are hence called resonant extraction.

A standard scheme of the resonant extraction mechanism can be described as follows. Using the quadrupole and sextupole magnets, a resonance condition for the betatron oscillations is fulfilled at a specific orbit, termed as resonance orbit. As the beam orbit is shifted close to the resonance orbit, the amplitude of the betatron oscillations increase rapidly until the particles with the largest amplitude start to fall into the septum of the kicker magnet and get kicked out of the orbit, which means they are extracted from the ring. Further details on various schemes for resonant extraction can be found in [75]. For the measurements discussed in the following sections, slow extraction up to several seconds is realized by the third order integer extraction from SIS18. This scheme is realized by varying the betatron tune to approach the third order resonance using a fast quadrupole magnet.

4.3.2 Beam Parameters

For the intensity measurement using CCC, slowly extracted Ni^{26+} ions at an energy of 600 $^{MeV}/_{u}$ were extracted from the synchrotron to the beamline section, HTP. The extraction time was varied from 64 ms up to 5 s. To measure the intensity of extracted spills, the number of particles was varied from 2.8×10^8 to the maximum available beam intensity of 5.6×10^9 particles per spill. By setting the number of particles and extraction time, a set of beam signals with average beam currents in the range of 2 nA to 105 nA were measured. Details of the complete beam parameters with respect to the synchrotron settings used for the beam measurements are given in table 4.1.

Parameter	Symbol	Value
Ion Species		Ni
Charge state	Z	26+
Atomic Number	A	58
Energy	E	600 $^{\mathrm{MeV}}/_{\mathrm{u}}$
Number of Particles	N	2.8×10^8 to $5.6 \times 10^9\, pps$
Extraction Time	τ_E	$64\, ms$ to 5 s
Bunching voltage	V_{rf}	$2\, kV$, $4\, kV$
Circumference of Synchrotron	C	$216\, m$
Revolution frequency	f_{rev}	$1.098\, MHz$
Slippage factor	η	0.338
Harmonic number	h	4
Ratio of velocity to speed of light	β	0.79

Table 4.1: Beam parameters and other relevant parameters used for the measurements

4.3.3 Measurement of Beam Intensity

A typical beam signal measured by all three devices (DCCT, CCC and SEM) is shown in figure 4.12. With fast detection and high rate data acquisition, CCC gives an excellent and reliable spill structure measurement.

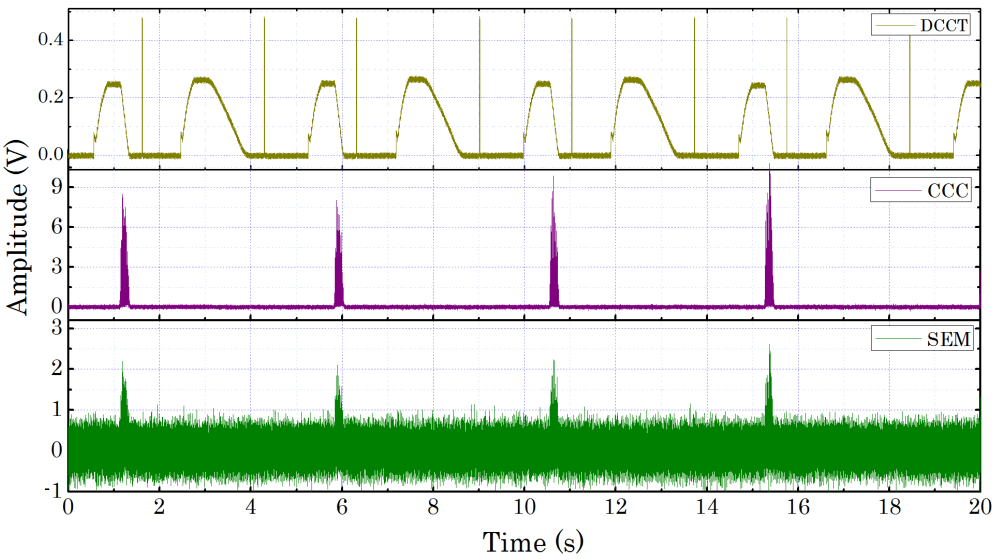

Figure 4.12: A typical intensity measurement of a coasting beam signal of 1.6×10^9 particles of Ni^{26+} extracted over 250 ms.

The beam measurement campaign was run in parallel with the HADES experiment [76] so that once in every two cycles, the beam was extracted to the HTP section as it can be seen from the DCCT signal which shows the intensity of the beam inside the synchrotron. These beam

signals are measured simultaneously by the CCC and SEM. From noise floor of the signal shown in figure 4.12, the current resolution was estimated to $2.3\,nA$ rms with a signal to noise ratio of 2. Figure 4.16 shows a typical time structure of a spill produced by the coasting beam containing about 1.3×10^9 particles extracted over $2\,s$. This produces an average current (over the total extraction time) of $5.34\,nA$ as measured by the CCC. The beam signals were measured with a time bin of $20\,\mu s$.

4.3.4 Comparison with SEM Measurements

To compare the spill structure measured by the CCC to a standard intensity measurement technique, the Secondary Electron Monitor is chosen as it can measure the intensity from several nano amperes to several hundred nano amperes depending on the gain settings at the trans-impedance amplifier (depicted in figure 1.3). The bandwidth of the SEM output is much higher than the CCC system in which the $10\,kHz$ anti-aliasing filter limit the bandwidth at the output. Hence to compare with the CCC output, the SEM signals are filtered with a low pass filter of similar characteristics to that of the anti-alias filter (given in section 3.4.2). With the bandwidth of $10\,kHz$, the noise floor of the SEM output was calculated to $13.57\,nA$. The spill structures measured by both SEM and CCC are compared in figure 4.13. As it is clear from the figure, the time structures of both CCC and SEM shows excellent match.

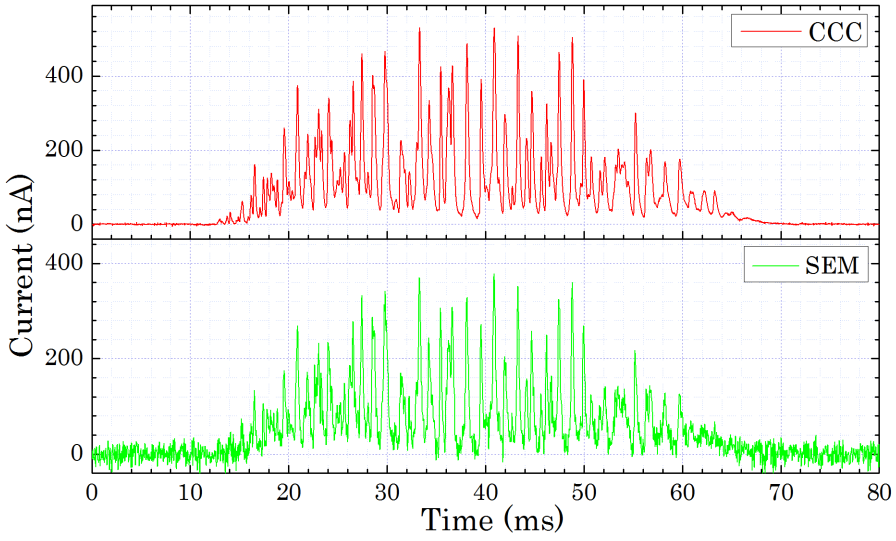

Figure 4.13: Comparison of the spill structures measured by both CCC and SEM. The spill structure is produced by 1.6×10^9 particles of Ni^{26+} ions extracted over $64\,ms$. For the comparison with CCC signal, the SEM signal is filtered with a low pass filter of cut-off frequency $10\,kHz$.

The frequency spectra of the signal measured by both CCC and SEM are given in figure 4.14. The amplitude of the frequency spectrum of SEM is normalized to that of the CCC spectrum for comparison. The frequency spectrum shows excellent match for the peaks corresponding to different noise signals. In addition to the major harmonics of $50\,Hz$, SEM detects additional

peaks at 791 Hz, 1078 Hz and their harmonics which were not present in the CCC measurements. These vibrations are presumably caused by the oscillations of SEM foils due to the operation of turbo molecular pumps installed very close to the SEM installation point, which are running at a frequency, 800 Hz and 1000 Hz .

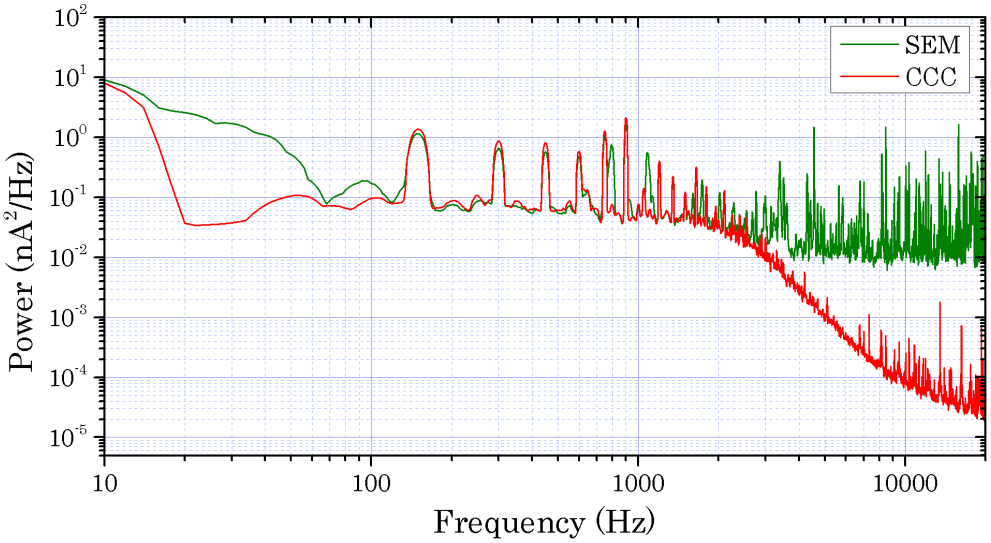

Figure 4.14: Comparison of the frequency spectra of CCC and SEM averaged over 9 spills. To reduce the noise floor, both the frequency spectra are smoothed using adjacent average method with a window of 15 points.

With a set of 65 different beam spill structures measured by both CCC and SEM, the intensity values of both measurement is compared as plotted in figure 4.15. With a linear error within 0.7%, both measurements shows excellent linearity over the complete range of the measurements. However the intensity values of the SEM shows a constant deviation of 18 % (lower) from the intensity measurements using CCC. After several investigations on the possible sources of errors such as calibration of both devices and various electronic settings, a specific reason for this deviation could not be given. Possible candidate for this error can be any imperfections on the SEM foils such as aging or presence of moisture which can influence the secondary electron emission rate. Detailed investigations are proposed to investigate the origin of this deviation.

4.3.5 Bunched Beams for Improved Time Structure

Ideally the spills are expected to be homogeneously filled with particles like a pulsed dc signal. However in realistic case, as seen in figure 4.16, the spill structure contains spikes with maximum amplitude reaching up to 267.6 nA, whereas the average beam intensity is 13.3 nA. For the detectors used in atomic physics experiments, these ripples cause an overload during the spikes followed by a lack of reaction rate. The spills recorded with a time bin of 20 μs and the ripples contain a steeper rise compared to the falling edge as predicted by L. Badano *et.al.* [75].

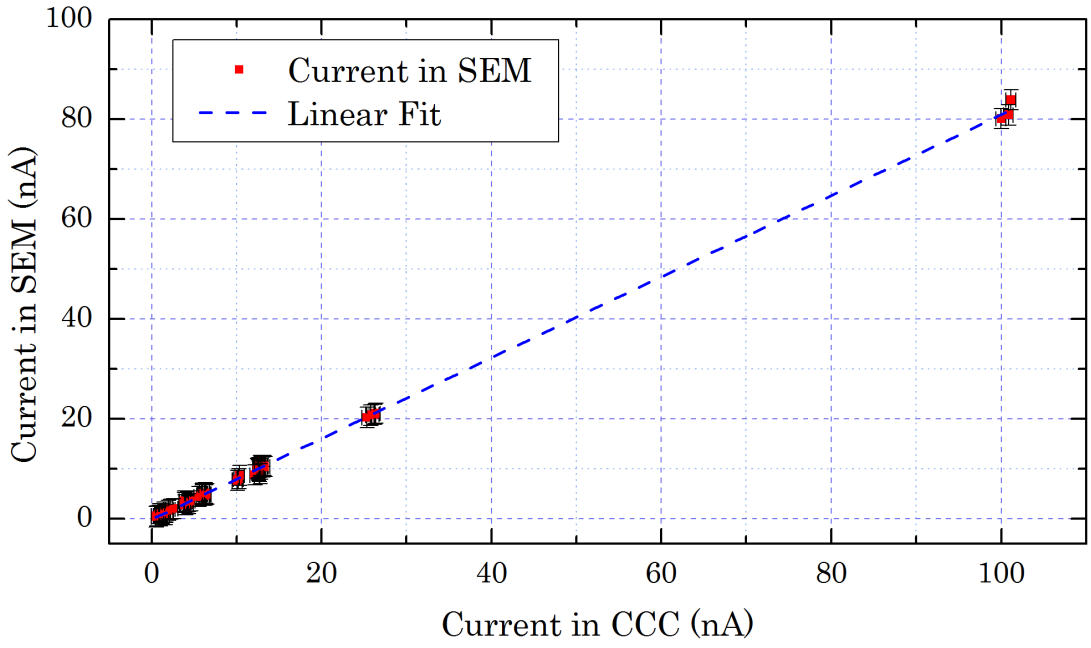

Figure 4.15: Comparison of the beam intensity measurements by CCC and SEM

These ripples originate from the fluctuations associated with the power converters of the magnets which cause the actual current to undergo deviation from the set DC current. This leads to fluctuations in the magnetic rigidity of the dipole magnets [77]. Moreover, to achieve the slow extraction in the order of seconds, the tune has to be varied slowly (relative tune change of $10^{-3}\,s^{-1}$) using quadrupole magnets which are easily disturbed by the ripple driven variation in the magnetic field [78]. While the tune of the resonance is an absolute number, the tune of the beam has the perpetual jitters. The resultant sharp movement of the tune shift causes a burst of particle entering the resonance and hence appear as a narrow peak in the extracted beam followed by flat plateau as seen in 4.16.

With sufficiently high error in the tune shift, the spikes in the spill structure causes the "over modulation" *i.e.* instantaneous current values are discontinuous with no particles over small time intervals in the spill. For any consideration of event rates in experiments, these fluctuations have to be taken into account. P. Forck *et.al.* [78] have shown that by bunching the beam the quality of the extracted beam can be improved.

Figure 4.17 shows the spill structure of a beam which was bunched inside the synchrotron prior to the extraction. By bunching the beam with an rf voltage, empty buckets are created at the resonance frequency which causes obstruction in phase space and hence the beam particles start to channel around these buckets. By this technique, the particle velocity can be increased as the particle crosses into the resonance region, thereby making the extraction less sensitive to ripples. In figure 4.17, the spill structure of a bunched beam of 9.7×10^8 particles extracted over

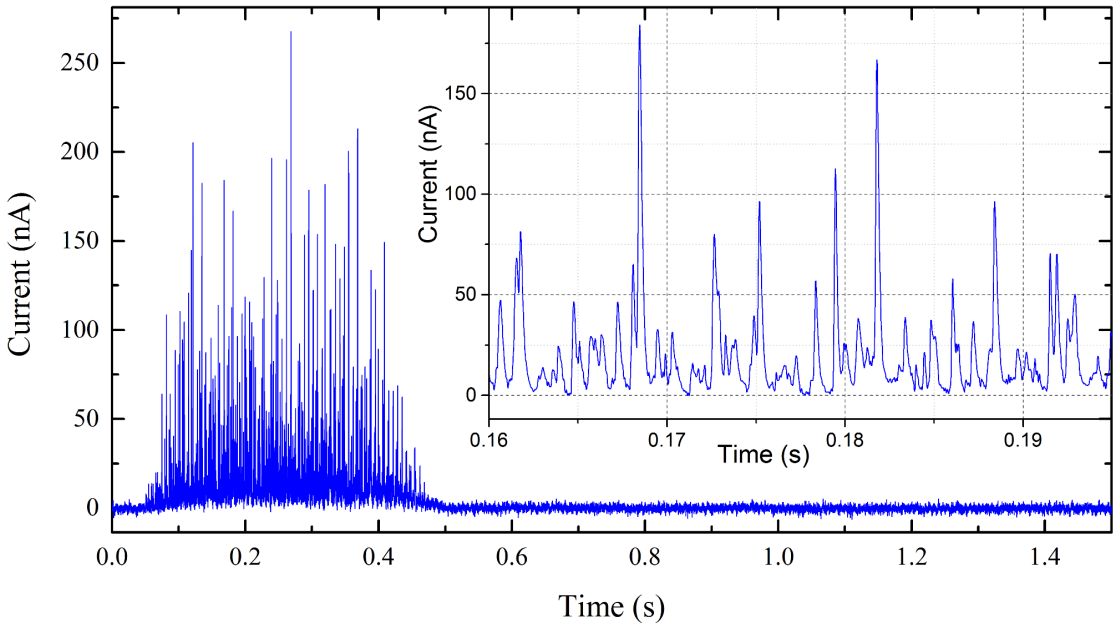

Figure 4.16: Spill structure formed by 1.3×10^9 particles of Ni^{26+} slowly extracted over $500\,ms$. The zoomed in view of the time structure is shown in the inset.

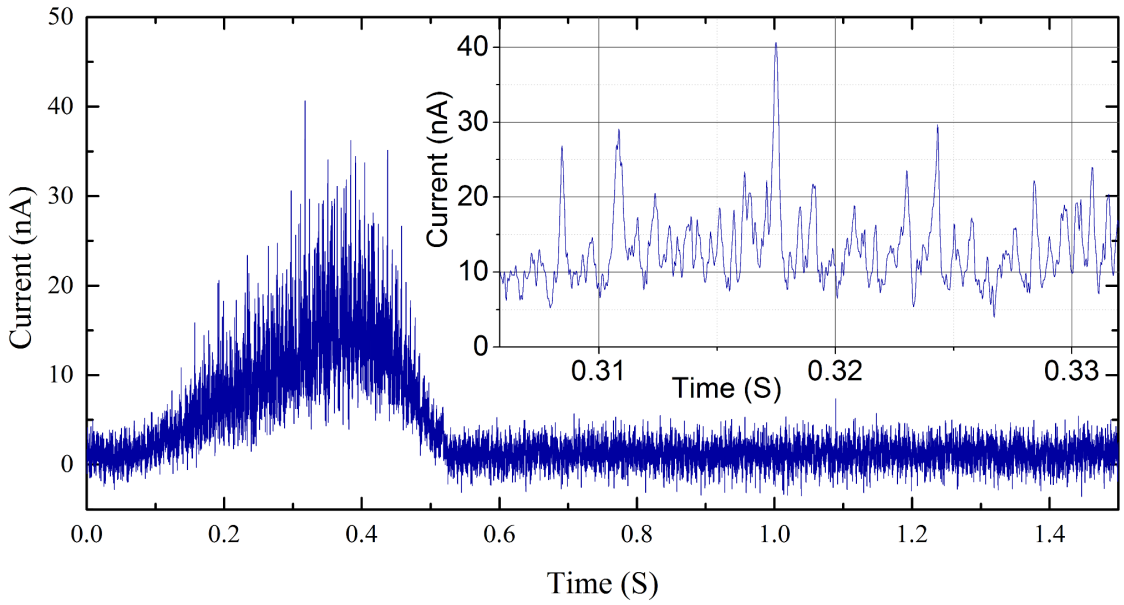

Figure 4.17: Spill structure produced by a bunched beam with 9.7×10^8 particles extracted over $500\,ms$. The beam is bunched with a bunching voltage of $2\,kV$. Zoomed in view of the same spill is shown in the inset.

$500\,ms$ to give an average current of $8.4\,nA$ is shown. The particles are bunched with an rf voltage of $2\,kV$, which is a factor of $1/7$ of the voltage used for acceleration. As it can be seen in figure, the bunched beam spill structure avoid the over modulation completely. In addition, the spikes in the spill structure are well suppressed as the maximum amplitude is $40.63\,nA$ ($\frac{I_{max}}{I_{avg}} = 4.85$,

whereas this factor for the coasting beam is measured to 20.12). With increasing rf-voltage, it was found that the spill structure was further improved. This was expected due to the stronger focusing of the momentum close to the resonance line.

The improvement of the spill quality by this method is dependent on their betatron amplitudes. It also depends on the frequency and amplitude of the ripples, this technique becomes less effective in the higher frequency ranges. Another characteristics of this method is that the spill shows a strong modulation at the harmonics of the synchrotron frequency as shown in figure 4.18.

4.3.6 Frequency Spectrum of the Spill

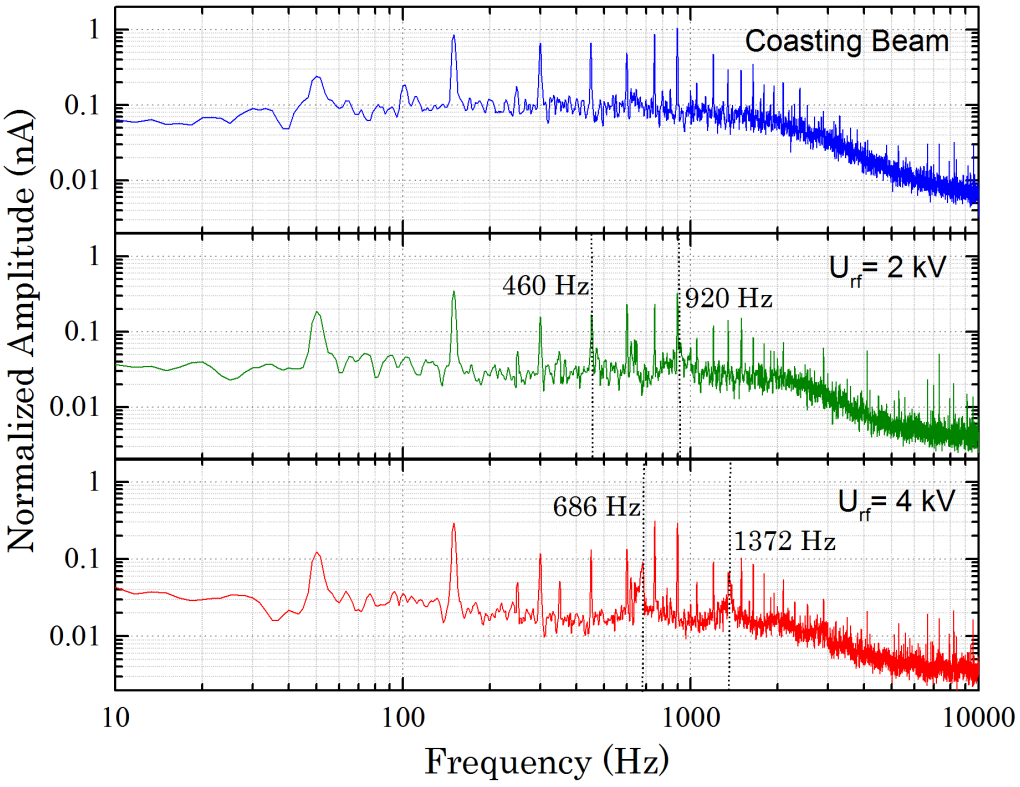

Figure 4.18: FFT of the signals with bunching and without bunching. The peaks in the bunched beam frequency spectra corresponding to the synchrotron frequency are highlighted in black.

Figure 4.18 shows the Fourier transformation of the spill of coasting beam and bunched beam. The frequency spectrum of the spills shows a number of characteristic peaks corresponding to the $50\,Hz$ more prominently, the harmonics of $150\,Hz$. These strong spikes are visible in both cases of bunched and unbunched beam spectra over a frequency range over $2\,kHz$. Nearly all other peaks which were found in the intrinsic frequency spectra of the system are suppressed by the electrical network frequency and its harmonics, however a broad peak in the frequency spectra of the beams can be found at $620\,Hz$.

In case of the frequency spectrum of bunched beams, in addition to the peaks corresponding to the noise components (as in case of coasting beam), the synchrotron frequencies and its harmonics are also present. Following equation 4.7, the synchrotron frequency of the particle beam in the SIS18 for an rf voltage $2\,kV$ and $4\,kV$ can be calculated as $494\,Hz$ and $698\,Hz$ respectively. The peaks corresponding to these frequencies and their harmonics can be found in the respective bunched beam's frequency spectra given in figure 4.18. In case of the beam with $2\,kV$ bunching voltage, the peaks in the frequency spectrum corresponds to the harmonics of $460\,Hz$ which agrees within 6% of its analytical value. In case of the beam bunched with $4\,kV$, the frequency spectrum shows peaks corresponding to $686\,Hz$ and its harmonics which are within 1.5% of the calculated value. These values shows good correspondence between the measured and calculated synchrotron frequencies considering the numerical simplifications taken for the calculations and experimental uncertainties.

The measurements show the reliability of the CCC system and its high data acquisition capability for investigations on the extracted beam signals, which can only be achieved by a non-integrating system which offers good time resolution for the intensity measurement.

Chapter 5

Influence of Experimental Environment on CCC System

It was demonstrated that the CCC can - due to its high magnetic field sensitivity - detect beam currents in the range of several nA. Naturally this sensitivity, as well as the complex composition of various components, makes the systems sensitive for different kinds of noise and environmental factors. In this chapter, detailed analysis of operation of the CCC in the presence of temperature and pressure fluctuations and a number of other ambient noise influences are presented.

The performance of the superconducting sensor unit of the CCC system cooled down under residual magnetic field (typical Field Cooled Case of a superconductor) are always found to be strongly influenced by smallest changes in environmental electromagnetic noise. In the first section of this chapter, a quantitative analysis of the noise figure of the CCC system operating in a typical accelerator beam line is presented. Major influences on the preparation and characterization of the CCC system in the presence of ambient noise fields are also discussed in this section.

While the dc SQUIDs are known to be sensitive to temperature variation in the milli-kelvin range, the influence of temperature on the intensity measurement depends largely on the nature of the pick-up unit and the SQUID electronics. The biggest influence of which - found during the beam measurement campaign - was that the CCC signal is extremely sensitive to pressure and temperature variations inside the liquid helium bath cryostat. Detailed analysis were performed to characterize the temperature/pressure dependence on the output signal in various working conditions of the system. In the second section of this chapter, the measurement of the temperature dependence on the CCC output is presented and several possible reasons for this effect are discussed. In the third section, some prevalent impacts of the temperature/pressure instabilities on typical operation of the CCC system and some useful measures to overcome these limitations are discussed.

With a wide sensitivity range that can be chosen in the FLL mode of operation, CCC can cover the typical intensity ranges foreseen at the future installation locations. However the output range is often limited by the excess noise environments which influence the linear flux range and noise width of the flux-voltage characteristics. In the fourth section, the operational range of the CCC system is discussed. The dynamic range of the system at various feedback resistor values

are discussed and the chapter is concluded with a description on the slew rate and flux jump limitations on the output.

5.1 Noise Characteristics

5.1.1 Flux Noise

Any Characterization of the optimized working conditions of the CCC system is found to be limited by several low frequency noise sources. This non-periodic noise causes random influences in the system performance over time. Hence it is useful to evaluate the performance of the system at a different times and compare the performances. In general, the variations in flux noise, transfer function and biasing conditions are indications to what extend the SQUID is affected by external noise. Successive reduction of these noise sources leads to step by step improvements in the operating conditions and hence performance of the system.

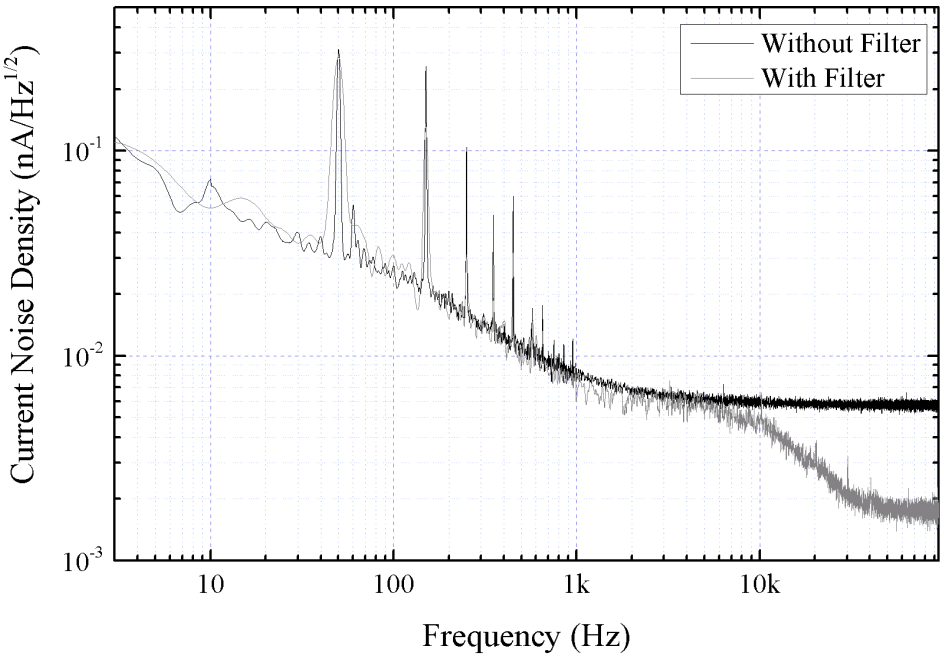

Figure 5.1: Noise spectrum measured with the CCC installed in the beam line. Grey: With anti aliasing filter, black: without this filter.

The low frequency noise mostly has $1/f$ characteristics. It is dominated by motion of trapped flux vortices in the superconducting loop and fluctuations in the critical current of the Josephson junctions. Figure 5.1 shows the noise spectrum recorded during the beam time with anti-aliasing filter ($10\,kHz$) and during offline measurements at the beam line at a later point with filter deactivated. Compared to the total flux noise level of $80\,\mu\Phi_0/\sqrt{\text{Hz}}$ during the beam measurements, a total flux noise with a slightly increased value of $90\,\mu\Phi_0/\sqrt{\text{Hz}}$ was recorded at $1\,kHz$. The white noise level of $60\,\mu\Phi_0/\sqrt{\text{Hz}}$ corresponds to a current noise density of $6\,\text{pA}/\sqrt{\text{Hz}}$. It was also found that the transfer function V_Φ in the later measurements were lowered to $9.6\,\mu\text{A}/\Phi_0$ which was measured to $10.6\,\mu\text{A}/\Phi_0$ during the beam measurements. As pointed in the previous chapters,

for the highest sensitivity of the sensor system, the SQUID biasing is optimized for maximum transfer function. However the excess noise caused by the external interferences can suppress the transfer function as the values indicate.

5.1.2 Ambient Field Influence on $V - \Phi$ Characteristics

Fluctuations in the critical current which suppress the transfer coefficient of the SQUID can also influence the symmetry of the $V - \Phi$ characteristics significantly. Figure 5.2 shows the formation of the $V - \Phi$ characteristics for a number of bias current values. As the bias current is increased above the critical current, the modulation increases to a maximum modulation depth and decreases on further increase in bias current.

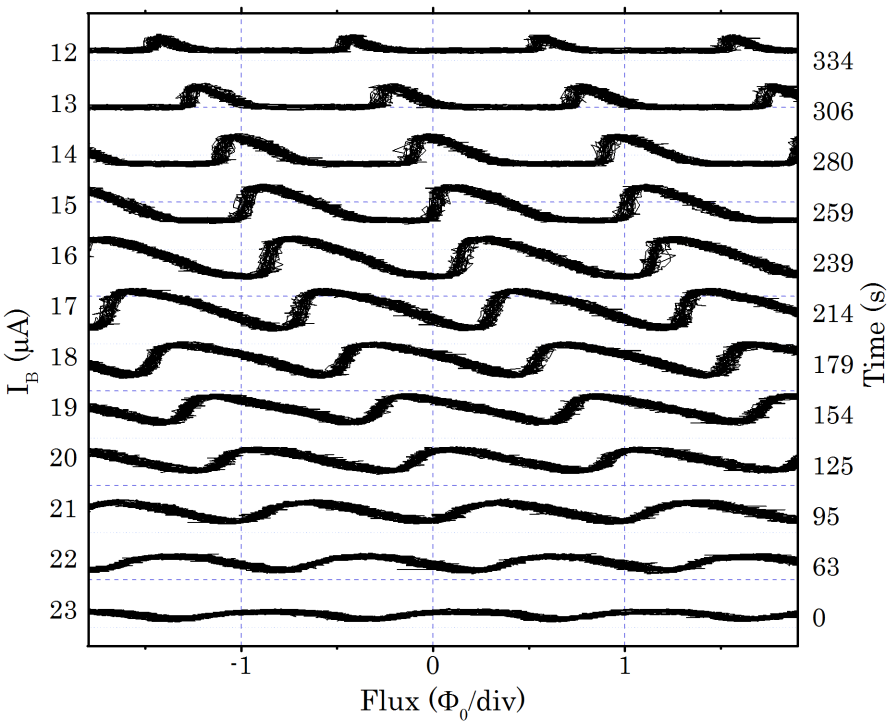

Figure 5.2: $V - \Phi$ characteristics of the dc SQUID with distorted sinusoidal oscillations at various bias currents in the presence of drift in the bias flux. The measurements were carried out during first cool down, where the drift was found to be maximum.

For the optimum performance the SQUID is biased at a flux $(n \pm 1/4)\Phi_0$, where n is an integer depending on the applied flux. In case of identical Josephson junctions, the variation of critical current within one flux quantum through the SQUID loop is generally given by the relation,

$$\Delta I_C = \frac{\Phi_0}{2 \cdot \gamma \cdot L} \tag{5.1}$$

where γ is the damping parameter for the shunted dc SQUID. From this equation, given by the temperature dependence of the inductance L, one of the most influential factors in the critical current are thermal instabilities. Critical current fluctuations arise from the trapping and release

of electrons from the defect sites in the tunneling barrier of the Josephson junctions [30] causing a large noise width in the $V - \Phi$ characteristics. The thermal fluctuations increase the critical current noise and can also produce asymmetry in the shunt resistors which can cause an effect similar to that of an additional positive feedback [79]. As a result, the sinusoidal behavior is strongly distorted, limiting the linear flux range in the flux-voltage characteristics. In simplified terms, asymmetry of the shunt resistors can act as a virtual feedback resistor with the SQUID inductance acting as the feedback coil [80]. A Degradation of the $V - \Phi$ characteristic can also be caused by the thermo - electric voltages (Seebeck effect [81]) originating from temperature gradients at junctions of different metals.

In addition to the distortion and noise width, the $V - \Phi$ characteristic curve is also found to have a strong drift. As it is shown in the figure 5.2, the flux voltage characteristics undergoes continuous drifts (in this case in the direction opposite to the flux applied to the SQUID by the feedback coil) at a rate of $8.06\,^{m\Phi_0}/_{s}$. The drift and the distortion of the $V - \Phi$ characteristic curve result in instability of the working point. Similarly the working point set at a point far from the center point of the increasing or decreasing slope may results in any additional external flux exceeding the linear flux range Φ_{lin} and hence limiting the dynamic range of the system.

5.1.3 Offset Drift in the CCC Measurements

With the sensor unit operating in the FLL mode, the output voltage of the CCC was found to have a significant drift similar to the drift found in the $V - \Phi$ characteristics. The magnitude of this drift was found to vary largely with time. Most important factor influencing the drift - found from operating experience - was the thermal fluctuations inside the liquid helium cryostat. During a number of cooling down cycles, it was observed that the drift gets reduced over time as the liquid helium cryostat reaches better thermal equilibrium.

Figure 5.3 shows the typical zero signal output of the CCC showing the drift measured under various conditions. In the first case 5.3 (a), the drift is measured immediately after the CCC system was cooled down. It represents the highest drift which has been observed at our system. The drift rate was measured to $1.6\,^{\mathrm{nA}}/_{\mathrm{s}}$, which (considering the application of the system, where several nano-ampere current is to be measured) is extremely large.

In the second case, the drift was measured around three hours after filling the cryostat. Hence the system was in a more thermally stable condition. The drift rate in this case was measured to be $0.38\,^{nA}/_{s}$. After 7 hours of cooling, the drift was reduced to $0.047\,^{nA}/_{s}$, indicating gradual stabilization of the system. Most interestingly once the sensor unit of the system is warmed up to about $10\,K$ for a few minutes and cooled down again back to $4.2\,K$ in a few hours the drift rate (not shown in the figure) was found to have reduced further down to $6.2\,^{pA}/_{s}$ which is considerably smaller than the values measured after cool down only once.

A drift in the current offset was also reported in the earlier CCC measurements [16, 47, 48]. A. Peters *et.al.* could measure the drift over 100 hours and found to have exponential nature (see Ref. [47]) over this period. But, unfortunately this could not be reproduced in our measurements, mainly due to the lower liquid helium life time during one filling. However as shown in figure 5.3, the tendency of the drift was found to follow a similar exponential behavior and slow reduction

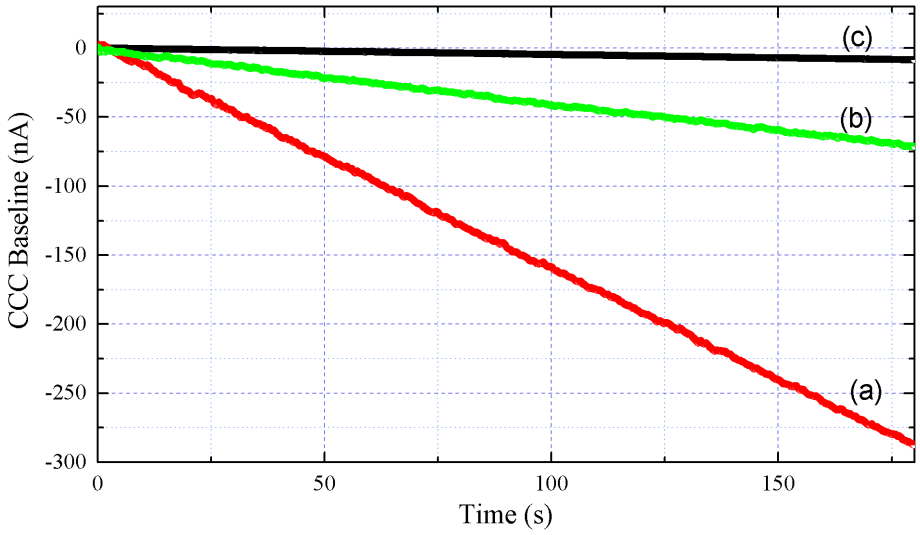

Figure 5.3: Drift measured in the CCC spectrum under different conditions over a period of 180 seconds. The fluctuations in the offset is caused by the temperature fluctuations inside the liquid helium cryostat.

in drift over time. Although the reason for the variations in the drift are not completely clear to us, general behavior indicate the Seebeck effect and possible thermal hopping of trapped flux within the superconducting elements.

Seebeck effect contributes to the formation of thermo-electric voltage when a slight temperature difference between two dissimilar electrical contacts are established at some point in the electronic scheme. The SQUID unit is connected to the FLL electronics, which is at room temperature, via a feed-through of about $1\,m$ in length. The thermo-electric voltage produced at the preamplifier can result in persistent drift in the CCC output [82]. Hence with the temperature gradient along the electronic unit, any imperfections in the electrical contact can produce thermo - electric voltages resulting in the drift at the CCC output.

When the CCC system is cooled down under the presence of residual magnetic field (strongest contribution are from Earth's magnetic field components, $B_{\parallel} \approx 50\,\mu T$ and $B_{\perp} \approx 40\,\mu T$ [83], with the magnets close to the CCC system switched off), magnetic flux can be trapped around the superconducting elements. Expulsion of the magnetic flux by Meissner effect will not reduce the magnitude of the trapped fluxes but can only be removed by heating the superconducting elements above their critical current. Flux trapping inside flux transformer, feedback- and flux modulation coil (which is included in the dc SQUID microchip, but not a part of the SQUID circuit in case of GSI - CCC system) could be avoided by heating the components with the help of built-in heater. However in case of the pickup unit of CCC, the flux trapping can only be avoided by warming up and re-cooling the cryostat.

Trapped fluxes coupled to a superconducting loop can produce a screening current without decay and can be easily coupled into the SQUID circuit. This screening current can produce an input noise current resulting in a temperature dependent offset in the CCC output. In case of the pickup unit of CCC system, presence of trapped flux inside the magnetic shield geometry can be

described as follows. As the temperature is brought down towards $4.2\,K$, the Niobium pickup coil becomes superconducting at $9.3\,K$. With trapped magnetic flux coupled to the Niobium pickup coil, the magnetic shield geometry made of lead (Pb) turns superconducting at $7.2\,K$ which keeps the trapped flux inside the shield geometry. Although it is not clear how the magnetic field is aligned inside or how they respond to the temperature fluctuations inside the interior of the shield geometry, we assume that this can result in certain magnetization of the ring core (made of the amorphous metal, "Vitrovac 6025-F") which might contribute to the drift.

In addition to the flux trapped inside the superconducting magnetic shield geometry, flux can also be pinned to the flux vortices in the superconducting materials through impurities in the superconductors [84].

5.2 Offset Drift- Temperature/Pressure Dependence

Besides the excess flux noise and resulting drift, another important characteristic observed during the current measurement was that the CCC output signal was extremely sensitive to pressure fluctuations inside the liquid helium cryostat. As the temperature of the system is increased, the drift was found to follow the temperature/pressure variations instantly in a direction opposite to that of the steady state drift. The magnitude of this drift is substantial compared to the typical beam current to be measured. Hence precise estimation of the drift as a function of temperature and pressure inside the liquid helium cryostat is important for the accurate measurement using CCC.

5.2.1 Measurement Setup

To study the influence of temperature on the offset the pressure inside the liquid helium cryostat is adjusted, which introduced instantaneous variation in the temperature of the cryostat and hence the sensor components. The pressure is controlled via adjusting the exhaust helium boil-off pressure with the help of a valve. The heat capacitance of the helium is extremely low at $4.2\,K$, therefore a (adiabatic) pressure increase will lead to immediate temperature increase. The variation in the pressure inside the cryostat is monitored by a differential pressure sensor and a mechanical manometer both mounted on the top of the outer vacuum chamber of CCC. The temperature sensors connected at various locations of the CCC system (as shown in figure 3.1) are used to monitor the temperature variations caused by the pressure increase inside the cryostat.

The typical behavior of temperature at various points caused by pressure manipulation is shown in figure 5.4. Here the temperature sensor T_2 directly measures the temperature on the magnetic shield. Being in direct contact with liquid helium and nearest to the liquid surface, T_2 is obviously most sensitive to the temperature variations. Sensors T_1 and T_3 are fixed on the outer surface of the liquid helium cryostat and these sensors, along with pressure variations, are also influenced by external thermal load. The temperature sensor T_4 is omitted from the image as is independent on the temperature fluctuations on the cryostat (mounted on the surface of the radiation shield). The gradual increase in temperature over the time is caused by the successive pressure increase, which stabilizes back to equilibrium after several minutes.

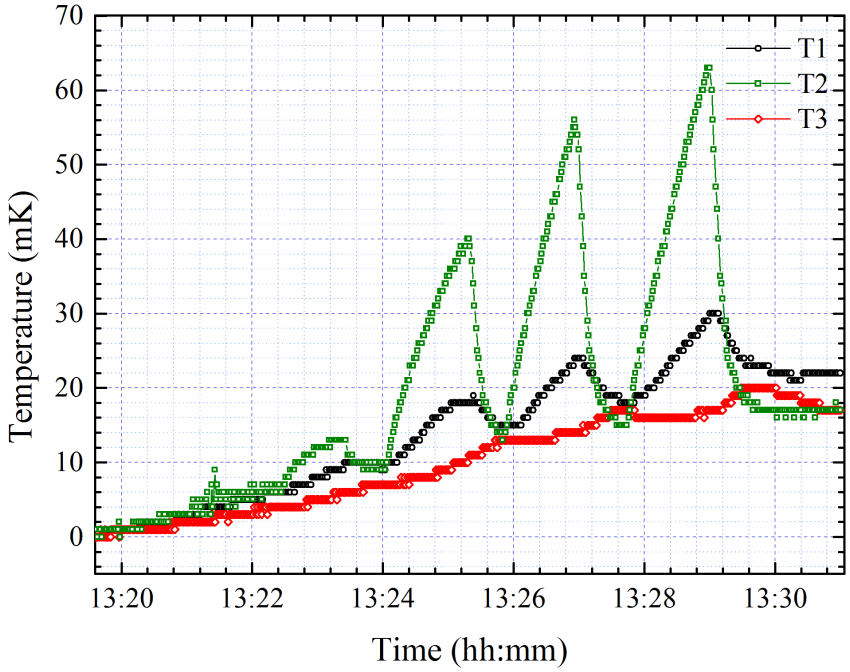

Figure 5.4: Typical temperature change caused by increasing and releasing of the pressure inside the liquid helium cryostat. The maximum pressure established in this cycle was 22.4 $mbar$. With the sensor T_2 measuring the temperature closest to the SQUID cartridge, T1 and T3 measuring the temperatures at the outer surface of the liquid helium cryostat as marked in figure 3.1.

5.2.2 Preparation of the Sensor Units

Pressure Sensor

The pressure inside the liquid helium cryostat is measured using two differential pressure sensors, one for measurement below the atmospheric pressure and one for measuring above atmospheric pressure. To minimize the noise, the pressure sensor is connected to the oscilloscope via a low pass filter with a cut-off frequency of 1 kHz. The sensitivity of the differential sensors connected to the oscilloscope was measured to 0.13 $mbar$ corresponding to a signal to noise ratio of 2. Since the signal amplitude of the pressure sensor is dependent on the input power given to the sensor amplifier, the sensor has to be calibrated prior to the measurement. Hence the pressure sensor is calibrated to the absolute pressure using a mechanical manometer (Absolutdrück... Company name to be noted) which has a precision of 5 $mbar$. Figure 5.5(a) shows the calibration measurements of the pressure sensor. For an input power of 10 V to the pressure sensor, the output voltage was calibrated to 4.86 $^{mV}/_{mbar}$.

Current Calibration

Since the CCC output is measured in terms of beam current (typically in nA), it is convenient to express the influence of temperature drift in the CCC output in terms of equivalent current. The output voltage is calibrated to equivalent current following the same procedure as described in

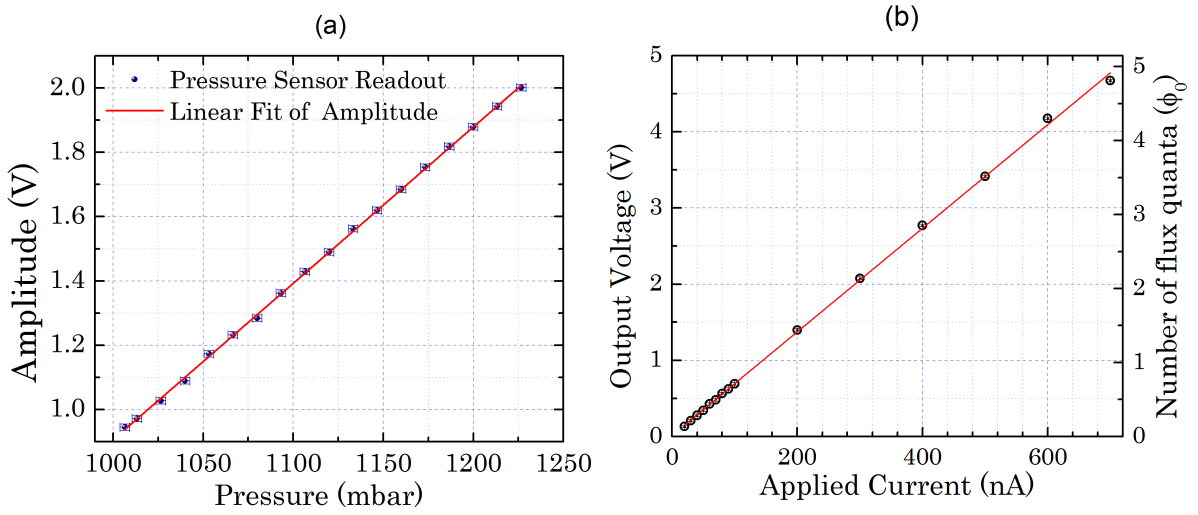

Figure 5.5: (a)Calibration curve of the pressure sensor to the absolute pressure measured by a mechanical manometer. (b) Current calibration plot of the CCC output voltage across the known applied current through the current calibration coil.

4.1.3. With all the possible working conditions are kept same compared to the beam measurement campaign, the working point of the CCC system was biased at the optimum working point. From a set of known current applied to the calibration winding, a current calibration factor with $R_F = 100\,k\Omega$ was calculated to $\kappa_V = 147.1\,^{\mathrm{nA}}/_{\mathrm{V}}$. With a reciprocal value of mutual inductance measured to $^{1}/_{\mathrm{M_F}} = 9.6\mu A$ and a $V_{period} = 0.24\,mV$, the current required to produce one flux quantum was calculated to $\kappa_\Phi = 153.2\,^{\mathrm{nA}}/_{\Phi}$. During the complete measurement session, the anti-alias filter with a cut-off frequency $10\,kHz$ was applied to reduce the rf interference at the output.

5.2.3 Results and Analysis

With the temperature and pressure sensors measuring the respective values inside the system, the drift in the CCC system was monitored while the exhaust pressure in the liquid helium cryostat was periodically varied. The instantaneous drift was recorded and a typical variation is shown in figure 5.6. The needle valve at the exhaust line was closed about 50 seconds so that an over-pressure of $15.3\,mbar$ developed inside the cryostat by the liquid helium boil-off. This rise of pressure created a temperature increase of $36\,mK$ at the temperature sensor, T_2 (installed at the top of superconducting magnetic shield). The valve is then released so that the pressure is reduced and hence also the temperature. With the SQUID cartridge installed about $5\,cm$ from the installation point of this sensor, the temperature of the SQUID system can be approximated to the value given by the sensor T_2. This pressure and temperature increases result in an instantaneous offset drift on the CCC output corresponding to an equivalent current of $1.107\,\mu A$ which is about $73\,\%$ of the full scale reading in the oscilloscope.

In the typical cycle of pressure increase and release, the CCC drift has a linear pressure dependency of $73.7\,^{nA}/_{mbar}$ which corresponds to a flux change of $0.62\,^{\Phi_0}/_{mbar}$ inside the SQUID

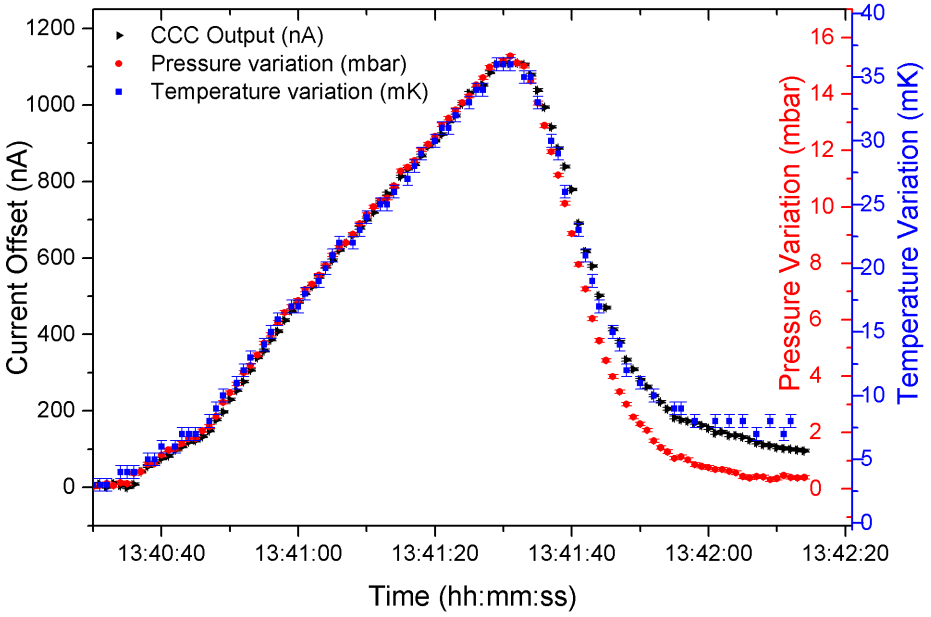

Figure 5.6: Relative drift measured in the CCC signal as the pressure inside the liquid helium cryostat is increased from the equilibrium pressure to $15.3\,mbar$. The temperature sensor shows the instantaneous temperature rise at the temperature sensor close to the SQUID cartridge.

loop. In terms of equivalent temperatures, the drift was estimated to $0.28\,{}^{\Phi_0}/_{mK}$ (which corresponds to a current dependence of $33.5\,{}^{nA}/_{mK}$). However this dependency was not consistent over a number of similar measurements.This value is surprisingly high compared to various investigations reported previously on bare SQUID sensors (for example [85]). In fact these figures shows the importance of temperature/pressure stability for especially for long term measurements.

5.2.4 Mechanisms Leading to Temperature Dependence in SQUID

It is well known that all SQUID based devices are strongly influenced by temperatures down to milli-kelvin range [84, 86]. In fact, based on its temperature dependence, dc SQUIDs are used for the thermometric applications, by utilizing the variation of its noise level with temperature [87, 88]. In addition to the contribution of higher noise levels, it was observed - as shown above - also on our system that the offset drift is highly sensitive to the working temperature. Temperature driven zero drifts were also observed in other typical high resolution magnetic field measurements as well(for eg. in geophysical applications, see [89]).

Apart from the possible sources of drift in the CCC output such as thermo-electric voltages and trapped flux formation, a number of other strongly correlated factors can contribute to the strong temperature/pressure dependence of the CCC output. Possible mechanisms which can contribute to temperature dependence in the sensor and pickup unit are as follows.

- **London Penetration Depth Fluctuations:** As the London penetration depth is temperature dependent, any fluctuations in the temperature can influence the characteristics the superconducting elements, noticeably on the microscopic geometries. The London pen-

etration depth of a superconducting material as a function of temperature can be given by the London formula,

$$\lambda_L = \frac{\lambda_L(0)}{\sqrt{1-(\frac{T}{T_C})^4}} \tag{5.2}$$

where $\lambda_L(0)$ is the London penetration depth at $T = 0\,K$. With Niobium having a critical temperature of $9.3\,K$ and $\lambda_L(0) = 39\,nm$, at $4.2\,K$, the variation in the London penetration depth can be calculated to $\frac{\partial \lambda_L}{\partial T} = 0.84\,\mathrm{nA/K}$. For a certain temperature change, the variation in the London penetration depth leads to corresponding variation in the effective area of the SQUID. However in case of the low-$T_C$dc SQUID with an inductance of nearly $300\,pH$, the change in the SQUID transfer function due to the temperature variation is reported to be in the order of $\frac{\partial \Phi}{\partial T} \approx 5\,\mathrm{m\Phi_0/K}$ [84].

- **Asymmetric Josephson Junctions:** In case of dc SQUIDs, in addition to the distortion in the flux-voltage characteristics, asymmetries in the critical currents can lead to temperature dependence of its output. If I_{C1} and I_{C2} are the critical currents of the two junctions which are considerably different, then the applied bias current I_0 will be asymmetrically divided between the weak links. With the energy gap of $\Delta(T)$ and the normal state resistance of the tunnel junction, R_N, the critical current I_C of these tunnel junctions can be given by the Ambegaokar-Baratoff [90] equation,

$$I_C = \frac{\pi}{2} \cdot \frac{\Delta(T)}{e.R_N} \cdot \tanh(\frac{\Delta(T)}{2k_BT}) \tag{5.3}$$

For a dc SQUID of inductance L, the temperature dependence of I_{C1} and I_{C2} will produce a change of flux through the SQUID as given by,

$$\Phi_{tot} = \frac{L \cdot I_{C1}}{2} - \frac{L \cdot I_{C2}}{2} = \frac{L}{2} \cdot \Delta I_C \tag{5.4}$$

where I_C is the critical current of the tunnel junction. As the temperature of the junctions is increased, the critical currents in the junctions are decreased which can also decrease ΔI_C roughly in the order of I_{C1}or I_{C2} (whichever is lower). The change in the flux coupling with the SQUID is expected to be in the order of $35\,\mathrm{m\Phi_0/K}$ [84].

- **Thermally activated motion of flux vortices:** With the trapped flux contributing to the current offset drift in CCC measurements as described before, sufficiently large thermal energy can result in the trapped flux vortices hopping to the adjacent pinning sites producing changes in the flux[84]. As the number of trapped vortices and their position is likely to vary with time, the effect is more likely to be random and not reproducible. In case of the pickup unit of CCC system, the geometrical dimensions are large compared to the sensor unit and hence a large amount of magnetic flux is likely to be trapped producing screening current proportional to the size of the geometry.

5.3 Measures for Stable CCC Operation

Due to the temperature instabilities and excess mechanical vibrations associated with the cryogen-free cooling solutions, for the practical operation of CCC system, liquid helium bath cryostat is

the reliable cryogenic solution. For the test measurement of the GSI - CCC system, the liquid helium recycling system included storage of the boil-off helium gas in a helium gas bag which is installed about $70\,m$ from the CCC, connected by a recovery line. This helium gas is further purified, compressed and stored for further liquefaction.

During the helium compressor was running, it was found to cause slight pressure variations in the cryostat. This pressure variations were found to create proportional oscillations in the CCC signal synchronous to the pressure reading as shown in figure 5.7. The amplitude of the oscillation depends on the liquid helium level in the cryostat. With a liquid helium level of 56.5% of the total volume, the peak to peak amplitude of this oscillation was measured to $0.17\,mbar$. Resulting oscillations in the CCC signal was measured to $9.1\,nA$ peak to peak. As found in the frequency spectrum shown in figure 5.7(b), this periodic oscillation corresponds to $2.5\,Hz$. In addition to this modulation, it can be also seen that these fluctuations causes significant noise contribution in the lower range of the frequency spectrum. This indicates that for the future applications of the CCC, the pressure stability at the exhaust line of the system has to be improved for reliable measurements over long time scales.

As strong temperature dependent drifts were observed by a number of SQUID applications, several efforts are reported to reduce this dependence. To reduce the trapped flux vortices in the circuit, one possibility is to apply a high frequency magnetic field to "clean" the superconducting elements [84]. This technique follows application of a high frequency magnetic field (typically, $150\,MHz$) with high amplitude (of the order of $1000\,\Phi_0$) for several seconds, which is slowly reduced to zero. It was reported to have reduced the temperature dependence to about a factor of 5 [84].

In future CCC installations, where extraction times of several ten seconds are possible, temperature/pressure stability of the system is particularly important. To improve this stability on the cryostat side, the thermal load has to be further reduced. One possible improvement to improve the pressure stability is to reduce the thermal load (which leads to turbulence at the liquid helium surface due to boil-off) on to the liquid helium cryostat.

Being a highly delicate cryogenic system installed inside the accelerator vacuum environment, improvements on the thermal load on the CCC cryostat has practical limitations. However enhancing the pressure stability inside the liquid helium cryostat can be applied to have a better temperature stabiliis to have a pressure stabilizing system at the exhaust which can- based on the presented drift values- achieve a pressure stability within $1\,mbar$. However the temperature of cold helium gas has to be taken into account, at which the standard pressure stabilizing valves fail to operate.

The offset drifts can be compensated efficiently by means of a precise pressure measurement inside the liquid helium cryostat as presented in the previous section. As the pressure and hence the temperature are perfectly correlated with the CCC readout and the pressure dependency is known, by the synchronized readout of pressure variations one can compensate the drift from the CCC readout. However, this technique cannot be adapted as a long time solution since a persistent drift can cause resetting of the working point once the offset exceeds the maximum flux limit of the CCC feedback loop. Although one can reset the working point of the FLL loop, in the presence of drift, the new working point may have different slope compared to the initial

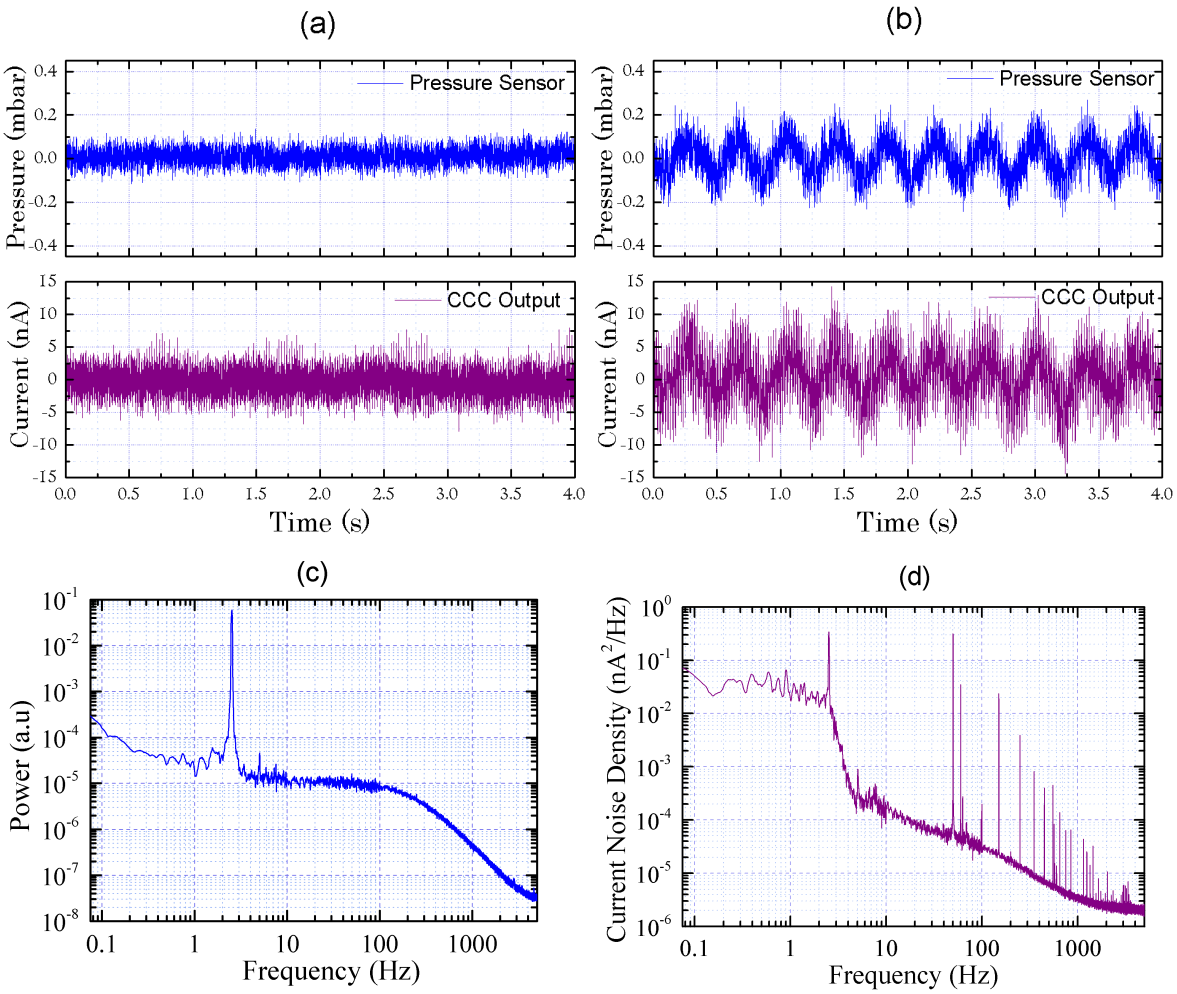

Figure 5.7: Plots showing the influence of the compressor unit of the helium gas recovery system connected to the liquid helium cryostat on the CCC output. Time domain signals of CCC and pressure sensor when the compressor is switched-off (a) and fluctuations observed when the compressor is switched-on. Frequency spectra of the pressure sensor output (c) and CCC output (d) indicating the influence of these fluctuations on the performance of CCC.

point. This leads to changes in the transfer coefficient (hence calibration factor) and dynamic range of the system.

5.4 Operating Ranges of CCC

5.4.1 Dynamic Range of CCC system

As mentioned before, with the FLL mode of operation, the SQUID system can measure a current which is equivalent to a tiny fraction of a fluxon to several hundreds of flux quanta. For the beam measurement described in the previous chapter, the current resolution was measured to $2.4\,nA_{rms}$ which is equivalent to $0.029\,\Phi_0$. In higher intensity range, the limit is typically determined by the maximum voltage of the integrator which is limited to $V_{max} \pm 10\,V$. Hence the maximum

flux that can be fed back through the feedback coil with the chosen feedback resistor R_F is given by,

$$\Phi_{max} = \frac{M_F \times V_{max}}{R_F + R_W} \tag{5.5}$$

where R_W is the additional resistance in the feedback loop given by the wire resistance and can be neglected ($R_W \ll R_F$). In the most sensitive range of the electronics with a feedback resistance of $100\,k\Omega$ and with a measured reciprocal value of mutual inductance (in the case of beam measurements) $^1/_{\mathrm{M_F}} = 10.67\,^{\mu\mathrm{A}}/_{\Phi_0}$, Φ_{max} can be given by,

$$\Phi_{max} = \frac{M_F \cdot V_{max}}{R_F} = \frac{\pm 10\,V}{10.67\,^{\mu\mathrm{A}}/_{\Phi_0} \times 100\,k\Omega}$$

$$= \pm 9.37\,\Phi_0$$

Hence in this range of feedback resistance, the CCC system is able to measure a maximum current of $\pm 651.5\,nA$. With the feedback resistor selectable from $0.7\,k\Omega$, the maximum flux that can be applied by the feedback loop up to $\pm 1338\,\Phi_0$ which gives a maximum measurable current corresponding to $\pm 93\,\mu A$. However in practical operation, the measurement range of the output is also influenced by the linear flux range (Φ_{lin}) in the $V - \Phi$ characteristics. The output remains linear if the feedback error flux ($\Phi_e = \Phi_{in} - \Phi_F$) is within the range $\pm^{\Phi\mathrm{lin}}/_2$ [91]. If the feedback error flux exceeds this limit, the output start to saturate. This limit the dynamic range of the system especially when the CCC system is operated in relatively large noise fields such as the case presented here. Figure 5.8 shows the saturation of the CCC output caused by the excess flux. The figure shows the CCC response to a known applied current via the current calibration loop with three different feedback resistance values.

To achieve very high dynamic ranges in FLL mode of operation two techniques can be used, "flux quanta counting" and "dynamic field compensation (DFC)". In the flux-quanta counting technique, the feedback range of the FLL electronics is set to $\pm 1\,\Phi_0$. When the input flux exceeds the feedback range, that is when the flux in the feedback loop exceeds $\pm 1\,\Phi_0$, the integrator is reset. This causes the feedback current and hence output drops abruptly to zero. As the net flux in the SQUID is quantized to integer multiples of flux quanta, the new working point is set at the next cycle of the $V - \Phi$ curve, which is indistinguishable in the FLL output. Hence after the reset, the output follows the input flux with a constant offset which corresponds to one Φ_0. By counting the number of reset, the input flux is reconstructed and hence the dynamic range is hence substantially increased.

The FLL electronics also include the option of dynamic field compensation method to improve the dynamic range. In this technique, a compensation flux $\Phi_C$is applied to the SQUID if the feedback range is reached. By this way, the SQUID is always operated in a low field range. This technique was not used in our measurements and the details of this technique can be found in Ref [92]. Without the application of flux quanta counting and dynamic field compensation, current values up to $50\,\mu A$ (but not limited to) were measured using the GSI-CCC system which corresponds to $720\,\Phi_0$ with a feedback resistance of $10\,k\Omega$.

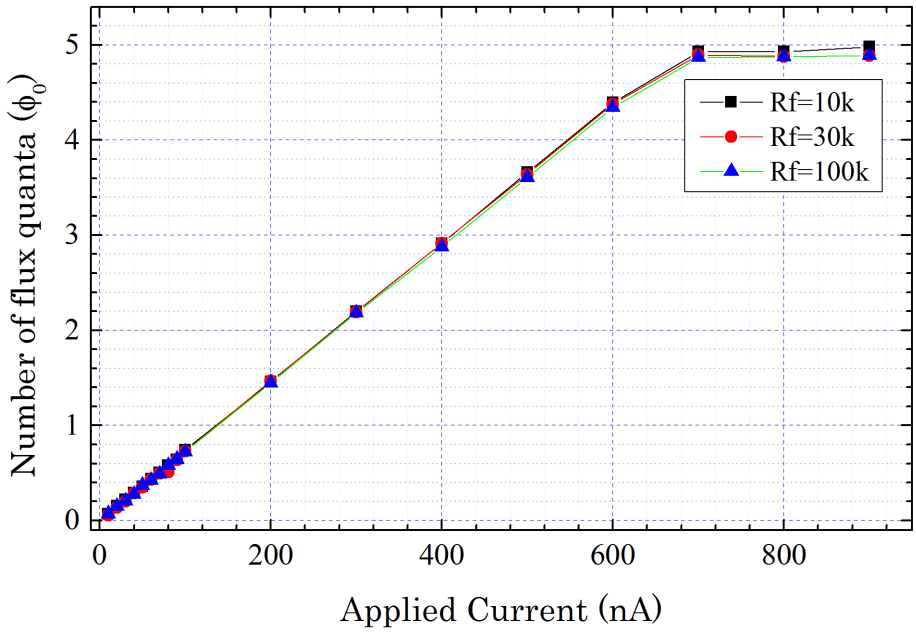

Figure 5.8: Plot showing the saturation of the CC output at higher amplitude in the presence of excessive noise. In this case shown here, the CCC output saturates above a flux $\Phi_0 = 5$.

5.4.2 Flux Jump and Slew Rate Limitations

Another measurement limit of the FLL electronics is given by the bandwidth of the measurement. The bandwidth limitation of the measurements mainly occurs due to the slew rate limitations of the FLL electronics (intrinsically dc SQUIDs fabricated by thin film technology have bandwidth in the range of several GHz) and flux jumps. The slew rate can be defined as the maximum rate at which the electronics can follow the change in the applied flux without loosing the lock. With a feedback flux Φ_F, the slew rate of the system is given by,

$$\dot{\Phi_F} = \mid \frac{\partial \Phi_F}{\partial t} \mid_{max}$$

As long as the applied flux is within the the linear flux range $\pm\Phi_{\text{lin}}/2$, the SQUID behaves as a linear element. However for the stable operation, the closed loop bandwidth of the electronics needs to be high enough for the feedback loop to respond to the fast changes in the input noise and bring the feedback error flux to zero. Otherwise, in the presence of noise amplitude that cannot be compensated by the feedback loop introduce a limit on the signal amplitude that can be measured.

Hence in the direct readout scheme, in terms of slew rate, it is not desirable to increase V_Φ to achieve high sensitivity since it can significantly reduce the linear flux range Φ_{lin}. Hence the choice of APF has to be chosen depending on the measurement requirement. Due to excessive noise interference, precise measurement of the slew rate of the CCC system could not be measured in our measurement campaign.

In addition to the slew rate limitations which causes output degradation, in case of the feedback error flux exceed $\Phi_0/2$, the working point of the system can jump one period (or more

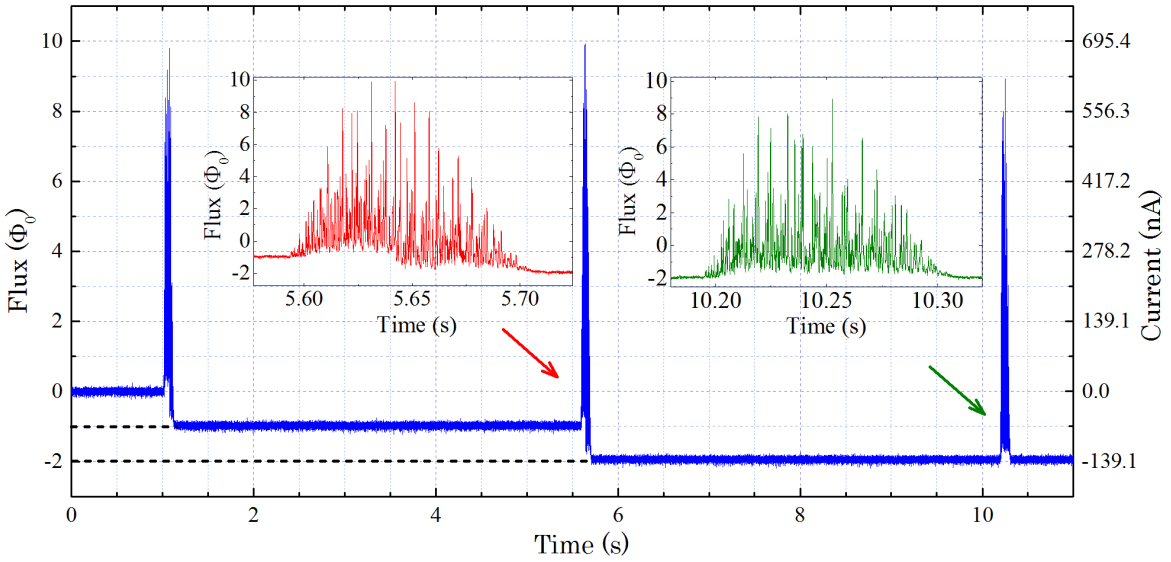

Figure 5.9: Flux jump observed in the beam measurement due to random excess noise in the feedback flux. The beam signal is produced by 5×10^8 particles of Ni^{26+} extracted over 125 ms to give an average current of $60.9\,nA$. Zoomed in view of individual spill structures are shown in inset.

depending on the amplitude of the feedback error flux) along the $V - \Phi$ characteristics known as flux jumps. A typical occurrence of flux jump observed while the beam measurements are shown in figure 5.9. When the system detects a sudden rise of the flux above $\Phi_0/2$, the system looses the lock temporarily and jumps to the next quantum level and regains the lock as shown in the figure. However after two cycles of jumps, the instantaneous changes in the feedback error flux is less than $\Phi_0/2$ and the output become stable without flux jumps.

Chapter 6

Advanced CCC Systems for FAIR

In the earlier chapters, technical details and performance of the GSI-CCC prototype have been presented showing its characteristic parameters under various working conditions. Combining these details with the working experience and boundary conditions at the beamline, a universal design of the CCC system is under development for a number of installation locations in the FAIR facility. Pilot studies of these installations will take place at Cryring[1] at ESR, which is currently under set up. In this chapter, an overview of the advanced CCC system is presented with scopes for further investigations.

In the first section of the chapter, the planned installation locations of the CCC system in the FAIR accelerator chain are discussed. Given by the nature of these locations, a number of boundary conditions are enforced on the CCC design concerning vacuum, cryogenic and structural aspects. The two general cases - beam transfer lines and storage rings - are considered separately as the interests for intensity measurement using CCC in these cases are different.

The results of the investigations presented in the previous chapters lead also to the scope of a number of further studies to improve the stability of the CCC system. In the second section, further investigations on the improved performance of the advanced CCC systems which partly go beyond the scope of this thesis are introduced. A brief description of these studies is presented indicating direction of further developments on the system.

In the third section, characterization of the superconducting magnetic shield for the upcoming CCC units using FEM simulations are presented. The calculated influence of various geometric parameters on the field attenuation is compared with an analytical model.

6.1 Installation Locations and Requirements

As mentioned in the first chapter, six units of CCC systems are planned to be installed in the FAIR facility in its first stage of realization. This includes four units in the High Energy Beam Transport sections and two units in storage rings namely, Cryring at ESR and Collector Ring (CR). While in HEBT sections, the most interesting parameters to be measured are the intensity and spill structure of a single pass beam, in storage rings, life times and reaction rates are of

[1] CRYRING at ESR is a heavy ion storage ring built by Manne Siegbahn Laboratory, Sweden, which is transferred to the GSI facility as an in-kind contribution to the FAIR facility.

major interest. Major requirement of the CCC design for FAIR is to develop a system which can -with minimum modification of geometric parameters- be installed at all planned locations. This generalized CCC is foreseen to have a compact cryostat with a length of less than $1\,m$ in beam direction. Since it was shown in earlier chapters, that temperature fluctuations significantly affect the current resolution of the CCC, a compact cryostat design (without increasing the thermal load) is challenging. In addition to the compact cryostat, the CCC system must be equipped for complete remote operation as the access to certain beamlines are restricted by the radiation safety measures.

In FAIR, due to the large number of instrumentation involved which is based on a wide range of different technologies, a common Front End Software Architecture (FESA) will be used at the lowest level of the control system [93]. For the standardization of the CCC system, data acquisition and control systems are required to be upgraded to be fit into the FESA framework.

6.1.1 High Energy Beam Transport

The High Energy Beam Transport (HEBT) is a complex system, which connects the synchrotron extraction lines, the experimental areas and the storage rings. Its total length at FAIR will be about $2350\,m$ [94]. CCC installations in the HEBT are planned at the extraction sections of the synchrotrons SIS18 and SIS100 in the first phase and at SIS300, which will be realized in the final phase. Additionally two CCC will be installed in front of the beam dumps, one of which is the part of SIS300. The CCCs will be used for precise measurement of high energy beams with intensities down to few nA, given by long extraction times (up to several tens of seconds). Apart from the precise measurement of beam intensity, the CCC will also be used for investigations on improved extraction efficiency and spill structure during slow extraction from the synchrotrons. The online measurement which provide the microstructure of the beam will help to identify individual machine parameters and their corrections. In addition to the investigations on the machine settings, CCC will also be used to calibrate other beam diagnostic components such as SEM, Ionization Chambers etc. The CCCs installed near the beam dumps will be used to analyze beam losses during transport to the dumps to ensure complete extinction of the beam.

In general the HEBT sections will be operating with a vacuum pressure of around $10^{-8}\,mbar$. Bake-out is not foreseen in the HEBT beamlines, however a pressure of $10^{-8}\,mbar$ was chosen because of the UHV requirements (down to $10^{-12}\,mbar$) in the synchrotrons and storage rings. In the FAIR CCC system, a separate isolation vacuum is necessary to avoid vacuum degradation by the large surface areas and trapped gas in the Multi Layer Insulation. Another boundary condition at these beamlines is that the beam tube diameter in the HEBT sections will be $160\,mm$ which require larger diameter of the warm-hole of the liquid helium cryostat compared to the GSI - CCC prototype. Close to the beam dumps CCC operation at high radiation levels must be possible over sufficiently long time periods.

6.1.2 Storage Rings

In general, accumulation of exotic beams (radioactive ions or anti-protons) and preparation of intense beams for internal experiments with cooled beam are the main tasks of the storage rings

at FAIR facility. In the case of CR, where a CCC will be installed, the anti-proton beams and secondary rare isotope beams will be pre-cooled and delivered to other storage rings. When operated in isochronous mode, the mass measurements of secondary short lived rare isotopes from the super-fragment separator (SFRS) are another major experiment planned at this storage ring [95]. In the due course of technical realization of the FAIR storage rings, the Cryring will provide a test facility for several relevant R&D projects and will stand for the continuation of the existing storage ring collaborations at GSI [96]. Together with ESR, advanced investigations which are relevant for the successful operation of the FAIR storage rings will be carried out at the Cryring. This will provide valuable feedback on operational concepts and experience for the operators on the new control systems of FAIR.

The intensity of stored and accelerated or decelerated beams is a key information in any storage ring. In case of Cryring, where highly charged heavy ions will be cooled, stored and decelerated down to few hundred $^{keV}/_{u}$, the intensities available for atomic physics experiments are expected to be in very low ranges, typically nA range. In addition the intensity of the cooled beams at low energy is limited by the space charge tune shift, especially in the case of bunched beams. For the atomic and molecular experiments, exact knowledge of the beam intensity is essential to determine the reaction rate with sufficient accuracy. Hence CCC will provide a perfect diagnostic tool to measure the intensity with absolute calibration.

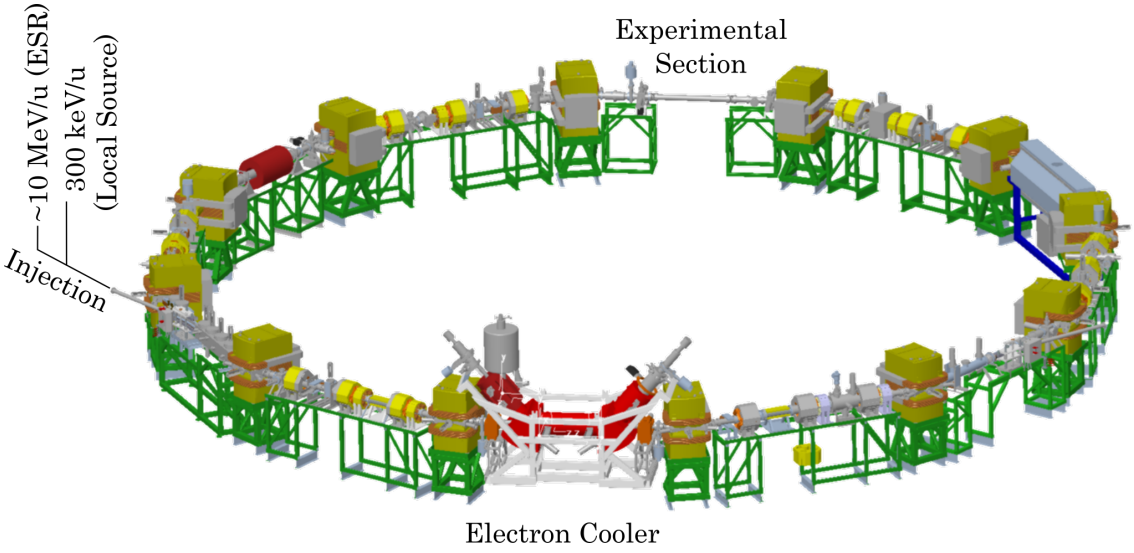

Figure 6.1: Schematic view of the Cryring at ESR. During first tests the CCC will be installed in the $\sim 3\,m$ experimental section of the ring.

While the FAIR facility is under construction with its modularized start version [97] currently underway, the Cryring will be operational at the GSI Target Hall in early 2016. An advanced CCC system will be installed in the Cryring experimental section and a number of test measurements and optimizations for the FAIR installations will be carried out.

6.2 Further Developments of CCC for FAIR

6.2.1 Vacuum and Cryogenic Solutions

In the GSI - CCC prototype, the vacuum surrounding the liquid helium cryostat is connected to the accelerator vacuum as illustrated in figure 3.1. Here, the radiation shield, the inner surface of the CCC outer shell, multi-layer insulation and helium container are exposed to the accelerator vacuum. The huge surface area of these components, especially the multi - layer insulation introduce limitations in the end pressure due to out-gassing. Hence in future CCC units, this approach cannot be applied due to ultra high vacuum requirements especially in the storage rings. Similarly for the realization of this vacuum range, bake-out is foreseen and the CCC units must be able to cope with it. In addition, any helium leakage would cause fatal errors in the NEG coatings used for the UHV, immediately resulting in long shut down periods. These brings a mandatory requirement of a separated insulation vacuum in the new CCC systems. The FAIR CCC units will have an individual insulation vacuum with a pressure in the $10^{-7}\,mbar$ range, containing the cryogenic components surrounding the beam pipe.

To reduce the heat radiation from the beam pipe at room temperature, the radiation shield (covered with multi - layer insulation) has to be extended into the warm-hole. The radiation shield which is kept at a temperature much lower than room temperature (as in the case of GSI - CCC prototype) will be acting as a thermal anchor for the cryogenic components. Similar to the warm-hole in the case of GSI-CCC prototype, the cryostat includes a warm-hole through the liquid helium cryostat which encloses the beam pipe and the radiation shield. Hence given by the relative increase in the inner diameter of the warm-hole, the pickup unit of the CCC system also has to be proportionally larger.

Given by the fact that the thermal load on the liquid helium cryostat has to be kept minimum. This is because the thermal fluctuations of the detector unit were found to have huge impact on the resolution of the system. At the same time, the requirement of a compact cryostat due to the minimum installation space available demands for a trade-off with the low thermal load design. For instance, the extensions of the warm-hole on either sides of the cryostat in the GSI - CCC prototype have to be avoided.

Another boundary condition in the design of new CCC units is highly restricted access in the beamline during operation of the system. This demands for automated cryogenic solutions. Since the installation points of CCC are spread wide across the FAIR facility, liquid helium supply lines will not be available in several locations and hence stand-alone liquid helium re-liquefaction solutions are foreseen.

Recently a new CCC system was installed in the Antiproton Decelerator (AD) ring at CERN in collaboration with GSI, Friedrich - Schiller - University, Jena and Helmholtz Institute, Jena [98]. This CCC system consists of a separated vacuum chamber and a stand-alone helium re-liquefaction unit based on pulse tube refrigerator as shown figure 6.2. In this CCC design (with the help of extensive simulations) mechanical vibration modes of the cryostat were identified and are damped using Titanium rods. The first beam measurements with this system are

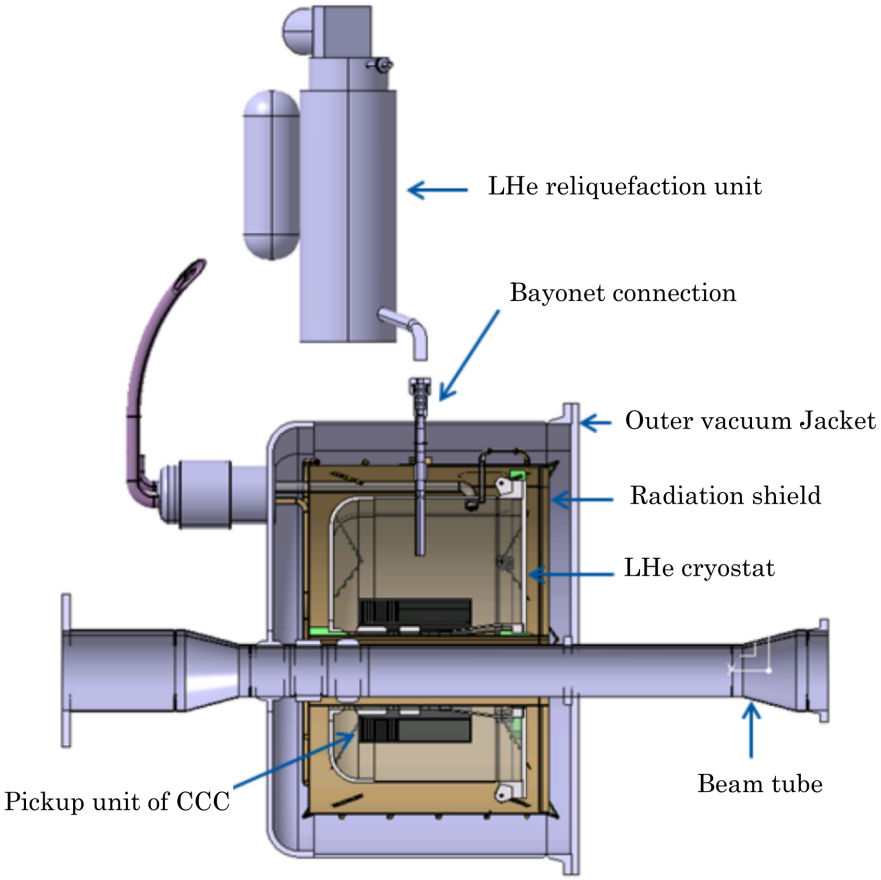

Figure 6.2: Cross-sectional view of the CCC system installed in the AD machine at CERN. Figure Courtesy, [98]

currently performed.

Although this design satisfies several boundary conditions, in the universal design for FAIR accelerators some changes are foreseen. Since the beam tube diameters in the FAIR are larger compared to the AD ring (150 mm instead of 100 mm), a larger pickup unit has to be designed. Moreover, for the installation in FAIR and Cryring@ESR, several modifications of the sensor units are foreseen especially in its initial stages of test measurements at Cryring. Hence access to the dc SQUID and associated electronics as well as the superconducting shieding without unmounting from the beamline are considered as an important requirement. Other design criteria are mechanical stability, minimum heat load through suspensions and decoupling of electromagnetic interferences from the liquid helium inlet siphon. This arises from the fact that most of the automated helium re-liquefaction solutions have the liquid helium inlet siphon permanently inserted into the cryostat. This leads to the mechanical vibrations being easily coupled into the cryostat along with environmental electromagnetic interferences. At FAIR, a system with buffer helium container is foreseen to overcome these problems.

6.2.2 Investigations of the Drift Mechanisms

As discussed in chapter 5 for reliable operation of the CCC the temperature and pressure dependence of its output has to be minimized. Since there are a number of possible mechanisms leading to drifts in the output, detailed investigations are planned to identify the leading contributions to the drift and its temperature dependence. In our measurements, temperature follows instantaneous to the pressure and hence the contributions from these two parameters are indistinguishable from the output variations of CCC. Although our investigations so far indicate the temperature being the primary reason behind the drift, further investigations are planned to confirm this. By operating the sensor unit in isobaric and isothermal conditions, the contribution of temperature and pressure can be investigated separately without influencing each other.

The scheme of the planned experiment to isolate the pressure influence on the pick up coil is as follows. A miniature pickup coil inside a chamber is immersed in a liquid helium bath cryostat. In the first case, the pressure inside the chamber of the pick up coil is kept constant. The temperature inside the closed liquid helium bath cryostat can be easily varied by pumping or by the application of slight excess pressure at the exhaust. Hence the temperature variations inside the chamber enclosing the pick up loop can be introduced and the drift measurements can be performed. In the second case, by applying pressure to the inner chamber which contains the pickup coil, one can introduce pressure variations, with very little influence on the temperature of the liquid helium bath. This allows the drift measurements in the presence of pressure variations without temperature dependence.

The next strong candidate for the drift is the thermo-electric voltage formation at the junctions of dissimilar metal contacts. This effect will be studied by producing temperature gradients in the feed-through and cabling scheme where the thermo electric voltage can be produced.

6.2.3 Improvement of Dynamic Range and Slew Rate Limitations

As mentioned before, the maximum dynamic range of the system is limited by the linear flux range Φ_{lin} in the flux-voltage characteristics. However, to overcome this limitation and achieve very high dynamic range, two different techniques can be used, known as "flux quanta counting" and "dynamic field compensation (DFC)". In the flux-quanta counting technique, the feedback range of the FLL electronics is set to $\pm 1\,\Phi_0$. When the input flux exceeds the feedback range (*i.e.* when the flux in the feedback loop exceeds $\pm 1\,\Phi_0$) the integrator is reset. This causes the feedback current and hence the output to drop abruptly to zero. As the net flux in the SQUID is quantized to integer multiples of a flux quantum, the new working point is set at the next quantum level of the $V - \Phi$ curve, which is indistinguishable in the FLL output. Hence after the reset, the output follows the input flux with a constant offset corresponding to one Φ_0. By counting the number of resets, the input flux is reconstructed and hence the dynamic range can be substantially increased.

The flux quanta counting method implies that instead of compensating the total flux in the SQUID, only a fraction of it is compensated by the feedback coil. This means in the case of high input flux ranges, the SQUID is exposed to a large flux. Although very high dynamic ranges can be achieved by this techniques in low noise environments, high noise levels can considerably

degrade the $V - \Phi$ characteristics. A large deviation in the slopes in the $V - \Phi$ characteristics can cause errors in the calibration and hence the efficiency of this technique. Dynamic field compensation technique can be applied to achieve high dynamic range and stable operation without this limitation. In DFC, a compensation flux Φ_C from an internal low noise current source is applied to the SQUID through a field compensation coil once the feedback range is reached. The amplitude of this flux is controlled such that the FLL output drops back to nearly zero. To ensure the FLL remains locked throughout the compensation process, the slew rate of the compensation flux should be kept well below the system slew rate. In this way the SQUID is always operated in a low field range. The DFC technique provide an additional possibility of avoiding issues with flux trapping and excess flux noise. These techniques to improve the maximum dynamic range of the system will be tested in the new CCC system.

Another limitation on the CCC measurement range is due to the slew rate limitation of the FLL circuit. One possibility of avoiding slew rate limitation is to reduce the bandwidth of the input circuit below the FLL circuit. This way the FLL will be able to follow changes in the SQUID and can hence compensate the input flux. By introducing a low pass filter by a proper parallel RC shunt in the flux transformer, signals above the desired bandwidth can be attenuated [99].

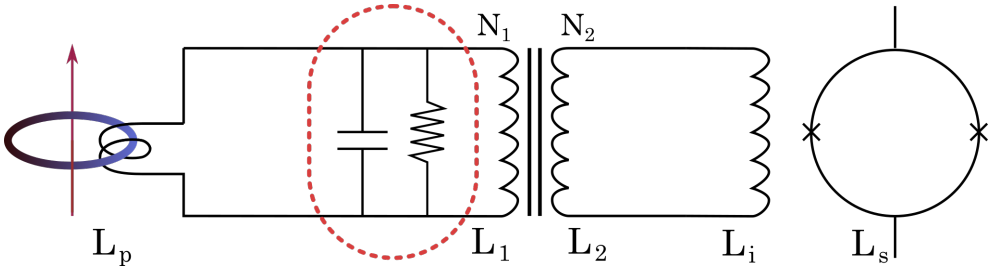

Figure 6.3: Flux transformer coupling the input signal to the dc SQUID with a low pass filter (shown in red)

6.2.4 Radiation Hardness Tests

Due to the increase in the intensity and energy of the ion beams in FAIR, the radiation levels[2] in the vicinity of the beamlines will increase by up to two orders of magnitude. Hence the materials close to the beamline will be exposed to secondary radiations comprising of a complex spectrum of gamma, neutrons, protons and heavier particles depending on the position. The consequences of radiation interact with solid materials depends on the type, mass, charge and Kinetic Energy of the incident particle and type of the target material. In the case of CCC systems, the radiation damage is critical for its electronic components rather than the bulk material. Hence dc SQUID and the FLL electronics are required to undergo radiation hardness tests for proper long term operation of the CCC system.

The incident particles can be divided into two groups: neutral and charged particles. The neutral particles of interest are neutrons and photons. Neutrons may interact with atomic

[2]The radiation is produced by the particles deviated from the primary trajectory of the beam that collide with accelerator components or planned collisions with dense materials.

nuclei by elastic collisions or inelastic reactions causing ionization and nuclear displacement damages. On the other hand, photons can interact with target material via Compton scattering, photoelectric effect or pair production depending on the energy of the incident photon and the atomic number of the target. Charged particles (proton, heavy ions and electrons) differ from the neutral particles since they mainly interact through Coulomb attraction or repulsion with electronic clouds of the target atoms.

The radiation effects on semiconductors in the accelerator environment can be divided into short-term temporary effects or long-term permanent effects. In silicon based electronic components, main consequence of radiation is ionizing effects and displacement damages (of atoms). Generally Gamma radiation contributes to the maximum radiation damage in the semiconductor components, mostly in the form of ionizing effects. Ionization effects can lead to enhancement of conductivity through production of excess charge carriers, trapped charges and chemical effects [100]. Another important source of circuit malfunction are Single Event Effects (SEEs), a phenomena induced in a semiconductor device by the impact of a single particle or ion. A SEE generates an immediate logical state change in one or more transistors which can influence the complete digital circuit.

In case of modern integrated circuits based on complementary metal-oxide semiconductor (CMOS) technology, where the gate oxide thickness are typically several atomic layer thick, ionization effects are the primary cause of radiation damages. These damages will add up over time and can persist for hours to years. Finally it can end up in the complete failure of the electronic component. Although these sub-micron devices are relatively insensitive to radiations compared to the analogue electronics, their demanding electrical parameters and very low input specifications (*e.g.* operational amplifiers and ADCs) can be significantly affected by radiation. Significant concerns of radiation include ionization damages in MOSFETs, CMOS and other linear devices and latch-up in CMOS circuits. Details on various influences of radiation on electronic components can be found in Ref.[101, 102].

Most of the modern hybrid electronic components are manufactured with limited information and "tracability" about the internal components. In addition, several components are considered to be proprietary by manufacturers. Hence short term irradiation studies of the dc SQUID and FLL electronics are planned to be performed at GSI, to investigate the limitations of the CCC system which consisting of various of the above mentioned components. The CCC installation point with maximum radiation levels will be in front of the beam dumps of SIS100/SIS300. At these locations an absorbed dose of up to $5\,Gy/h$ are expected [103]. Hence by irradiation with heavy ions and photons, using appropriate dose rates, the effects of radiation on the dc SQUID and the FLL electronics will be studied.

6.3 Optimization of the Magnetic Shield for CCC

As it was already shown in the earlier chapters, the superconducting magnetic shield geometry is an important component of the CCC in defining the field sensitivity of the system. It is based on the fact that the magnitude of the stray magnetic fields in all cases are several orders of magnitude higher than that of the beam's magnetic fields and must be efficiently attenuated.

For the CCC units at FAIR, the beam tube diameters are larger compared to GSI prototype . Additionally the requirement of a separated isolation vacuum demands for the magnetic shield to have a large inner diameter. For the design of the compact cryostat, however the total size and mass of the geometry has to be minimized. This leads to an essential trade-off between the attenuation factor and the geometric parameters such as number of meander units (N), gap width between two consecutive plates (g) and their radial width ($R_{out} - R_{in}$).

To understand the underlying physics behind the attenuation of the magnetic field as it propagates through the magnetic shield and the factors influencing it, FEM simulations are performed using Comsol Multiphysics™.

6.3.1 Model of the Shield Geometry

As one of the basic characteristic properties, the superconducting surface can be assumed as an ideal diamagnetic surface. This assumption gives that the normal component of magnetic field on a superconducting surface is zero and hence the magnetic flux inside the material will vanish beyond its superconducting penetration depth λ_L. Since the material thickness is several orders of magnitude larger than λ_L and the material properties are not interesting in this context, the superconducting volume is removed from the model for the simulation (shown in gray in figure 6.4(a)). In case of the finite element method, the number of mesh cells exponentially increases the computational requirements. Hence this procedure will not only simplify the analysis, but also improves the computational capability by reducing the number of mesh cells to be solved.

Due to the nature of the propagating magnetic field through the superconducting meander shaped path (which will be shown later), 2D symmetry cannot be applied on the geometry. However the geometry possesses mirror symmetry for the 180 degree rotation of the axial cross-section as shown in figure 6.4(b) which is used in this analysis. Although the model is simplified by removing the superconducting material and cross-sectional symmetry, extremely small gap-width ($0.5\,mm$) compared to the total geometry results in a large number of mesh cells to be solved. This again would set challenges to the computing power available and hence simpler geometries were studied for analyzing the general influence of individual parameters. A cylindrical volume is defined at the opening of the shield where the external magnetic field is applied (left hand side in figure 6.4(b)

To quantify the number of meander shaped paths in the shield geometry, a single meander unit is defined as a curved path formed by three consecutive circular discs as shown in the figure 6.4(a). The superconducting discs of thickness 't' forms a meander path of width 'g' having minimum and maximum radii 'R_{in}' and 'R_{out}' respectively.

In the magneto-static case where no currents are present in the ideal diamagnetic boundary, the problem can be solved by scalar magnetic potential, V. That means the magnetic field outside the superconductor can be derived from the scalar magnetic potential which are connected by, $B = \nabla V$ and obeys Laplace's equation, $\nabla^2 V = 0$. The diamagnetism of the superconductor can be described by,

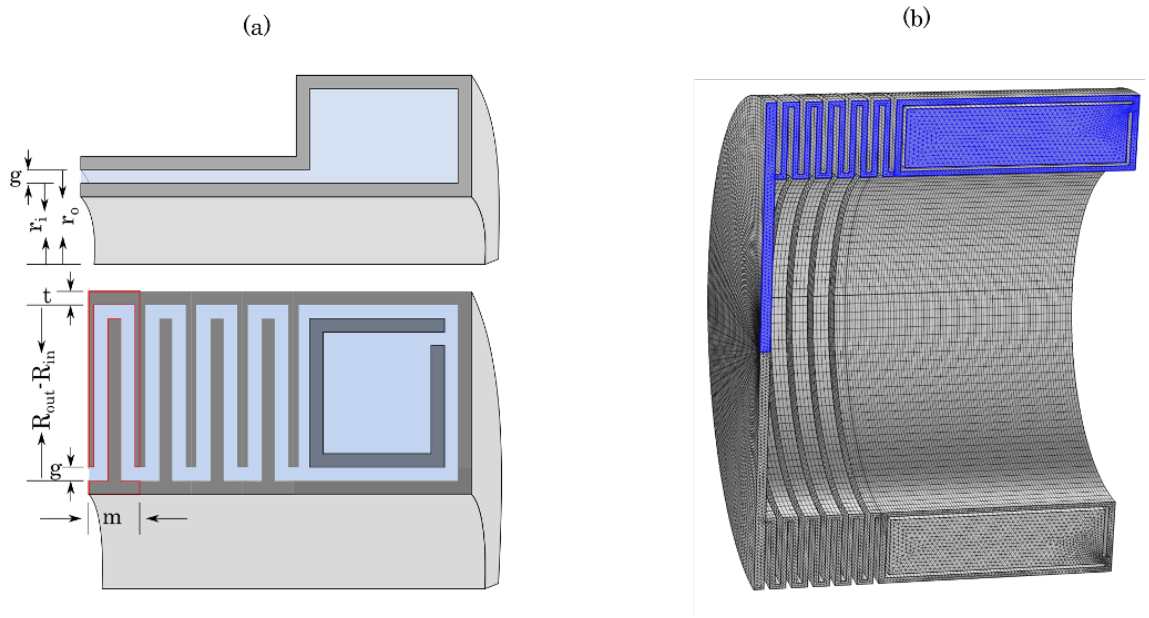

Figure 6.4: (a) Parameters of the coaxial cylinder and shield geometry considered for the simulations. Red contour in the shield represents a single meander unit (indicated by m). (b) Meshed model of the shield used for the simulation. In both images of the shield, the high permeability ring core is not shown as it is not included in the calculations.

$$\frac{\partial V}{\partial n} = 0$$

where n represents the normal vector to the superconducting surface. In the simulating model, ideal diamagnetic boundary conditions on the shield surface are realized by applying the *magnetic insulation* boundary condition to the superconducting boundaries of the shield. On these boundaries the magnetic insulation boundary condition realizes the Dirichlet boundaries, which sets the normal component of the magnetic vector potential to zero while keeping the parallel components of the field. That is,

$$n \times A = 0$$

Another boundary condition used to achieve symmetry of the problem is the *perfect magnetic conductor* boundary condition which sets the parallel component of the magnetic vector potential to zero,

$$n \cdot A = 0$$

Depending on the direction of the external field, the magnetic insulation and perfect magnetic conductor boundary conditions are applied on the symmetric planes of the shield geometry so that only half of the total shield has to be solved for the complete solution.

Validity of the simulation.

The field attenuation through an ideal diamagnetic meander shaped geometry is analytically studied by Grohmann *et.al.* [53, 104]. Following the same procedure, a simplified case of field attenuation by a coaxial cylinder (as shown in figure 6.4(a), top) can be considered to check the accuracy of the simulation. The cylindrical path formed by the superconducting walls of the coaxial cylinders has an opening at one end where a magnetic field perpendicular to the cylindrical axis is applied as shown in figure 6.5.

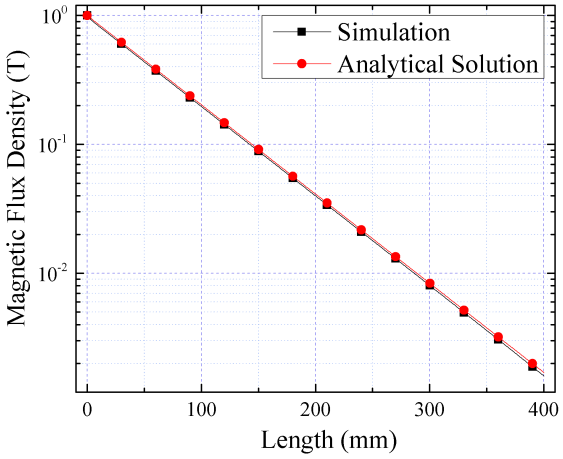

Figure 6.5: Comparison of simulations to analytical values for field attenuation in a superconducting coaxial cylinder

In the analytical approach, as discussed above, the magnetic field can be estimated by deriving an expression for the scalar potential V. The Laplace equation of the scalar potential in the cylindrical co-ordinate system can be written as,

$$\frac{1}{r}\frac{\partial}{\partial r}\left(r\frac{\partial V}{\partial r}\right)+\frac{1}{r^2}\frac{\partial V^2}{\partial \phi^2}+\frac{\partial^2 V}{\partial z^2}=0 \tag{6.1}$$

Here r, ϕ, z are the cylindrical co-ordinates. The solution of this Laplace equation can be given by the twofold infinite series,

$$V\left(r,\phi,z\right)=\sum_{n=0}^{\infty}\sum_{all\,k} V_{nk}(kr)\,\sin\left(n\phi+\nu_n\right)\exp\left(-kz\right) \tag{6.2}$$

In the equation, ν_n represents the phase angle with n characterizing the harmonics of the Fourier series of the scalar potential with respect to the angle ϕ. By varying n, different field configurations can be distinguished. That is $n = 0$ of the scalar potential represents a longitudinal field (parallel to the cylindrical axis of the shield), $n = 1$ represents a dipolar field centered at $r = 0$ and $n = 2$ stand for a quadrupolar field [105]. Hence by determining all possible values k and by solving each of the eigenvalue problems, the field at any z value can be estimated. In each case, the attenuation factor can be defined as,

$$A^n = 20\log\left(\frac{B^n_{out}}{B^n_{in}}\right) \tag{6.3}$$

where B^n_{out} is the field just outside the opening of the superconducting path and B^n_{in} , the field inside the cylindrical path.

The solution in the case of a magnetic field applied in a direction perpendicular to the cylindrical axis of the shield (transverse field) can be approximately given by the general solution [104],

$$B_{in} = B_{out} \cdot exp\left\{ -\frac{2}{\left(1 + \frac{r_i}{r_o}\right)} \frac{z}{r_o} \right\} \tag{6.4}$$

In case of an external longitudinal field, the field attenuation can be approximately given by the relation,

$$B_{in} = B_{out} \cdot exp\left\{ -\frac{\pi}{\left(1 - \frac{r_i}{r_o}\right)} \frac{z}{r_o} \right\} \tag{6.5}$$

In the case $r_i \approx r_o$, it can be seen from equation 6.5 that the longitudinal field components undergo strong attenuation compared to the transverse field. Hence in the case of $z \gg r_o$, the contribution of longitudinal field is negligible. Therefore, in the following discussions we consider only the case of perpendicular magnetic fields. The result of simulation in this case is compared with this analytical result given by equation 6.4. As the figure 6.5 indicates, the simulation shows an identical attenuation as it is estimated by the analytical solution. Hence this scheme is used for simulation of the magnetic shield geometries.

6.3.2 Azimuthal Magnetic Fields

Following the formation of the magnetic shield given in section 3.3.1, the shield geometry can be visualized as a coaxial cylinder folded in to the form of a cavity. It can also be shown with the analytical solution [105] that the azimuthal field produced by a current element within the geometry does not undergo any attenuation. In addition, it also gives the important result that the field inside the shield is independent of the position of the current element within the geometry. Hence for a thin wire loop carrying a current I through the axis of the shield, the field at the interior, at a distance $\vec{r}$ from the axis of the current element can be given by Ampere's law,

$$B_{in} = \frac{\mu_0 \cdot I}{2\pi r} \tag{6.6}$$

The result of the simulations in the case of the shield geometry having 10 meander units having a gap width of $2\,mm$ are shown in figure 6.6(a).

The surface current through a cylindrical surface at the axis of the shield produces the azimuthal magnetic field, the magnitude of which is shown by the first legend (left hand side in figure 6.6(a)). The distribution of the magnetic field through the meander shield geometry is shown by the scale on the right hand side. The comparison of the simulation result of the field along $\vec{r}$ direction with the numerical calculation shows good agreement with the analytical value as shown in figure 6.6(b).

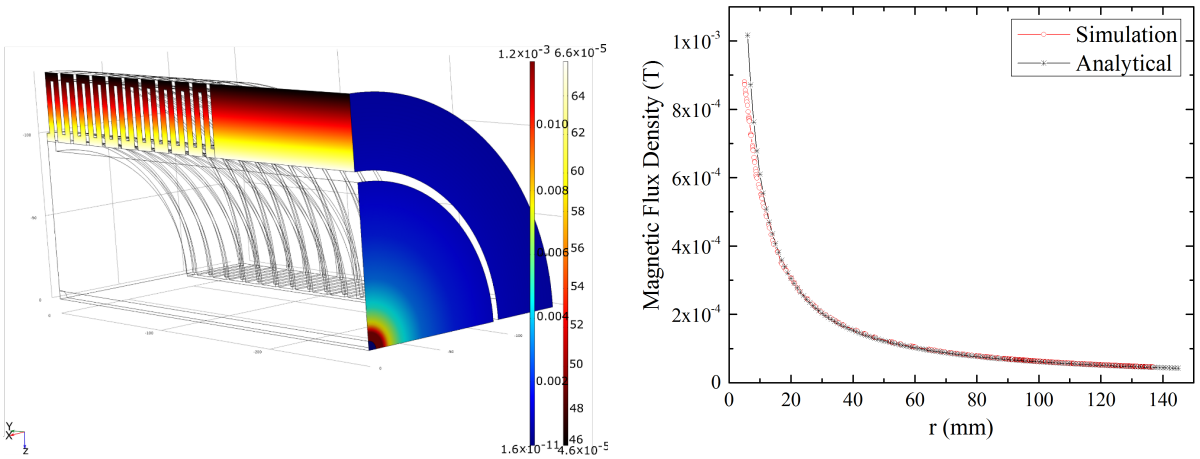

Figure 6.6: (a)Simulation showing the value of azimuthal magnetic field produced by a surface current passing through the axis of the shield geometry. (b)Comparison of the simulation result with the analytical value for the magnetic field along the radial ($\vec{r}$) direction.

6.3.3 Attenuation of Dipolar Magnetic Fields

To reduce the effective number of mesh cells in the model, a simpler case of $g = 2\,mm$ is considered to study the nature of field attenuation. The attenuation through a single meander unit as a function of the radial distance for a number of gap widths is shown in Figure 6.7(a). Here, the length corresponding to the positive radial direction ($+\vec{r}$) shows exponential attenuation whereas the length corresponding to $-\vec{r}$ shows significantly less attenuation. As the length in $\vec{z}$ direction (which itself has exponential attenuation as seen in the case of a coaxial cylinder) is considerably small in this case, the contribution to the attenuation can be neglected. Reduction in the attenuation factor against the increment in the gap width between two consecutive meanders is shown in figure 6.7(b). As g is increased, the reduction in the attenuation was found to follow roughly a linear behavior.

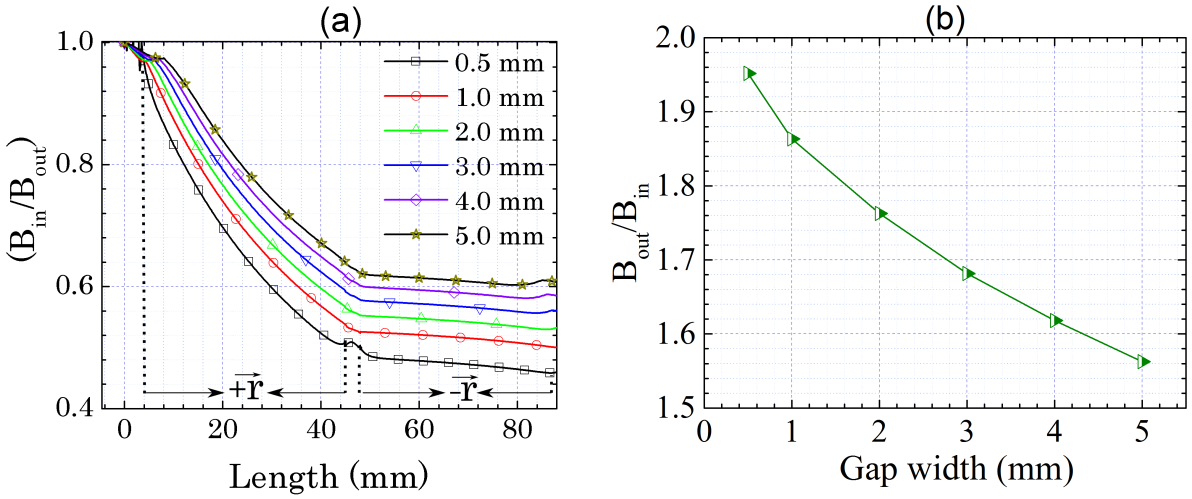

Figure 6.7: Comparison of field attenuation through a single meander unit along the arc length of the shield for various gap-width. (b) Variation of attenuation as a function of gap width.

Another interesting characteristics of the external dipolar magnetic field propagating through the meander shaped shield geometry is given in figure 6.8. As the field gradually passes through each meander units, the field tends to "align" to the shape of the shield [45]. In the figure, the external magnetic field is applied in the X direction (as shown by the arrows) and the direction of propagation inside the shield (uniform) is shown by the green ribbons. This gives rise to the fact that the external magnetic fields will be guided into the azimuthal direction by the shield geometry irrespective of their initial directions.

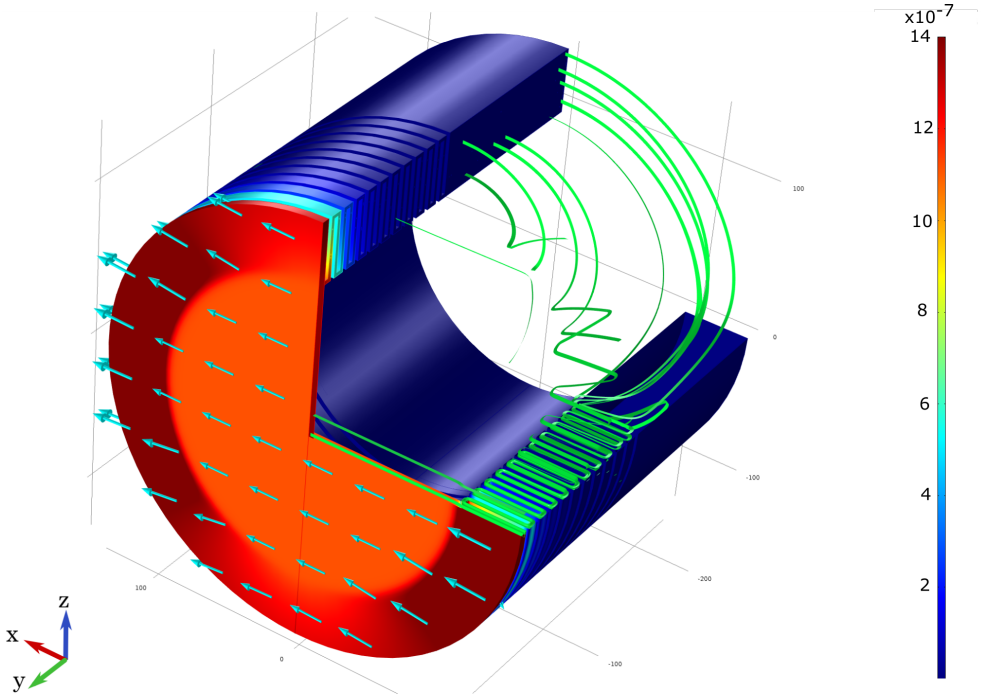

Figure 6.8: Streamline plot showing the direction of the external magnetic field (perpendicular to the cylindrical axis) while passing through the meander units ($g = 2\,mm$) to the interior of the shield. The green ribbons indicates the direction of the magnetic field lines and are plotted for uniform density.

Increasing the diameters of the shield for FAIR will result in increased shield mass, which considering the cryogenics should be kept at minimum. This trade-off lead to the requirement of keeping the number of meanders and gap width at a minimum. Hence the influence of variation of the inner and outer diameters (R_{in} and R_{out}) of the shield is an important design parameter.

Following 6.7(a), the field undergoes exponential attenuation in the radial direction. Hence by increasing the radial width, one can increase the attenuation. On the other hand, an increase in the diameter of the shield will again result in an increased mass. However as it can be found in the case of a superconducting coaxial cylinder of gap-width g and a radial width d, as the inner and outer radii increased (keeping d constant), the attenuation undergoes degradation. This mechanism is analogue the unexpected behavior of a superconducting hollow cylinder having stronger attenuation than a coaxial cylinder as shown by Ref.[53]. Following this behavior, it is obvious that the inner diameter of the shield geometry has to be kept minimum for maximum attenuation. Hence with the same number of meanders, gap-width and radial width, it can

be seen that due to the smaller inner and outer radii, the GSI - CCC prototype posses better attenuation than the larger shields.

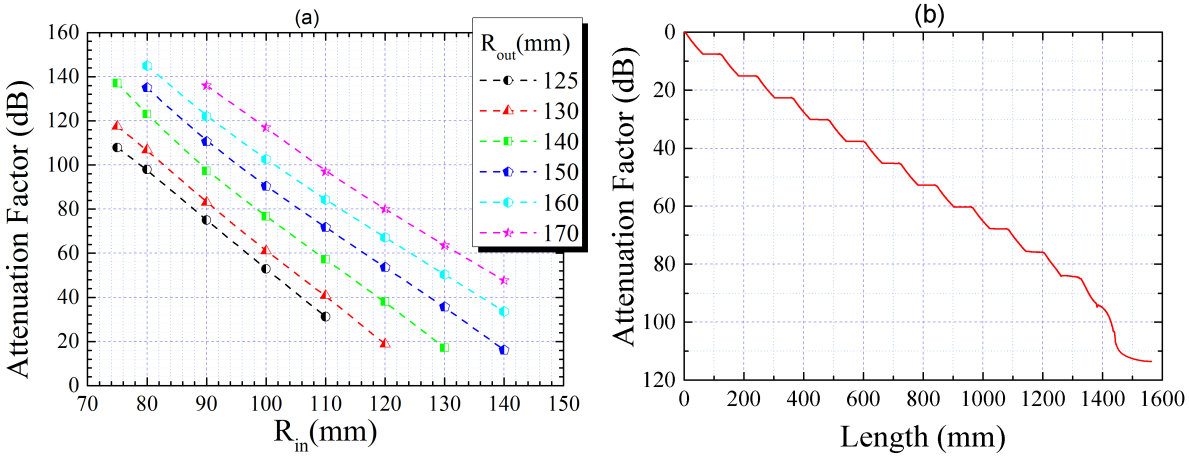

Figure 6.9: (a) Attenuation factor measured by the simulation for a set of inner and outer diameters of the shield. (b) Attenuation of the magnetic field along the path formed by the meander unit to the interior of the shield. Both the simulations were performed for a gap-width of $2\,mm$.

To study the influence of different shield diameters on the attenuation factor, calculations for a set of inner and outer diameters were performed as shown in figure 6.9(a). Using a gap width of $g = 2\,mm$, while shield with dimensions of GSI-CCC prototype ($R_{out} = 125\,mm$ and $R_{in} = 75\,mm$) shows an attenuation of $108\,dB$. The shield dimensions of $R_{out} = 140\,mm$ and $R_{in} = 92.5\,mm$ (dimensions used in the AD installation in CERN) show an attenuation factor of $91\,dB$. For the FAIR installations, the planned radii of the shield are $R_{out} = 170\,mm$ and $R_{in} = 110\,mm$. In this case, the attenuation factor will be further reduced to $85\,dB$. In the real case of gap widths $g = 0.5\,mm$, the relative changes in attenuation factor are expected to be almost identical.

Two possibilities to compensate the reduced attenuation factor are either increasing the outer radii of the shield or increasing the number of meanders. Since increasing the outer radii has practical limitations given by the cryostat design criteria and construction point of view, efficient possibility is to increase the number of meander units. As shown in figure 6.9(b), by adding two additional meander units, the attenuation factor can be increased by approximately $25\,dB$. As shown in the roughly linear increase in the attenuation factor with decrease in gap width, a proportional increase in the attenuation factor can be expected in case of shield with $g = 0.5\,mm$.

The simulation shows the mechanism of the field attenuation by the superconducting shield and the variation in the attenuation according the various geometric parameters. However this simulation is based on a number of idealistic assumptions which may need to be extended further to include all practical contributions to the attenuation factor. Here for the simulations, we have neglected the formation of super-current through the superconducting surfaces. Similarly the influence of the high permeability ring core has to be included into the simulation for any comparison with the empirical results. In the presented case, the magneto-static approximation

neglects possible mechanical vibrations which introduces a time dependence of the magnetic fields which might influence the attenuation factor.

Chapter 7

Summary

This thesis describes the investigations on a Cryogenic Current Comparator (CCC) for highly sensitive beam intensity measurements. Within the scope of this work, the first CCC system developed for ion beam current measurements at GSI was recommissioned and upgraded with new, advanced sensor components. Successful intensity measurements of ion beams down to nA range were performed at the extraction section of the GSI synchrotron SIS18 and were compared with conventional beam intensity measurement devices (Secondary Electron Monitor). Furthermore it was shown that the CCC is a useful tool to analyze the micro-structure of slowly extracted beam spills with a large bandwidth (in our case limited to $10\,kHz$). Parameters which influence the performance of CCC system, mainly flux noise, temperature/pressure and trapped flux effects are investigated during further measurements with a focus on the advanced CCC systems for the upcoming accelerator facilities, Cryring at ESR and the FAIR.

Being one of the most important parameters to be measured in an accelerator, intensity measurement techniques are generally based on detection of the transverse electromagnetic field of the beam or the energy deposition of the beam while passing through a sensor material. Due to the availability of magnetic materials with high permeability values (μ_r), which can be efficiently used for the precise measurement of azimuthal magnetic field of the beam, Beam Current Transformers (BCT's) are the most widely used techniques. BCT's provide non-interceptive measurement of the beam intensity independent of particle energy and ion type. However the detection thresholds of the BCT's are limited to about $1\,\mu A$ due to noise limitations in the magnetic materials. To measure the intensity below this range, typically a number of devices are used in tandem to cover the entire spectrum of the beam intensity.

Conventional devices used for intensity measurement below the detection threshold of the BCT's are mainly intercepting techniques such as Scintillators, Ionization Chambers (IC) and Secondary Electron Monitors (SEM). These intercepting techniques which are based on the interaction of particle beam with the sensing material have limitations in case of high energy, high intensity beams and also need to be calibrated with non-intercepting techniques. In the case of intensity measurements at FAIR accelerator beam lines, (with an energy up to $29\,Gev/u$ in SIS100 and further up to $45\,GeV/u$ in SIS300), the intensity measurements have to be performed with direct, non-intercepting techniques. Moreover, given by the long extraction times (up to 100 seconds) in case of slow extraction from the synchrotrons, beam intensity down to several

nA also need to be covered. The CCC system - as it is demonstrated in this thesis - covers an intensity range from few nA to several hundreds of μA (depending on the sensitivity settings) without the need of any external calibration, irrespective of the energy, ion-type and trajectory of the ion beam. Hence to satisfy the boundary conditions given at various locations, CCC units are planned to be installed at 6 different locations spread across the High Energy Beam Transport (HEBT) sections and storage rings of the FAIR facility.

The CCC prototype consists of a liquid helium bath cryostat surrounded by a radiation shield, both are suspended within the outer vacuum chamber. It includes a warm-hole through the liquid helium cryostat for the beam passage. A superconducting pickup unit is installed inside the liquid helium cryostat surrounding the warm-hole. The pickup unit consists of a magnetic shield enclosing a high permeability ring core surrounded by a niobium pickup coil. When the beam passes through the warm-hole, azimuthal magnetic field of the ion beam produces superconducting screening current on the pickup coil proportional to the beam current. This current is coupled to a superconducting sensor unit through a superconducting flux transformer. The signal proportional to the beam current is further linearized and amplified at the sensor unit and is read out at the data acquisition unit. The sensor unit consists of a SQUID (Superconducting Quantum Interference Device) sensor operated in Flux Locked Loop (FLL) mode using associated SQUID electronics.

In the first phase of this thesis work, the existing CCC system at GSI - developed during early 1990's by A. Peters, *et. al.* - was upgraded after extensive refurbishments and optimizations on the vacuum and cryogenic components. After successful test measurements with this system, the SQUID sensor unit and the associated FLL electronics were replaced with advanced components from commercial vendors with the aim of serial production of the CCCs for FAIR. After successful test measurements in lab environment, using a calibration wire simulating the beam current, the GSI-CCC prototype was installed at the extraction section of SIS18 for beam measurements. Given by the extreme sensitivity of superconducting sensor components to external noise, detailed investigations were performed to optimize the performance of the CCC system at minimum external electromagnetic interferences. This included isolation of electrical noise using isolation-amplifiers and measurement of various mechanical resonances on the CCC vacuum chamber. In addition, precise mechanical alignment of the liquid helium cryostat was carried out to compensate thermal compression of the titanium suspensions.

For the intensity measurements with the GSI-CCC prototype, the sensor unit was adjusted to optimum working point in the flux-voltage characteristics, so that the dc SQUID has maximum sensitivity and dynamic range in the FLL mode of operation. Under optimized working conditions in the beam line, the performance of dc SQUID was characterized and a white noise level of $11\,{}^{pA}/\sqrt{Hz}$ at $2\,kHz$ was measured which corresponds to a flux noise of $80\,{}^{\mu\Phi_0}/\sqrt{Hz}$. Using the calibration wire loop wound around the pickup unit, the current calibration factor was calculated to $69.53\,{}^{nA}/\Phi_0$. In the most sensitive range of the SQUID electronics (defined by the feedback resistance, $R_F = 100\,k\Omega$), this factor corresponds to $74.2\,{}^{nA}/V$ at the data acquisition unit. After characterization and calibration measurements, the CCC was operated in the remote operation scheme for the beam measurements.

Particle beams of Ni^{26+} at an energy of $600\,{}^{MeV}/u$ from SIS18 extracted by slow extraction

scheme were used for the beam intensity measurements. Extraction times from $64\,ms$ to $5\,s$ were recorded and beam currents of different spills in the intensity range from $2\,nA$ to $105\,nA$ were measured by the CCC. The current resolution of the system was measured to $6 - 120\,{}^{pA}/\sqrt{Hz}$ within a bandwidth of $DC - 10\,kHz$. In the presence of excess low frequency noise, the CCC was able to measure a beam current down to $2\,nA_{rms}$ corresponding to a signal to noise ratio of $6\,dB$. The beam signals measured by the CCC were also measured by a SEM which was installed about $1\,m$ downstream on the same beam line. The simultaneous measurements of the spill structure were compared and evaluated in both, time and frequency domains. The beam signals were measured by CCC with the bandwidth limited to $10\,kHz$ by activating the anti-alias filter at the readout electronics. The comparison of intensity values measured by both the systems showed excellent linearity within 0.7% over 65 different spills.

Due to the instabilities (ripples) in the synchrotron magnet power supplies, the spill structure of the coasting beam contains spikes (several times higher than the average beam current) and over modulations resulting in discontinuous particles in the spill structure. Bunching the beam inside the synchrotron was shown to improve the spill structure due to time dependent momentum deviation of single particles and its coupling to the tune spread. By analyzing the spill structure of the extracted beam using CCC, a suppression of the over-modulation and corresponding reduction of the peak amplitudes of the spikes was demonstrated for various bunching voltages. As a characteristic property of this technique, the synchrotron frequency and its harmonics were observed in the frequency spectrum of the spill and verified with numerically calculated frequencies for each bunching voltage, confirming the precision of the CCC measurements.

For further characterization of external noise influences on the CCC measurements in an accelerator environment, detailed offline test measurements were performed at the same beam line with comparable ambient fields. Two main effects observed during the measurements were distortion of the flux-voltage characteristics and a long-term drift in the CCC output. The rate of the later was found to be a function of thermal fluctuations inside the liquid helium bath cryostat. The rate of the drift was measured in different stages of liquid helium filling and was observed to be reduced as the liquid helium cryostat reaches better thermal stability. During three cooling cycles, the drift rate was found to be between a highest rate of $1.6\,{}^{nA}/_{s}$ to a lowest drift of $6.2\,{}^{pA}/_{s}$ at different liquid helium levels in the cryostat. A number of factors contribute to the drift in CCC output. The main influence arise from the Seebeck effect (at the electrical feed-throughs) and from flux trapping inside different superconducting coils.

In addition to the long-term baseline drift, it was also observed that the CCC output is highly sensitive to any pressure or temperature changes in the liquid helium cryostat. As the magnitude of pressure and temperature effects was found to be significant compared to the typical beam intensity (an increase of $36\,mK$ caused a baseline drift equivalent to $1.107\,\mu A$ at the CCC output), detailed investigations were performed to characterize those effects. Synchronous measurements of pressure and temperature inside the liquid helium cryostat were compared with the CCC output. From a set of pressure-temperature measurements across the CCC baseline, it was observed that the magnitudes of these factors are strongly dependent on ambient conditions such as liquid helium level inside the cryostat and time after filling. Since liquid helium re-liquefaction units (which causes higher thermal instabilities) are foreseen at FAIR for continuous cryogenic

operation, methods to reduce the influences of thermal instabilities on the CCC measurements are proposed.

The dynamic range of the CCC system is defined by maximum voltage limit of the feedback loop in the FLL electronics. With a voltage limit of $10\,V$, the dynamic range of the CCC system is calculated to $\pm 9.37\,\Phi_0$ which is equivalent to $\pm 93\,\mu A$ in the least sensitive range (corresponding to $R_F = 0.7\,k\Omega$). However when high flux noise causes the feedback error flux to exceed the linear flux range in the flux-voltage characteristics of the SQUID electronics, the dynamic range is found to decrease. With a limited bandwidth of the FLL electronics ($57\,kHz$), the slew rate limitations is found to cause flux jumps when the feedback error flux exceed $\Phi_0/2$ which results in temporary loss of the working point. Typical occurrence of flux jumps are presented and methods to improve the dynamic range and slew rate of the system are discussed.

From the results of investigations on the GSI-CCC prototype and operational experience, the general requirements for the advanced CCC systems are evaluated. Apart from a number of specific boundary conditions at individual locations, main general boundary conditions include compact cryostat design, ultra high vacuum (UHV) conditions in the beamlines, large radiation fields and large beam tube dimensions. A universal design of an advanced CCC system which satisfies these boundary conditions is currently under development at GSI with a goal of serial production for all future installation locations. This CCC system, will be first commissioned at the CRYRING at ESR. Here it will be used as the test bench for a number of test measurements such as automated cryogenic operation and the common Front End Software Architecture (FESA), which will be implemented for data acquisition and control systems in FAIR facility.

The requirement of a larger beam tube diameter ($160\,mm$) compared to the GSI-CCC prototype ($100\,mm$), together with insulation vacuum for the operation of CCC system under UHV conditions, demands for a larger inner diameter of its superconducting magnetic shield. Hence for the optimum dimensions of magnetic shield for the compact cryostat design, dependence of various geometric parameters was investigated using FEM simulation package, Comsol Multiphysics^{TM}. The influence of number of meander-shaped superconducting path leading into the interior of the shield, gap-width of the superconducting path and different ratios of inner and outer radii were calculated. In these simulations, it was quantitatively shown that the larger shield diameters will reduce attenuation of the most prominent magnetic field component, *i.e.* the magnetic field component perpendicular to the beam axis. Hence in the case of new CCC systems, to compensate the reduction in the attenuation factor, an obvious option is to increase the number of meander shaped superconducting path. From the calculated attenuation factor for various number of meander paths, a compromise between the required attenuation factor and the Niobium costs (respectively insertion length) has to be found.

Zusammenfassung

Die vorliegende Arbeit befasst sich mit Untersuchungen an einem kryogenen Strom-Komparator (Cryogenic Current Comparator, CCC) zur hochempfindlichen Messung von Teilchenströmen am Beschleuniger. Im Rahmen dieser Untersuchungen wurde ein in den neunziger Jahren bei GSI entwickelter CCC wieder in Betrieb genommen und dabei mit zeitgemäßer, verbesserter Sensorik und Elektronik aufgewertet. Nachdem das neue CCC-System in einer Extraktions-Strahllinie des SIS18- Synchrotrons der GSI installiert wurde, gelang dort ein erfolgreicher Nachweis von Ionenströmen bis in den Bereich weniger nA. Gleichzeitig wurden die ermittelten Stromwerte mit denen eines herkömmlichen Sekundärelektronen-Emissions-Monitors (SEM) verglichen. Es konnte gezeigt werden, dass der CCC ein äußerst nützliches Werkzeug für die Analyse der Mikrostruktur des Spills langsam extrahierter Ionen darstellt, da er hierfür eine hinreichende Messbandbreite (hier limitiert auf ca. $10\,kHz$) aufweist.

Weiterhin wurden bei Messungen zum magnetischem Fluss-Rauschen, zu Temperatur- und Druck-Effekten sowie zum Einfluss von eingefangenem magnetischem Fluss Parameter untersucht, welche die Leistungsfähigkeit eines CCC (besonders hinsichtlich der gestiegenen Anforderungen in den zukünftigen Beschleunigeranlagen CryRing@ESR und FAIR) wesentlich beeinflussen.

Die Bestimmung der Strahlintensität ist eine der wichtigsten Messungen am Beschleuniger. Sie basiert in der Regel auf der Detektion der den Strahl umgebenden transversalen bzw. azimutalen elektromagnetischen Felder oder auf der Bestimmung der Energie-Deposition des Strahls beim Durchgang durch Materie. Sogenannte Strahlstrom-Transformatoren aus weichmagnetischen Werkstoffen höchster Permeabilität (μ_r) sind die verbreiteten, effizienten Messgeräte zur Erfassung der magnetischen Azimutalkomponente eines Ionenstrahls. Sie ermöglichen eine nicht-destruktive Strommessung, unabhängig von Ionensorte und –Energie. Bedingt durch das Eigenrauschen ihres Ferromagnetikums und der folgenden Mess-Elektronik endet ihr praktisches Auflösungsvermögen bei etwa $1\,\mu A$. Um die Strahlintensität unterhalb dieses Bereichs zu messen werden in der Regel sukzessive Apparaturen mit überlappenden Messbereichen kombiniert. Herkömmliche Instrumente zur Intensitätsmessung im Bereich unterhalb der Auflösungsgrenze der BCTs sind Szintillatoren, Ionisationskammern (IC) oder Sekundärelektronen-Emissions-Monitore (SEM). Da diese Apparaturen alle auf der Interaktion der Strahlteilchen mit dem Detektormaterial basieren, beeinflussen oder zerstören sie den Strahl. Des Weiteren besitzt die Energie- und Ionenabhängige Wechselwirkung Limitierungen hinsichtlich Strahlenergie und –Intensität. Die Instrumente benötigen daher eine Kalibration mit Hilfe einer nicht-destruktiven Absolutmessung.

Für die Strahltransportstrecken der FAIR-Anlagen sind direkt messende, zerstörungsfreie Messsysteme zur Erfassung der Strahlintensität bei Energien von bis zu $29\,^{GeV}/_{u}$ hinter dem SIS100, und bis zu $45\,^{GeV}/_{u}$ am SIS 300 gefordert. Bedingt durch Extraktions-Zeiten von bis zu 100 Sekunden können bei der langsamen Teilchen-Extraktion aus den Synchrotronen Strahlströme bis zu wenigen nA auftreten. In dieser Arbeit wird gezeigt, dass das verwendete CCC-System – lediglich abhängig vom vorgewählten Messbereich – eine Spanne von einigen nA bis in den Bereich mehrerer hundert µA abdecken kann (unabhängig von Energie,Teilchensorte oder Trajektorie). Es ist daher vorgesehen, zur Abdeckung der Messaufgaben bei FAIR CCC-Systeme an sechs verschiedenen Positionen in der Hochenergie-Strahlführung und den Speicherringen zu installieren.

Der GSI Prototyp des CCC wurde in einem LHe-Badkryostaten eingebaut, der von einem thermischen Schild umgeben ist. Beide Komponenten sind dem Beschleuniger-Vakuum ausgesetzt. Der Heliumbehälter enthält ein elektrisch unterbrochenes Strahlrohr als transversale "warme" Durchtrittsöffnung für den Ionenstrahl. Die supraleitende, konzentrisch zum Rohr angebrachte Sensor-Einheit ist von flüssigem Helium umgeben. Sie besteht aus einem hochpermeablen Ringkern mit einer supraleitenden Sekundärwindung, beides umschlossen von einer ebenfalls supraleitenden magnetischen Abschirmung. Das magnetische Azimutalfeld des Ionenstrahls induziert beim Durchtritt der Teilchen durch den Sensor in der supraleitenden Windung des Ringkerns einen Abschirmstrom. Dieser ist identisch mit dem Wert des Strahlstroms. Er koppelt über einen supraleitenden Anpassungstransformator in den Eingangskreis eines SQUID (Superconducting Quantum Interference Device), welcher in einer weiteren, zylindrischen Abschirmung angebracht ist. Das dem Strahlstrom proportionale Ausgangssignal des SQUID wird in einer externen Auswerteelektronik verstärkt und linearisiert und danach einer Daten-Erfassungs-Einheit (DAQ) zugeführt. Der SQUID wird mit dieser Elektronik im gegengekoppelten Modus betrieben (Flux Locked Loop, FLL).

In der ersten Phase der Arbeiten wurde das von A. Peters, et. al. in den frühen 1990ern entwickelte CCC-System durch umfangreiche Überholungs- und Optimierungsmaßnahmen am Kryo- und Vakuum-System verbessert, und der Erfolg durch entsprechende Labormessungen bestätigt. Anschließend wurden der SQUID und die FLL-Elektronik mit Blick auf die später zu realisierende Kleinserie der FAIR-CCCs durch aktuelle marktgängige Versionen ersetzt. Der so verbesserte Prototyp wurde im Labor weiteren Testmessungen unterzogen, wobei der Ionenstrahl mittels eines gespannten Drahtes und einer Stromquelle nachgebildet wurde. Schließlich wurde die Apparatur zur Durchführung von Strahlmessungen im Experiment-Bereich einer SIS18 Extraktionslinie (HTP) installiert.

Die extreme Empfindlichkeit der supraleitenden Sensor-Komponenten gegenüber einer Vielzahl externer Störeinflüsse erforderte in Folge detaillierte Untersuchungen am System, um die Leistungsfähigkeit, vor allem in der gegebenen elektromagnetischen Störumgebung des Beschleunigers, optimieren zu können. Dazu gehörte der Einsatz eines potenzial-trennenden Signalverstärkers, wie auch die Ermittlung mechanischer Resonanzen der Aufhängung des CCC innerhalb des Kryostaten. Eine präzise Justierung des CCC beim Einbau war erforderlich, um die spätere Schrumpfung der Titan- Spanndrähte bei Abkühlung vorab zu kompensieren.

Für die Intensitätsmessungen am Strahl muss der Arbeitspunkt des SQUID auf einen opti-

malen Punkt der Fluss/Spannnungs-Kurve justiert werden, um im FLL-Betrieb die maximale Empfindlichkeit und Aussteuerbarkeits-Dynamik zu erreichen. Unter diesen Bedingungen wurde die Leistungsfähigkeit des SQUID charakterisiert, wobei $11\,{}^{pA}/\sqrt{Hz}$ als Pegel des auf den Strahlstrom normierten Weißen Rauschens erreicht werden konnten. Dies entspricht einem Rauschwert des magnetischen Flusses von $80\,{}^{\mu\Phi_0}/\sqrt{Hz}$. Über eine vor dem Einbau um den Sensor geschlungene Drahtschleife wurde ein Strom-Kalibrierfaktor von $69.53\,{}^{nA}/\Phi_0$ ermittelt. Dies entspricht im empfindlichsten Messbereich der FLL-Elektronik – mit dem gewählten Gegenkopplungs-Widerstand $R_F = 100\,k\Omega$ – einem Wert von $74.2\,{}^{nA}/V$ am Eingang der DAQ-Einheit. Nach Beendigung von Charakterisierung und Kalibration konnte das CCC-System während der Strahlzeiten ferngesteuert betrieben werden.

Die folgenden Intensitäts-Messungen wurden mit einem Strahl von Ni^{26+} - Ionen bei $600\,{}^{MeV}/u$ im langsamen Extraktionsmodus durchgeführt. Dazu wurden Daten verschiedener Extraktionspulse (‚Spills') für die Dauer von $64\,ms$ bis $5\,s$ aufgezeichnet, wobei Ströme von $2\,nA$ bis zu $105\,nA$ vom CCC registriert wurden. Die Strom-Auflösung des Systems konnte so zu $6 - 120\,{}^{pA}/\sqrt{Hz}$ bestimmt werden, bezogen auf eine Bandbreite von DC bis $10\,kHz$. Unter der vorherrschenden, Störumgebung am Einbauort konnte der CCC einen Strom von $2\,nA_{rms}$ bei einem Signal/Rausch Verhältnis von $6\,dB$ nachweisen. Zu Vergleichszwecken wurde auch das Signal eines in $1\,m$ Abstand strahlabwärts vom CCC eingebauten SEM mit aufgezeichnet. Die simultan aufgenommen Daten der Spill-Struktur wurden verglichen und sowohl im Zeit- als auch Frequenzbereich bewertet. Dabei wurde die Messbandbreite des CCC-Systems durch Aktivierung eines Anti-Alias-Filters in der FLL-Elektronik begrenzt. Beim Vergleich der Intensitätsdaten beider Sensor-Systeme konnte eine hervorragende Linearität von 0.7% in 65 verschiedenen Spills gezeigt werden.

Die unvermeidliche Restwelligkeit einiger Magnetnetzteile im Synchrotron verursacht eine diskontinuierliche Extraktion der Teilchen, sichtbar im Spill durch plötzliche, schnelle Teilchenhäufungen oder Unterbrechungen des Teilchenflusses, wobei die Spitzenintensitäten ein vielfaches des Strom-Mittelwerts betragen können, d. h. ein hoher Crest-Faktor auftritt. Um die Zeitstruktur des Spills zu verbessern, wurde der Strahl unter Beibehaltung des Bunchings im Synchrotron extrahiert, was zu einer zeitabhängigen Impulsverteilung einzelner Teilchen bei Kopplung mit dem Tune Spread führt. Mittels des CCC konnte die Zeitstruktur des extrahierten Strahls aufgelöst und dabei eine Reduzierung des Crest-Faktors und der damit einhergehenden Verringerung der Stromspitzen im Spill unter Variation der HF-Spannung im SIS demonstriert werden. Die Synchrotron-Frequenz und ihre Harmonischen - für dieses Verfahren charakteristische Größen - konnten im Frequenzspektrum der mittels CCC gemessenen Spills identifiziert werden. Ein Vergleich mit Werten, die aus numerischen Berechnungen für die jeweilige Spannung an der Kavität gewonnen wurden, bestätigte die Präzision des CCC.

Im Folgenden wurden mit dem CCC detaillierte Messungen ohne Ionenstrahl - jedoch in der realen Umgebung am Beschleuniger und den damit einhergehenden elektromagnetischen Störfeldern - durchgeführt, um Ursachen und Wirkungen der externen Störgrößen eingehender zu untersuchen. Als zwei wesentliche Effekte dieser Störeinflüsse wurden eine Verformung der Fluss/Spannungs-Kurve des SQUID sowie eine Langzeit-Nullpunktdrift am Ausgang der FLL-Elektronik identifiziert. Die Nullpunktdrift konnte auf thermische Fluktuationen inner-

halb des LHe-Kryostaten zurückgeführt werden. Die Driftrate wurde bei unterschiedlichen LHe-Füllständen bestimmt. Dabei konnte eine Reduzierung der Drift nach Erreichen des thermischen Gleichgewichts beobachtet werden. Es wurden während dreier Abkühlzyklen bei verschiedenen Füllständen Driften zwischen $1.6\,{}^{nA}/_{s}$ und minimal $6.2\,{}^{pA}/_{s}$ gemessen. Als Ursache für die Drift kommen der an den Signaldurchführungen auftretende Seebeck-Effekt sowie in den einzelnen supraleitenden Spulen eingefangener magnetischer Fluss in Betracht.

Zusätzlich zu der beobachteten Langzeit-Drift wurde eine weitere Drift mit deutlicher Abhängigkeit von Druck- und Temperatur-Veränderungen im Kryostaten beobachtet. Ein Anstieg der Temperatur um $36\,mK$ verursachte dabei eine Nullpunktverschiebung entsprechend $1.107\,\mu A$ am Ausgang der CCC-Elektronik. Bei einer genaueren Untersuchung dieses Effekts wurden zeitgleiche hoch aufgelöste Messungen von Druck und Temperatur im Kryostaten mit der Ausgangsspannung des CCC verglichen. Es konnte eine starke Abhängigkeit der beiden Grössen von den Umgebungswerten (LHe-Pegel und dessen thermische Stabilität) nachgewiesen werden. Basierend auf diesen Untersuchungen werden für die neuen CCCs bei FAIR Methoden zur Reduzierung dieser Einflüsse vorgeschlagen – besonders im Hinblick darauf, dass zukünftig eine lokale Rückverflüssigung des abdampfenden LHe vorgesehen ist, was wiederum thermische Instabilitäten zur Folge hat.

Der dynamische Aussteuerungsbereich des CCC-Systems wird durch die maximale Spannung im Gegenkopplungskreis der FLL-Elektronik begrenzt. Für den Maximalwert von $10\,V$ wurde der Dynamik-Bereich zu $\pm 9.37\,\Phi_0$ entsprechend $\pm 93\,\mu A$ im unempfindlichsten Messbereich (bei $R_F = 0.7\,k\Omega$) berechnet. Führt übermäßiges Fluss-Rauschen zum Überschreiten des linearen Bereichs der Fluss/Spannungs-Kurve des SQUID, so reduziert dies den dynamischen Bereich. Aufgrund der auf $57\,kHz$ begrenzten Bandbreite der FLL-Elektronik verursacht die daraus resultierende Begrenzung der Signal-Anstiegsgeschwindigkeit Fluss-Sprünge, wenn der Fluss im Gegenkopplungs-Zweig $\Phi_0/2$ überschreitet. Dies führt zu zeitweisem Verlust des Arbeitspunktes. Typisches Sprünge dieser Art wurden untersucht und Maßnahmen zur Verbesserung des dynamischen Bereichs und der Anstiegsgeschwindigkeit des Systems vorgeschlagen.

Anhand der Ergebnisse der Untersuchungen am CCC-Prototypen und der Erfahrungen aus dem Strahlbetrieb am SIS18 wurden schließlich die fundamentalen Anforderungen an ein verbessertes CCC-System formuliert. Die generellen Randbedingungen sind ein kompaktes Design, die Gewährleistung von UHV-Eigenschaften des Kryostaten, eine hohe Strahlungsresistenz sowie große Strahlrohr-Aperturen. Die derzeit bei GSI laufende Auslegung eines universellen verbesserten CCC-Systems für eine Kleinserie berücksichtigt diese Bedingungen für alle vorgesehenen Einbauorte. Das System soll zukünftig erstmals am CryRing@ESR aufgebaut und in Betrieb genommen werden, wo es zunächst als Prüfstand für Tests wie z.B. dem des automatisierten LHe-Betriebs und der gemeinsamen, für Kontrollsysteme und Datenaufnahme vorgesehenen, Front-End-Software- Architektur (FESA) dienen soll.

Der Durchmesser des Strahlrohrs am CCC wurde von 100 mm im alten GSI-Prototypen auf $150\,mm$ für die FAIR-Vakuumstrecken erweitert. Zusammen mit dem separierten Isoliervakuum bedingt dies einen deutlichen Zuwachs beim Durchmesser der supraleitenden Abschirmung. Zur Optimierung der Abschirmung bezüglich ihrer magnetischen Eigenschaften und zur Realisierung eines Kryostaten mit möglichst kompakten Abmessungen wurden mit dem FEM-Simulations-

Paket “Comsol Multiphysics^{TM}” eingehende Untersuchungen der geometrischen Parameter vorgenommen. Dabei wurden Berechnungen zur Abhängigkeit des Dämpfungsfaktors von der Anzahl der Mäandern am Eintrittspalt, sowie von der Spaltweite und den Radiusverhältnissen der Schirmung ausgeführt. Es konnte quantitativ gezeigt werden, dass ein vergrößerter Innenradius des Schirms eine Verringerung der Dämpfung der kritischen transversalen Komponente externer magnetischer Störfelder bewirkt. Dies zeigt die Notwendigkeit, bei den neuen CCC-Systemen den durch die Vergrößerung verringerten Abschirmfaktor durch eine erhöhte Zahl von Mäandern am Schirm zu kompensieren. Aus den für die unterschiedlichen Anzahlen von Mäandern berechneten Abschirmfaktoren kann für den zukünftigen CCC ein Kompromiss aus Schirmwirkung und Nb-Materialaufwand (bzw. Einbaulänge) ermittelt werden.

Appendix 1

Field attenuation Through a Coaxial Cylinder- Analytical Approach

In the magneto-static case without any current flowing through the surface of the superconductor, the field attenuation through a simple case of a coaxial cylinder can be derived by the magnetic scalar potential V. The Laplace equation of the scalar potential in cylindrical co-ordinates can be written as,

$$\frac{1}{r}\frac{\partial}{\partial r}\left(r\frac{\partial V}{\partial r}\right)+\frac{1}{r^2}\frac{\partial V^2}{\partial \phi^2}+\frac{\partial^2 V}{\partial z^2}=0 \tag{7.1}$$

The scalar potential can be solved by re-writing it in the form, $V(\rho,\phi,z)=R(\rho)\Phi(\phi)Z(z)$ and finding the solution for each component. Substituting this in equation 7.1 and dividing throughout by $R\Phi Z\cdot\rho^{-2}$, we have

$$\frac{\rho}{R}\frac{d}{d\rho}\left(\rho\frac{dR}{d\rho}\right)+\frac{1}{\Phi}\left(\frac{d^2\Phi}{d\phi^2}\right)+\frac{\rho^2}{Z}\frac{d^2Z}{dz^2}=0 \tag{7.2}$$

Multiplying with R throughout Setting

$$\frac{1}{\Phi}\left(\frac{d^2\Phi}{d\phi^2}\right)=-n^2 \tag{7.3}$$

and

$$\frac{1}{Z}\frac{d^2Z}{dz^2}=k^2 \tag{7.4}$$

We get,

$$\rho\frac{d}{d\rho}\left(\rho\frac{dR}{d\rho}\right)+\left(k^2\rho^2-n^2\right)R=o$$

By setting $k\rho=\nu$, we get the Bessel's equation,

$$\frac{d^2R}{d\nu^2}+\frac{1}{\nu}\frac{dR}{d\nu}+\left(1-\frac{n^2}{\nu^2}\right)R=0 \tag{7.5}$$

solving for each components $R,\Phi\,and\,Z$, the second order differential equations, 7.3, 7.4 and 7.5 gives the general solution,

$$\Phi(\phi)=\begin{cases} A\phi+B & n=0 \\ A_n\sin\left(n\phi+D\right) & n>0 \end{cases} \tag{7.6}$$

$$Z(z) = \begin{cases} Cz + D & k = 0 \\ C_k \sin(kz) + D_k \cos(kz) & k > 0 \end{cases} \tag{7.7}$$

$$R(\rho) = \begin{cases} E \ln \rho + F & n = 0, k = 0 \\ E_n^0 \rho^n + F_n^0 \rho^{-n} & n > 0, k = 0 \\ E_n^k I_n(k\rho) + F_n^k K_n(k\rho) & n \geqslant 0, k > 0 \end{cases} \tag{7.8}$$

where I_n and K_n are the modified Bessel functions of the first and second kind respectively of integer order. The coefficients $A...F$ can be calculated by applying different boundary conditions given by the nature of the superconducting geometry. The complete solution can be developed into a Fourier series,

$$V(\rho, \phi, z) = \sum_{n=0}^{\infty} \sum_{all\ k} V_{nk}(k\rho) \sin(n\phi + \nu_n) \exp(-kz) \tag{7.9}$$

The lowest attenuation is produced by a transverse external field and can be expanded in the case of a simple cylinder into the following series,

$$V = V_{11} \exp\left(\frac{-1.84z}{r_o}\right) + V_{12} \exp\left(\frac{-5.33z}{r_o}\right) + ...$$

and for a coaxial cylinder within the limit $\frac{r_o}{r_i} \leq 1.5$,

$$V = V_{11} \exp\left(\frac{-1.05z}{r_o}\right) + V_{12} \exp\left(\frac{-34.55z}{r_o}\right) + ...$$

In general the attenuation by a coaxial cylinders depends largely on the ratio of radii. However in the case of superconducting magnetic shield, $\frac{r_o}{r_i}$ is close to one and the series can be approximated to equations 6.4 and 6.5.

Bibliography

[1] Sigurd Hofmann. Welcome copernicium? *Nature Chemistry*, 2(2):146, February 2010. 1.1

[2] J. Khuyagbaatar, A. Yakushev, Düllmann, et al. ^{48}Ca $+^{249}$ Bk fusion reaction leading to element $z = 117$: Long-lived α-decaying ^{270}Db and discovery of ^{266}Lr. *Phys. Rev. Lett.*, 112:172501, May 2014. 1.1

[3] G. Kraft. Tumor therapy with heavy charged particles. *Progress in Particle and Nuclear Physics*, 45, Supplement 2(0):S473 – S544, 2000. 1.1

[4] https://www.gsi.de. 1.1

[5] http://www.fair-center.de. 1.1

[6] Thomas Stoehlker, Yuri A Litvinov, Vincent Bagnoud, et al. Sparc experiments at the high-energy storage ring. *Phys. Scr.*, 2013(T156):014085, 2013. 1

[7] H. H. Gutbrod, K. D. Groß, W. F. Henning, D. Krämer, G. Walter, I. Augustin, H. Eickhoff, et al. *FAIR Baseline Technical Report*. GSI, Darmstadt, Germany, September 2006. 1.1

[8] Technical design report super fragment separator. Technical report, GSI, Darmstadt, 2008. 1.1

[9] G.Kube. *Specific Diagnostic needs for different machines*. Number CERN-2009-005. CERN, Dourdan, France, 2008. 1.2

[10] Peter Forck. *Lecture Notes on Beam Instrumentation and Diagnostics*. GSI, Darmstadt, Germany, 2011. 1.2, 1.3, 2

[11] P. Odier. DCCT technology review. In *Proceedings of Workshop on DC Current Transformers and Beam-Lifetime Evaluations*, number CARE-Note-2004-023-HHH, pages 3–5, 2004. 1.2.1

[12] Robert C. Webber, editor. *Tutorial on Beam Current Monitoring*, FERMILAB-Conf-00-119, 2000. 1.2.1

[13] Charles Kittel. Physical theory of ferromagnetic domains. *Rev. Mod. Phys.*, 21:541–583, Oct 1949. 1.2.1

[14] M. Schwickert, H. Braeuning, F. Kurian, H. Reeg, et al. Beam current monitors for FAIR. In *Proceedings of IPAC, Dresden, Germany*, 2014. 1.2.1

[15] P. Strehl. *Beam Instrumentation and Diagnostics.* Springer- Verlag Berlin, Heidelberg, 2006. 1.2.2, 1.2.2

[16] Andreas Peters, Wolfgang Vodel, Helmar Koch, Ralf Neubert, Hansjoerg Reeg, and Claus Hermann Schroeder. A cryogenic current comparator for the absolute measurement of na beams. *AIP Conference Proceedings-Beam Instrumentation Workshop*, 451(1):163–180, 1998. 1.2.2, 3, 3.5.1, 5.1.3

[17] Rene Geithner. *Optimierung eines kryogenen Stromkomparators für den Einsatz als Strahlmonitor.* PhD thesis, Physikalisch-Astronomischen Fakultät, Friedrich-Schiller-Universität Jena, 2013. 1.3, 3.4

[18] Paolo Tripodi, Di Gioacchino Daniele, and Vinko Jenny Darja. A review of high temperature superconducting property of PdH system. *International Journal of Modern Physics B*, 21(18n19):3343–3347, 2007. 2.1

[19] W. A. Little. Possibility of synthesizing an organic superconductor. *Phys. Rev.*, 134:A1416–A1424, Jun 1964. 2.1

[20] Paolo Tripodi, Daniele Di Gioacchino, Rodolfo Borelli, and Jenny Darja Vinko. Possibility of high temperature superconducting phases in pdH. *Physica C: Superconductivity*, 388-389:571 – 572, 2003. Proceedings of the 23rd International Conference on Low Temperature Physics (LT23). 2.1

[21] D. Dew-Hughes. The critical current of superconductors: An historical review. *Low Temperature Physics*, 27(9):713–722, 2001. 2.1

[22] Charles Poole, Horacio Farach, Richard Creswick, and Ruslan Prozolov. *Superconductivity, Third edission.* Elsevier, 2014. 2.1, 2.3

[23] Leon N. Cooper. Bound electron pairs in a degenerate fermi gas. *Phys. Rev.*, 104:1189–1190, Nov 1956. 2.1

[24] Bascom S. Deaver and William M. Fairbank. Experimental evidence for quantized flux in superconducting cylinders. *Phys. Rev. Lett.*, 7:43–46, Jul 1961. 2.2

[25] R. Doll and M. Näbauer. Experimental proof of magnetic flux quantization in a superconducting ring. *Phys. Rev. Lett.*, 7:51–52, Jul 1961. 2.2

[26] J. P. Carbotte. Properties of boson-exchange superconductors. *Rev. Mod. Phys.*, 62:1027–1157, Oct 1990. 2.2

[27] J. M. Rowell. Magnetic field dependence of the josephson tunnel current. *Phys. Rev. Lett.*, 11:200–202, Sep 1963. 2.2

[28] RL Fagaly. Superconducting quantum interference device instruments and applications. *Rev. Sci. Instrum.*, 77(10):101101, 2006. 2.3

[29] Alex Braginski and Yi Zhang. *The SQUID Handbook: Fundamentals and Technology of SQUIDs and SQUID Systems, Volume I: Practical RF SQUIDs- Configuration and Performance*, chapter 6, pages 219–250. Wiley-VCH Verlag GmbH & Co. KGaA, 2005. 2.3

[30] Boris Chesca, Reinhold Kleiner, and Dieter Koelle. *The SQUID Handbook: Fundamentals and Technology of SQUIDs and SQUID Systems, Volume I: SQUID Theory*, chapter 2, pages 29–92. Wiley-VCH Verlag GmbH & Co. KGaA, 2005. 2.3.1, 2.3.1, 2.3.1, 2.3.3, 5.1.2

[31] Victor Jan de Waal. *Low Noise SQUIDs*. PhD thesis, TU Delft, 1983. 2.3.1

[32] Robin Cantor and Dieter Koelle. *The SQUID Handbook: Fundamentals and Technology of SQUIDs and SQUID Systems, Volume I: Practical DC SQUIDs: Configuration and Performance*, chapter 5, pages 171–217. Wiley-VCH Verlag GmbH & Co. KGaA, 2005. 2.3.1, 2.11

[33] D. Koelle, R. Kleiner, F. Ludwig, E. Dantsker, and John Clarke. High-transition-temperature superconducting quantum interference devices. *Rev. Mod. Phys.*, 71:631–686, Apr 1999. 2.3.1

[34] Martin Podt. *Wideband Low-Noise Integrated SQUID Systems*. PhD thesis, University of Twente, 2003. 2.3.3

[35] O. Dossel, B. David, M. Fuchs, W.H. Kullmann, and K.M. Luedeke. A modular low noise 7-channel SQUID-magnetometer. 27(2):2797–2800, Mar 1991. 2.3.3, 2.4.2

[36] Bonaventura Savo, Frederick C. Wellstood, and John Clarke. Low frequency excess noise in NbAl2O3Nb josephson tunnel junctions. *Appl. Phys. Lett.*, 50(24):1757–1759, 1987. 2.3.3

[37] Dietmar Drung. High-Tc and low-Tc dc SQUID electronics. *Supercond. Sci. Technol.*, 16(12):1320, 2003. 2, 2.4, 2.4

[38] M. Kiviranta and H. Seppa. DC-SQUID electronics based on the noise cancellation scheme. *Applied Superconductivity, IEEE Transactions on*, 5(2):2146–2148, June 1995. 2.4.2

[39] Dietmar Drung. Low frequency noise in low Tc multiloop magnetometers with additional positive feedback. *Appl. Phys. Lett.*, 67(10):1474–1476, 1995. 2.4.2

[40] Y. Zhang, N. Wolters, R. Otto, and H. J Krause. Non-constant bias current for dc SQUID operation. *Physica C: Superconductivity*, 368(1-4):181 – 184, 2002. 2.4.2

[41] J. E. Zimmerman. Sensitivity enhancement of superconducting quantum interference devices through the use of fractional-turn loops. *J. Appl. Phys.*, 42(11):4483–4487, 1971. 2.5

[42] Coupling magnetic signals to a SQUID amplifier. SQUID Application Note 1052-202A, Quantum Design, 2001. 2.5

[43] Jukka Knuutila, Matti Kajola, Heikki Seppae, Risto Mutikainen, and Jorma Salmi. Design, optimization, and construction of a dc SQUID with complete flux transformer circuits. *J. Low Temp. Phys.*, 71(5-6):369–392, 1988. 2.5

[44] I. K. Harvey. A precise low temperature dc ratio transformer. *Rev. Sci. Instrum.*, 43(11):1626–1629, 1972. 3

[45] K. Grohmann, D. Hechtfischer, J. Jakschik, J. Jakschik, and H. Luebbig. A cryo device for induction monitoring of dc electron or ion beams with nano-ampere resolution. *Superconducting quantum interference devices and their applications, Walter de Gruyter & Co.*, pages 311–315, 1977. 3, 6.3.3

[46] W. Vodel and K. Makiniemi. An ultra low noise dc SQUID system for biomagnetic research. *Meas. Sci. Technol.*, 3(12):1155, 1992. 3

[47] H. Koch, H. Muehlig, R. Neubert, A. Peters, H. Reeg, C.H. Schroeder, and W. Vodel. Review of the experimental results with a cryogenic current comparator. In *Proceedings of EPAC*, 1996. 3, 5.1.3

[48] A. Peters, H. Reeg, P. Forck, W. Vodel, and R. Neubert. Recent improvements of a cryogenic current comparator for nA ion beams with high intensity dynamics. In *Proceedings DIPAC, Chester, UK*, 1999. 3, 5.1.3

[49] Graham Walker. *Cryocoolers.* The International Cryogenics Monograph Series, Springer Science + Business Media, LLC, 1983. 3.2.2

[50] Ph. Lebrun, editor. *An Introduction to Cryogenics*, volume CERN/AT 2007-1, 2007. 3.2.2

[51] J.P. Le E.D. Marquardt and Ray Radebaugh. Cryogenic material properties database. In *11th International Cryocooler Conference*, 2000. 3.2.3

[52] A new cryogenic diode thermometer. Technical report, Lake Shore Cryotronics, Inc., 2001. 3.2.4

[53] K. Grohmann, H.D. Hahlbohm, D. Hechtfischer, and H. Lübbig. Field attenuation as the underlying principle of cryo-current comparators 2. ring cavity elements. *Cryogenics*, 16(10):601 – 605, 1976. 3.3.1, 6.3.1, 6.3.3

[54] Febin Kurian. Development of a superconducting magnetic shielding. Master's thesis, Goethe Universität, Frankfurt am Main, 2011. 3.3.1

[55] Hans. L. Pecseli. *Fluctuations in Physical Systems.* Cambridge University Press, 2000. 3.3.2

[56] K. Knaack, K. Wittenburg, R. Neubert, S. Nietzsche, F. Schiller, W. Vodel, and A. Peters. Current status of the SQUID based cryogenic current comparator for absolute measurements of the dark current of superconducting rf accelerator cavities. In *Proceedings of DIPAC*, 2007. 3.3.2

[57] Soft magnetic materials and semi-finished products. Technical Report PHT-001, Vacuumschmelze GmbH & Co. KG, P.O.Box. 22 53 63412 Hanau, Germany, Edition 2002. 3.3.2

[58] A. Steppke, R. Geithner, S. Hechler, R. Nawrodt, R. Neubert, W. Vodel, M. Schwickert, H. Reeg, and P. Seidel. Application of lts-SQUIDs in nuclear measurement techniques. *Applied Superconductivity, IEEE Transactions on*, 19(3):768–771, June 2009. 3.3.2

[59] Rene Geithner, Daniel Heinert, Ralf Neubert, Wolfgang Vodel, and Paul Seidel. Low temperature permeability and current noise of ferromagnetic pickup coils. *Cryogenics*, 54(0):16 – 19, 2013. 3.3.2

[60] Wolfgang Vodel. The SQUID based cryogenic current comparator -a useful tool for beam diagnostics. In *Workshop on "Low Current, Low Energy Beam Diagnostics", Hirschberg-Grosssachsen*, 2009. 3.5

[61] Magnicon physical research and instrumentation, Lemsahler Landstr. 171 22397 Hamburg Germany. *High Performance dc SQUID Electronics XXF-1 Manual*, v3.3.8 edition, 2011. 3.4

[62] N. Uchida, K. Enpuku, Y. Matsugaki, S. Tomita, F. Irie, and K. Yoshida. Flux trapping in josephson tunnel junctions. *J. Appl. Phys.*, 54(9):5287–5292, 1983. 3.4.1

[63] Koichi Yokosawa, Daisuke Suzuki, Keiji Tsukada, Seiichi Ugai, Toshiaki Suzuki, and Yasushi Shimizu. Low- tc SQUIDs with a built-in heater module to remove flux trapping. *Supercond. Sci. Technol.*, 13(8):1286, 2000. 3.4.1

[64] Vibration diagnostics for industrial electric motor drives. Technical report, Bruel & Kjær, Nærum, Denmark, 2007. 3.5.2

[65] Dietmar Drung and Michael Mueck. *The SQUID Handbook: Fundamentals and Technology of SQUIDs and SQUID Systems, Volume I: SQUID Electronics*, chapter 4, pages 127–170. Wiley-VCH Verlag GmbH & Co. KGaA, 2005. 4.1.2

[66] P.Forck and T. Hoffmann. Test of different beam loss detectors at the GSI heavy ion synchrotron. In *Proceedings of DIPAC, ESRF, Grenoble, France*, 2001. 4.2

[67] C. Andre, F. Becker, H. Braeuning, P. Forck, R. Haseitl, R. Lonsing, and B. Walasek-Hoehne. Beam-induced fluorescence (BIF) monitors as a standard operating tool. In *Proceedings of DIPAC- Hamburg, Germany*, 2011. 4.2

[68] E. J. Sternglass. Theory of secondary electron emission by high-speed ions. *Phys. Rev.*, 108:1–12, Oct 1957. 4.2

[69] James F. Ziegler, M.D. Ziegler, and J.P. Biersack. SRIM - the stopping and range of ions in matter (2010). *Nuclear Instruments and Methods in Physics Research Section B: Beam Interactions with Materials and Atoms*, 268(11-12):1818 – 1823, 2010. 19th International Conference on Ion Beam Analysis. 1

[70] T. Hoffmann, P. Forck, and D. A. Liakin. New spill structure analysis tools for the VME based data acquisition system ABLASS at GSI. *AIP Conference Proceedings*, 868(1):343–350, 2006. 2

[71] R. Singh. *Tune Measurement at GSI SIS-18: Methods and Applications.* PhD thesis, Technische Universität, Darmstadt, 2014. 4.3.1, 4.11

[72] H. Klingbeil P. Huelsmann, O. Boine-Frankenheim and G. Schreiber. Considerations concerning the rf system of the accelerator chain SIS12/18 - SIS100 for the FAIR-project at GSI. GSI-Acc-Note-2004-08-001, GSI, Darmstadt, Germany, August 2004. 4

[73] K. Poljanc M. Regler, M. Benedikt. Medical accelerators for hadrontherapy with protons and carbon ions. In *CERN Accelerator School, Intermediate Accelerator Physics, Seville, Spain, October 15-26*, 2001. 4.3.1

[74] Klaus Wille. *The Physics of Particle Accelerators: An Introduction.* Oxford University Press, 2000. 4.3.1

[75] L. Badano, M. Benedikt, P. Bryant, M. Crescenti, P. Holy, P. Knaus, A. Maier, M. Pullia, and S. Rossi. Synchrotrons for hadron therapy: Part i. *Nuclear Instruments and Methods in Physics Research Section A: Accelerators, Spectrometers, Detectors and Associated Equipment*, 430:512 – 522, 1999. 4.3.1, 4.3.5

[76] Tetyana Galatyuk and Manuel Lorenz. Investigating the microscopic properties of strongly interacting matter with HADES. *Central European Journal of Physics*, 10(6):1295–1301, 2012. 4.3.3

[77] D. Ondreka M. Kirk and P. Spiller. Sis-18 rf knock-out optimisation studies. In *Conference Proceedings, International Particle Accelerator Conference (IPAC), Shanghai*, 2013. 4.3.5

[78] A. Peters P. Forck, H. Eickhoff and A. Dolinskii. Measurements and improvements of the time structure of a slowly extracted beam from a synchrotron. In *Proceedings of European Particle Accelerator Conference, Vienna, Austria*, pages 2237–2239, 2000. 4.3.5, 4.3.5

[79] G. Testa, C. Granata, C. Di Russo, S. Pagano, M. Russo, and E. Sarnelli. Low-noise magnetometers with asymmetric superconducting quantum interference devices. *Appl. Phys. Lett.*, 79(24):3989–3991, 2001. 5.1.2

[80] D Drung. Simplified analysis of direct SQUID readout schemes. *Supercond. Sci. Technol.*, 23(6):065006, 2010. 5.1.2

[81] Hiroto Adachi, Ken ichi Uchida, Eiji Saitoh, and Sadamichi Maekawa. Theory of the spin seebeck effect. *Reports on Progress in Physics*, 76(3):036501, 2013. 5.1.2

[82] Dietmar Drung. Improved dc SQUID read-out electronics with low 1/f noise preamplifier. *Rev. Sci. Instrum.*, 68(11):4066–4074, 1997. 5.1.3

[83] www.ngdc.noaa.gov. 5.1.3

[84] S. Schöne, M. Mück, G. Thummes, and C. Heiden. Investigation of the response of superconducting quantum interference devices to temperature variation. *Rev. Sci. Instrum.*, 68(1):85–88, 1997. 5.1.3, 5.2.4, 5.2.4, 5.2.4, 5.3

[85] Temperature dependent response of a dc-SQUID. Technical report, Defence Research Establishment Atlantic, 1997. 5.2.3

[86] J. A. Mydosh and Hans Meissner. Dependence of the critical currents in superconducting films on applied magnetic field and temperature. *Phys. Rev.*, 140:A1568–A1580, Nov 1965. 5.2.4

[87] R. A. Kamper and J. E. Zimmerman. Noise thermometry with the josephson effect. *J. Appl. Phys.*, 42(1):132–136, 1971. 5.2.4

[88] C P Lusher, Junyun Li, V A Maidanov, M E Digby, H Dyball, A Casey, J Nyeki, V V Dmitriev, B P Cowan, and J Saunders. Current sensing noise thermometry using a low TC dc SQUID preamplifier. *Meas. Sci. Technol.*, 12(1):1, 2001. 5.2.4

[89] R. Egli and F. Heller. High-resolution imaging using a high-tc superconducting quantum intereference device (SQUID) magnetometer. *J. Geophys. Res.*, 105(B11):25709–25727, 2000. 5.2.4

[90] John M. Martinis. Course 13 superconducting qubits and the physics of josephson junctions. In Jean-Michel Raimond Daniel EstÃšve and Jean Dalibard, editors, *École d' été de Physique des Houches Session LXXIX*, volume 79 of *Les Houches*, chapter Quantum Entanglement and Information Processing, pages 487 – 520. Elsevier, 2004. 5.2.4

[91] D. Drung. High-performance dc SQUID read-out electronics. *Physica C Superconductivity*, 368:134–140, March 2002. 5.4.1

[92] Volkmar Schultze, Dietmar Drung, Rob IJsselsteijn, and Hans-Georg Meyer. A high- tc SQUID gradiometer with integrated homogeneous field compensation. *Supercond. Sci. Technol.*, 17(5):S165, 2004. 5.4.1

[93] T. Hoffmann. FESA- the front end software architecture at FAIR. In *Proceedings of PCaPAC08, Ljubljana, Slovenia*, 2008. 6.1

[94] S. Ratschow, F. Hagenbuck, and P. J. Spiller. The high energy beam transport system for FAIR. In *Proceedings of EPAC08, Genoa, Italy*, 2008. 6.1.1

[95] Germany GSI Darmstadt. Conceptual design report, 11 2001. 6.1.2

[96] CRYRING@ESR: A study group report. Technical report, GSI, Darmstadt, 2012. 6.1.2

[97] FAIR green paper - the modularized start version. Technical report, GSI, Darmstadt, 2009. 6.1.2

[98] T. Stöhlker R. Neubert J. Tan C.P. Welsch M. Fernandes, R.Geithner and M. Schwickert. A cryogenic current comparator for the low-energy antiproton facilities at cern. In *Proceedings of IBIC*, 2015. 6.2.1, 6.2

[99] C. P. Welsch M.Fernandez, J. Tan. A cryogenic current comparator for the low energy antiproton facitities at CERN. In *Proceedings of IBIC, Monterey, California, USA*, 2014. 6.2.3

[100] Anton Belousov. *Radiation Effects on Semiconductor Devices in High Energy Heavy Ion Accelerators*. PhD thesis, Technischen Universität, Darmstadt, Germany, 2014. 6.2.4

[101] Emerging radiation hardness assurance (rha) issues: A NASA approach for space flight programs, Kenneth A. LaBel and Allan H. Johnston and Janet L. Barth and others. 6.2.4

[102] S. Loechner. *Development, Optimisation and Characterisation of a Radiation Hard Mixed-Signal Readout Chip for LHCb*. PhD thesis, University of Heidelberg, 2006. 6.2.4

[103] Private communication. Technical report, GSI, Darmstadt, 2015. 6.2.4

[104] K. Grohmann, H.D. Hahlbohm, D. Hechtfischer, and H. Lübbig. Field attenuation as the underlying principle of cryo current comparators. *Cryogenics*, 16(7):423 – 429, 1976. 6.3.1, 6.3.1

[105] K. Grohmann and D. Hechtfischer. Magnetic shielding by superconducting simple and coaxial cylinders: a comparison. *Cryogenics*, 17(10):579 – 581, 1977. 6.3.1, 6.3.2

Acknowledgments

At the end, though only my name appears on the cover of this PhD thesis, a number of people contributed both directly and indirectly to shape this work in its present form. My abiding gratitude to all those people who were a part of my four years in the CCC project at GSI.

First I thank my supervisor Dr. Peter Hülsmann for all his support and care throughout this period. My mentors Dr. Marcus Schwickert and Dr. Thomas Sieber, are the two biggest reasons for the success of this project. Throughout the busy daily schedule, Dr. Schwickert always made sure I receive all possible academic and personal support from his side. I appreciate all his contributions by time, efforts, patience, ideas, funding and motivations during the PhD period. I extend my deepest gratitude to Dr. Sieber, for the support and long discussions on nearly every aspects of this works and huge efforts on corrections on the thesis. His supervision was the most crucial factor in shaping the thesis into its current form. I thank Dr. Thomas Stöhlker for the supports to the CCC project as well as me personally with funding, guidance and appreciations throughout the PhD work.

A special mention to Dr. Piotr Kowina, whom I consider working with, was unique experience and most informative. I received the biggest hands-on contributions to this PhD work from him. I thank him for helping me at nearly every stage of my work and most importantly for the "very special pressure sensor" used in my experiments. I also thank Hansjörg Reeg, for the support both academically and personally every single time it mattered. As a person who was involved from the first day in the CCC project, his contributions and knowledge were pivotal in every stage of development of this project.

Being the collaborating partners, I benefited a lot from the colleagues in FSU, Jena, Dr. Wolfgang Vodel, Dr. Rene Geithner, and Ralf Neubert. I thank them for those very long days/nights of experiments at GSI and ever informative meetings. I extend my appreciation to the crew of the SIS accelerator for the excellent technical support during the beam measurements. As the topic spread across a wide technical development, often I had to seek support from my colleagues at GSI. In the beam diagnostics group and cryogenic group, every single one has greeted me with smiling face and helping hands and gave immense support. Peter, Rahul, Christoph, Rainer, Rolf are only few names I couldn't leave out of many for with their support either by scientific, technical or personal matters. I thank Amaresh and Ronald for their company and numerous discussions about almost everything in this planet.

I thank DITANET (FP7 Marie Curie Initial Training Network) for selecting me into the program which lead to this PhD work. It was through DITANET I could attend so many conferences and training programs which eventually made me feel like a member of the accelerator

community. I extend my sincere thanks to Frankfurt Institute of Advanced Studies and Helmholtz Institute, Jena for supporting me with funding to finish this work. The HGS-HiRe program provided soft-skill schools and workshops which made sure my continuous involvement in the scientific community.

I owe thanks to Dr. Thomas Kalarikad who gave me inspiration to look at this world-and more importantly look at myself-differently. His guidance and philosophies will be remembered as extremely influential in career as well as personal life. Nothing can be replaced for my friends, throughout all these years who lead me the way and always cared for me. I thank all of them for all the support and well wishes and for still being good friend of the little bit-strange one.

I extend my gratitude to my wonderful family for the support and care for all these years. My father - my first teacher, in both life and in school - taught me to enjoy the beauty of hard work through his actions; my mother, for all those countless prayers and those gentle pushes I needed for all these years. My elder brother was both my first friend and look-up to man. My younger brother, for being there to understand, share my philosophies.

Knowing all these words of thanks still remain understatements when I look into the magnitude of help and support I received, I dedicate this thesis work to my wife Priyanka. Contributing to nearly everything these years, all those tears, all those happy moments gave me significant motivations every time I lacked. She literally lived for and with me all those very very tough times.

Febin Kurian
GSI, Darmstadt
October 2015